Navigation using Radio-Frequency Observables from LEO Constellations with Possible Aiding from an Inertial Navigation System

Brian K. McLemore

Dissertation submitted to the Faculty of the
Virginia Polytechnic Institute and State University
in partial fulfillment of the requirements for the degree of

Doctor of Philosophy
in
Aerospace Engineering

Mark L. Psiaki, Chair
Mathieu Joerger
Craig A. Woolsey
Wayne A. Scales

December 16^{th}, 2022
Blacksburg, Virginia

Keywords: Large LEO constellations, Doppler shift navigation, Kalman filter, INS

Navigation using Radio-Frequency Observables from LEO Constellations with Possible Aiding from an Inertial Navigation System

Brian K. McLemore

(ABSTRACT)

Analyses are performed on the potential of using radio-frequency signals from massive LEO satellite constellations. This work aids in the creation of a navigation system independent of current GNSS. A tightly-coupled carrier Doppler shift/INS filter is developed to determine the feasibility of using signals of opportunity from LEO satellites for navigation purposes. This portion of the work makes two major contributions to the field of satellite-based radio-navigation systems. The first contribution is an analysis that shows GNSS-like position accuracy is possible using only INS measurements and carrier Doppler shift from LEO communication constellations. The second contribution is that INS quality, signal availability, and constellation design can significantly impact the navigation accuracy of a carrier Doppler shift/INS Kalman filter. An analysis of the costs and benefits of using model replacement over a Markov model in the dynamic propagation step of a tightly-coupled carrier Doppler shift/INS Kalman filter is performed in the next part of this work. This portion of the work makes contributions to the field of satellite-based radio-navigation systems. The main contribution is an analysis that shows Gauss-Markov models can be used instead of model replacement without increasing navigation error. Next, a DOP analysis is developed for systems using pseudorange and carrier Doppler shift measurements in point-solution batch filters that do not rely on INS data or dynamic propagation. This section's contributions to the field of satellite-based radio-navigation systems include a combined pseudorange and carrier Doppler shift DOP analysis using a novel DOP metric and an example of how to use

the DOP analysis to identify the constellation characteristics, such as alternating ascending and descending nodes, that the OneWeb constellation could change to increase navigation accuracy.

Navigation using Radio-Frequency Observables from LEO Constellations with Possible Aiding from an Inertial Navigation System

Brian K. McLemore

(GENERAL AUDIENCE ABSTRACT)

This dissertation presents research on using large communication satellite constellations as an independent backup to GPS. Simulated data are used to study the feasibility and navigation accuracy of such a system. Also investigated are different implementations of the algorithms used to navigate. Finally, a general analysis is developed to quickly approximate the navigation accuracy of a system that uses multiple measurement types.

Acknowledgments

I would first like to thank my advisor, Dr. Mark L. Psiaki for all of the knowledge and guidance that he imparted to me during my time spent at Virginia Tech. This work would not be possible without him. I would also like to thank the members of my committee, including Dr. Mathieu Joerger, Dr. Craig Woolsey, and Dr. Wayne Scales. Their comments, critiques, and advice were invaluable in the creation of this work. I would also like to thank the members of my research group including Michael Esswein and Brian Slosman, among others, for the weekly discussions and commiserations that helped me make it through the difficult times during graduate school.

This work would not have been possible without the DOD NDSEG Fellowship sponsored by the AFOSR that funded the first three years of my graduate school. I would also like to extend my sincere thanks to Dr. Matt Zeiger and the NAL Research Corporation for funding my GRA for my fourth year of graduate school. They not only provided my funding for a year but also provided an interesting real-world problem to work on for my GRA.

Lastly, I would like to thank my parents, friends, and family for supporting me throughout my time at Virginia Tech. Their encouragement helped keep my spirits high. Without their support, this work would not have been possible.

Contents

List of Figures

List of Tables

Chapter 1

Introduction

1.1 Preface

This dissertation is in the manuscript format. As such, it consists of three separate manuscripts. Each of the three manuscripts has two authors. The first and main author is myself. The second author is my advisor, Dr. Mark L. Psiaki. His contributions to each work include help with idea formulation, technical derivation, editing, and providing initial coding scripts to accelerate the work process. The vast majority of technical work and writing has been completed by the first author of each paper.

1.2 Navigation using RF Signals from LEO Constellations

Every day millions of people use Global Navigation Satellite Systems (GNSS) such as the U.S. Global Positioning System (GPS), the European Galileo System, the Russian GLONASS System, and the Chinese BeiDou system. Localization services provided by GNSS are indispensable for civilians and militaries around the world. Driving to the store, planting crops, and guiding missiles all rely on GNSS. A disruption in GNSS could cause substantial hardships. As the dependence on GNSS increases, the number of people and methods attempting

to disrupt GNSS increases. Recently, jamming and spoofing disruptions have become more common. Jamming denies the use of GNSS signals by increasing the noise in a given area to the point of drowning out the signals. This method disrupts GNSS, but is straightforward to detect. Spoofing, however, is a more complicated disruption that is harder to detect than jamming. Spoofing occurs when a GNSS receiver is tricked by a set of false signals. The receiver processes them as though they were the true signals and determines an incorrect position, an incorrect time, or both. An incorrect position fix caused by spoofing can be much more dangerous than an inability to determine position due to jamming.

Instances of jamming and spoofing have been reported in [11], [3], [28], and [43]. In [11], the GNSS signals at Newark airport were jammed periodically, shutting down airport services. Eventually, the jamming signal was traced back to a commercial truck driver on a nearby highway. Iran claimed to spoof an American drone, resulting in its capture in [3]. In [28], several ships in the Black Sea were spoofed. Researchers spoofed a luxury yacht's navigation system in [43]. A spoofer could easily cause a boat or autonomous drone to crash by tricking its navigation system, as shown in [43]. Jamming in Newark and spoofing in Iran and the Black Sea are just a few examples of targeted interruptions in GNSS services.

Vulnerabilities such as jamming and spoofing have motivated research into detection and prevention methods. In addition to preventative measures to protect against jamming and spoofing, there have been calls to create a navigation system independent of current GNSS [41]. An independent system could serve as a backup or alternative to GNSS when there are interruptions in GNSS services. The main goal of this work is to investigate the potential of new massive Low Earth Orbit (LEO) constellations to provide radio-navigation observables for a navigation system that can function independently of existing GNSS.

If LEO communication constellation satellites carry GNSS-quality atomic clocks and omnidirectional beacons, and if they broadcast precise ephemeris information and Pseudo-Random

Number (PRN) codes, then their large number of satellites would make navigation accuracy better than GNSS. It is, however, unlikely that all of these conditions will be met by such constellations. Atomic clocks are expensive and require more mass and power than crystal oscillators. They are not needed to support such constellations' primary function of providing global communications. Omnidirectional antenna patterns are also not useful for modern communication because they waste power and bandwidth. The transmission of PRN codes would come at the cost of a reduction of communication data throughput.

Carrier Doppler shift measurements might be useable as navigation observables in a way that obviates the need for such constellation features. In [42], it is shown that eight simultaneous Doppler shift measurements is the minimum required number to perform a point solution that is analogous to the four-satellite pseudorange point solution of current GNSS. An eight-satellite minimum is an increase from the four required for a pseudorange point solution, but the lack of atomic clocks on LEO communication satellites makes pseudorange observables much less accurate: pseudorange measurement errors would degrade from about 1 m Root Mean Square (RMS) per-axis to about 100-200 m RMS per-axis if the constellation has neither atomic clocks or a precise PRN ranging code.

Communication constellations try to minimize the overlap of individual downlink beams. This design approach reduces the power consumption and bandwidth self-interference of the constellations, thereby making them much more efficient as space-based communication systems. This fact of LEO communication constellations makes it unlikely that eight carrier Doppler shift measurements will be available simultaneously at any given ground location from a single constellation.

The lack of simultaneous signal availability can be compensated by using a tightly-coupled navigation Kalman filter that combines Doppler shift measurements with an Inertial Navigation System (INS) to provide a navigation solution with fewer than eight simultaneous

carrier Doppler shift measurements. One chapter of this work implements one of these filters and tests it using truth-model simulation data in order to help better understand the error drivers for a LEO constellation navigation system.

Another chapter of the work investigates different ways to incorporate the INS measurements into the filter. One popular method to incorporate INS measurements is called model replacement. In model replacement, the accelerations and angular rates measured by the INS are used in the dynamic propagation of the KF to propagate the position, velocity, and attitude states forward in time. Another possible method uses the INS measurements in the KF measurement update, which is a more traditional approach from a pure Kalman filtering standpoint. This investigation will provide a better understanding of when to use model replacement versus the more traditional approach from a Kalman filtering standpoint.

The final study of this work develops a simple analysis to determine the potential accuracy of a combined pseudorange and Doppler shift navigation system. The carrier-Doppler-shift-only batch filter point solutions of [42] lack the receiver clock accuracy of pseudorange-based systems. An analysis is developed that is a generalization to the GNSS Geometric Dilution of Precision (GDOP) analysis that uses only pseudorange to determine the potential position and clock accuracy of a receiver and a given set of pseudorange measurements. Noisy pseudorange measurements, when combined with the carrier Doppler shift measurements of [42], improve the receiver clock accuracy by multiple orders of magnitude over a solution using only carrier Doppler shifts. The DOP analysis will enable constellation designers to quickly understand how small changes in constellation design impact navigation accuracy in systems that rely on both pseudorange and carrier Doppler shift measurements.

1.3 Contributions

The main focus of this dissertation is the analysis of navigation using signals of opportunity from LEO satellite constellations. The major contributions to the field of satellite-based radio-navigation systems are:

a) Investigation of the feasibility of navigation using only carrier Doppler shift from LEO satellites and an INS [32].

b) Analysis of the impacts of INS quality, signal availability, and constellation design on navigation accuracy [32].

c) Mathematical description of using model replacement in a tightly-coupled INS/radio-navigation filter.

d) Mathematical description of using a Gauss-Markov model for acceleration and angular rates in a tightly-coupled INS/radio-navigation filter.

e) Comparison of the costs and benefits of using model replacement over a Gauss-Markov model in a tightly-coupled INS/radio-navigation filter.

f) Development of a DOP analysis for a combined pseudorange and carrier Doppler shift navigation system that performs batch filter point solutions based on such data [30].

g) Example constellation design of a combined pseudorange and carrier Doppler shift navigation system using a DOP analysis [30].

The work in this dissertation was performed by the author with significant guidance and advice provided by Dr. Mark L. Psiaki. All simulations and filters were performed in MATLAB.

1.4 Outline of Remainder of Dissertation

The remainder of this dissertation is organized as follows. Chapter 2 reviews related work to give context to this dissertation. Chapter 3 studies the feasibility of using carrier Doppler shift from LEO communication constellations with INS aiding to perform GNSS-like navigation with a tightly-coupled navigation KF. Chapter 4 analyzes different methods to implement a tightly-coupled INS/radio-navigation filter. Chapter 5 studies how the addition of noisy pseudorange measurements to a carrier-Doppler-shift-only navigation filter improves clock accuracy by developing a DOP analysis for a combined pseudorange and carrier Doppler shift navigation system. The final chapter, Ch. 6, summarizes the dissertation and its results and contributions.

Chapter 2

Review of Literature

This literature review discusses published works related to this dissertation and is broken into three sections. Each section focuses on research related to each of the three main chapters of this dissertation. The first section covers general LEO satellite navigation research. The second section reviews papers on the model replacement method and other ways of incorporating INS data in a tightly-coupled navigation filter. The final section reviews previous work on DOP analyses for satellite navigation systems, especially those that include carrier Doppler shift measurements in their analyses.

2.1 Navigation using Radio-Frequency Signals from LEO Satellites

The use of signals from LEO satellites to aid in navigation is not a novel idea and has been investigated by a number of researchers. Publications on this subject include [20], [38], [42], [45], [46], and [47].

The potential of leveraging massive LEO communication constellations for navigation purposes is investigated in [46] and [20]. In [46], the power improvements and reduction in the coverage area of LEO navigation constellations are discussed. The paper focuses on pseudorange-based methods which require hosted payloads on LEO satellites to provide suf-

ficiently accurate clocks for precise pseudorange measurements. The authors in [46] believe that LEO constellations can provide an independent navigation system or minimally, an augmentation to the current GNSS. The authors of [20] also investigate the use of LEO constellations for navigation. The main difference between [46] and [20] is that in [20], fused LEO GNSS is investigated, where measurements from LEO satellites are used in addition to GNSS to increase reliability and accuracy. The authors of [20] also perform more in-depth research about the potential error sources and anti-jam performance of LEO navigation systems.

More specific methods of using LEO constellations for navigation purposes are investigated in [42], [38], [45], and [47]. The main observable of [42], [38], and [47] is carrier Doppler shift while accumulated delta range is used in [45].

The author in [42] investigates a batch filter point solution using only carrier Doppler shift from LEO constellations in a similar manner to current GNSS pseudorange-only solutions. Doppler-shift-only point solutions require eight or more satellites as opposed to pseudorange-only point solutions that only require four or more satellites because four additional unknowns affect carrier Doppler shift measurements in addition to the three unknown receiver position components and the one unknown receiver clock offset. Three of the additional unknowns are the components of the receiver velocity vector, and the fourth additional unknown is the receiver clock offset rate. Reference [42] shows that navigation is possible using only Doppler shift from LEO constellations when eight or more satellites are available and that GNSS-like accuracy is achievable, except for the receiver clock offset accuracy. In [42], it is noted that the likelihood of observing eight or more measurements simultaneously is low due to the LEO constellation owners' desire to reduce reducing overlapping satellite coverage footprints in order to conserve on transmission power and bandwidth.

In [38], a tightly-coupled inertial navigation filter using accelerometer and rate gyro mea-

surements along with carrier Doppler shift measurements from LEO satellites is investigated. The system developed in [38] is implemented and tested with real data collected while flying a receiver onboard a drone. The results show notable improvement over using solely INS data.

The authors in [47] also use carrier Doppler shift from LEO satellites to try to improve navigation accuracy, but the main focus of [47] is the estimation of the Doppler shift of weak signals. This research could enable the collection of Doppler shift measurements from the side lobes of LEO satellite antennas. By acquiring and tracking these side lobes, additional simultaneous carrier Doppler shift measurements can be made which may enable a point solution to be used to navigate, as discussed in [42].

As opposed to a completely independent navigation system using LEO constellations, in [45] the benefits of augmenting current GNSS with accumulated delta range measurements from LEO satellites are investigated. The accumulated delta range measurements, which measure range-equivalent changes in the received beat carrier phase of a signal, provide much higher accuracy than traditional GNSS. LEO satellites also provide an improved geometric diversity due to the large number of satellites and their speed of travel overhead. The increase in accuracy and geometric diversity results in a LEO-augmented GNSS system that provides more integrity to navigation systems than only GNSS measurements.

All of the papers in this subsection show the potential of using LEO constellations as navigation systems. The wide variety of methods to use the LEO satellites' radio-navigation observables also indicates that further research is required to determine the best methods for utilizing the large number of LEO satellites that are planned to be launched in the coming years for navigation purposes.

2.2 Model Replacement versus Other Methods of using INS Data

Model replacement is a popular way to incorporate INS measurements into Kalman Filters (KF)s. The measurements are included in the dynamic propagation step of the KF in model replacement, which is non-standard in the general KF literature, where all measurement data are assimilated via measurement update calculations that are distinct from dynamic propagation calculations. In [37], [49], [17], [15], and [40] model replacement is used in combined INS/radio-navigation filters. GPS measurements and INS measurements are combined in [49], [17], [15], and [40]. Additional measurements from LEO satellites are used in conjunction with INS measurements in [37]. While each of these papers uses model replacement, many are not explicit in their mathematical representation of model replacement. The reasons for selecting model replacement over a more traditional Kalman filtering method are not discussed. Additionally, the papers do not acknowledge the fact that using measurements in the dynamic propagation step is not a standard method for using measurements in a KF.

The authors of [21] and [51], however, do not use model replacement for all of the INS measurements. The attitude is dynamically propagated without the INS rate gyro measurements in [21]. A Gauss-Markov model involving jerk is used to propagate the position, velocity, and acceleration in [51]. The accelerometer data are used in a traditional KF measurement update implementation. Reference [51] is a complicated paper that is difficult to understand. The reasons for using a Markov model over model replacement are not discussed, and the use of INS measurements in this manner is not a focus of the paper.

A good description of model replacement is found in [29]. The authors discuss spacecraft attitude determination. Thus, only the rate gyro measurements are used in the model replacement equations. Accelerometer measurements, a key part of navigation systems using

INSs, are not used in [29].

All of the papers in this subsection, except [29], attempt to combine INS and RF measurements to navigate. While several papers on this topic exist, most focus on the navigation results of the work. The underlying equations and implementations of the KFs are not covered in detail. The reasons for using model replacement over a Markov model are not investigated. Additionally, the model replacement method is not well explained in most of the INS/radio-navigation papers.

2.3 DOP Analysis

In [36], a GDOP analysis for GNSS constellations is described. Similar DOP analyses can be found in virtually every reputable GNSS textbook. The GDOP analysis is a method of estimating the potential position accuracy using pseudorange measurements from a given set of satellites. The analysis is generally used for GNSS constellations.

Traditional GDOP is used to analyze the positioning accuracy of LEO constellations [39]. In this work, the GDOP analysis is extended to use only carrier Doppler shifts and pseudoranges to determine the position accuracy of navigation systems based on RF signals from LEO satellites. This concept is only briefly discussed in [39], and the assumption is made that the velocity of the receiver is known. The Doppler-only work in [39] references [2]. In [2], the authors attempt to create a Doppler-only GDOP analysis for GNSS satellites. It is initially assumed that user velocity and receiver clock are known in [2]. Later on these assumptions are relaxed. The final GDOP matrix with the relaxed assumptions is not explicitly derived. Without relaxing these assumptions, a true Doppler-only position solution can only be determined in specific cases. A full Doppler-only GDOP analysis that requires eight or more simultaneous carrier Doppler shift measurements is derived in [42]. This GDOP

analysis is used to analyze the potential navigation accuracy of LEO constellations. The unit issues created when solving a Doppler-only GDOP analysis are not mentioned in [2] but are resolved in [42].

No previous work has been found that performs a combined pseudorange and Doppler shift GDOP analysis with unknown position, velocity, receiver clock offset, and receiver clock offset rate. Each of the papers in this subsection makes strides in developing a more general GDOP analysis, but none develop an analysis that can be used with any combination of pseudorange and carrier Doppler shift measurements. The present work fills this gap.

Chapter 3

Navigation Using Doppler Shift from LEO Constellations and INS Data

3.1 Abstract

Absolute navigation using the downlink communication signals of massive Low Earth Orbit (LEO) constellations augmented by data from an Inertial Navigation System (INS) is considered. Lack of atomic clocks on-board LEO satellites requires the use of Doppler shift as a navigation observable. Furthermore, footprint limits of downlink signals' beams necessitate the use of a tightly-coupled INS/radio-navigation filter in order to compensate for the fact that it is not possible to measure carrier Doppler shift simultaneously from eight or more satellites. The navigation solution error is shown for a simulation which demonstrates the feasibility of combining measurements from LEO constellations and INS data to enable GNSS-like navigation capabilities. Additional simulations study how navigation solution error is affected by Inertial Measurement Unit (IMU) quality, signal availability, downlink spot beam steering protocol, and constellation characteristics.

3.2 Introduction

Global Navigation Satellite Systems (GNSS) have become an integral part of military and civilian infrastructure. A disruption of GNSS service would have significant negative impacts. Unfortunately, GNSS is vulnerable to attacks in the form of jamming and spoofing that could cause disruptions. In response, an executive order was issued that calls for the development of a navigation service that is not dependent on the Global Positioning System (GPS) [41]. In the coming years, a large number of Low Earth Orbit (LEO) satellites are slated for launch. Existing and new LEO constellations, designed to provide internet or other communication services anywhere in the world, may form the basis for an alternative to GNSS.

This paper proposes and studies a way to exploit the new massive LEO constellations. OneWeb and Starlink constellations have begun to launch large numbers of satellites into LEO with a plan to launch thousands more in the future. The Kuiper constellation, currently in planning stages, also envisions a large LEO constellation with satellite numbers on the order of thousands. These constellations are designed for communication purposes, but this paper leverages them to perform navigation. With the large number of satellites, navigation would be a trivial task if each satellite had an atomic clock similar to GPS and omnidirectional beacons that broadcast ranging codes and precise ephemerides. Unfortunately, this is not the case. Without an accurate clock, pseudorange measurements would have significant uncertainty due to the inability to accurately know the transmitter clock bias which would result in unacceptable navigation error. To overcome this problem, Doppler shift measurements that do not rely on atomic clock-level accuracy are utilized instead of pseudorange. Simultaneous carrier Doppler shift measurements from eight or more satellites enable a point solution to be determined [42]. This point solution is analogous to the navigation solution for pseudorange except that it solves simultaneously for eight scalar unknowns: the components of the position vector, the receiver clock offset, the components of the velocity vector, and

the receiver clock offset rate.

In [5], a detailed explanation of the errors in Doppler shift navigation can be found. While [5] uses a more complete Doppler shift model than most, it has some omissions that are mentioned in [42]. It is not obvious that an estimate of the receiver clock offset is needed when using only Doppler shift measurements because it is not obvious that clock offset affects such measurements. To see that it does, consider two receivers placed next to each other with the same velocity and the same clock offset rates, but different clock offsets. The two receivers would measure the same Doppler shift from a given satellite. Since the Doppler shifts are the same in each receiver, one might conclude that the receiver clock offset does not impact the Doppler shift. While the receivers do measure the same Doppler shift, each would believe that the Doppler shift was measured at a different time due to the different receiver clock offsets. The two receivers could use their receiver clock time difference for measuring a particular carrier Doppler shift as a means of deducing their relative receiver clock offset. This capability comes from the dependence of carrier Doppler shift on receiver clock offset. This paper's navigation filter must determine the receiver clock's offset relative to the LEO constellation "clock" that has been used to define all of the satellites' ephemerides. In [42], the effect of receiver clock offset on the Doppler shift measurement model is developed mathematically. This clock-offset-dependent measurement model is needed to enable the estimation of the user receiver clock offset relative to the constellation. Stated differently, the motion of satellites causes any observables, including carrier Doppler shift, to be affected by the true time, and the receiver's knowledge of the true time is affected by the clock offset. Thus, necessitating the inclusion of an estimate for the receiver clock offset. The receiver clock offset is only weakly observable, but the other seven quantities can be strongly observable and can be estimated to GPS-like accuracy with a properly designed system. Unlike typical GNSS that relies on highly accurate transmitter

clocks, a Doppler-only system only requires high transmitter clock stability. The lack of reliance on accurate transmitter clocks is one of the main benefits of a Doppler-only system. The navigation error is shown to depend on the geometric diversity of the line-of-sight vectors and the diversity of the rates of change of the line-of-sight vectors between the satellites and the receiver [42]. A high diversity of the rate of change of the line-of-sight vectors means that satellites are quickly traveling overhead in a multitude of directions. For polar constellations, this diversity may be low in some cases due to all the visible satellites traveling from South to North or North to South. Although there may only be one or two carrier Doppler shift measurements per sample, the diversity is increased over time as different satellites provide measurements.

Unfortunately, the nominal designs of the constellations' component satellites do not include omnidirectional beacons that can provide signals to any visible user. Therefore, it is unlikely that eight or more signals will be available at any given time. Constellations such as OneWeb and Starlink send their downlink communications signals in narrow beams whose footprint is small compared to an individual satellite's potential visible footprint. Although a given user may see 20 or more satellites from a given constellation above a 7.5 deg elevation mask angle, useable signals will be received from at most four satellites and often only from a single satellite. This is because the constellation designers minimize bandwidth overlap and power usage for their communication systems. It would be costly and inefficient to have many satellites pointing beams at a single location. A more detailed description of how satellites are selected to provide signals to users is discussed in further sections. Without eight or more visible signals, navigating with the point solution is not possible.

To overcome this problem, a tightly-coupled Inertial Navigation System (INS)/radio-navigation Kalman filter is proposed and analyzed. The filter used in this paper is an Extended Kalman Filter-like (EKF) implementation of a Square-Root Information Filter (SRIF) [9], and it uses

the multiplicative update for the attitude quaternion [25]. The Kalman filter fuses carrier Doppler shift measurements from the LEO satellites with inertial measurements from 3-axis rate gyros and accelerometers. Through the use of a tightly-coupled filter, a navigation solution can be found with fewer than eight simultaneous signals.

Prior work in [42] looks into the accuracy of a Doppler-only point solution and its Geometric Dilution of Precision (GDOP). In this work, this concept is further developed by implementing a tightly-coupled INS/radio-navigation filter that fuses INS data and carrier Doppler shift measurements. The fusion of satellite navigation observables and sensors has been studied extensively, e.g., see [24], [15], and [38]. The main focus of the first two papers is the fusion of inertial sensors with GPS data. Both papers use typical GPS measurements and augment them with accelerometer and rate gyro measurements from an INS. The present paper generalizes this to the fusion of an inertial sensor and any navigation observable from a LEO constellation. Reference [38] is similar to this paper in that it uses Doppler shift measurements from the LEO Orbcomm constellation combined with INS data [38]. A major difference between [38] and this work, is that in [38] GPS signals are initially available. During the experiment, GPS measurements are lost. Initialization with GPS allows for knowledge of satellite ephemeris and receiver clocks to be well known before the Doppler-only navigation solution begins. This work differs from [38] in that it does not use GPS measurements at any point. Another difference between this paper and [38] is that this paper assumes that the satellite ephemerides are known from sources external to the user receiver.

In [46], [45], [20], and [47], LEO satellites are used to aid navigation. In [46], the idea of using LEO broadband constellations for navigation is investigated. A large number of visible satellites significantly reduces the GDOP of a pseudorange-only LEO system [46]. The interest in LEO satellites shown in [46] is important, but the investigation here focuses on

Doppler-only navigation as opposed to pseudorange-based navigation. Therefore, specific results from [46] cannot be compared with this work directly. Another investigation into the navigation potential of LEO constellations is found in [45]. In [45], LEO satellites augment GNSS to provide high-integrity positioning through carrier phase measurements. The augmentation used in [45] differs significantly from the navigation system independent of GNSS developed in this work. GPS receivers and hosted navigation payloads on LEO satellites are investigated in [20]. GPS-like signals are produced by a hosted payload on LEO satellites in [20]. These high bandwidth and power signals could produce centimeter-level positioning accuracy [20]. In [47], weak Iridium signals provide Doppler shift measurements for positioning. Reference [47] focuses mainly on the acquisition and tracking of weak Iridium signals. This investigation focuses on the estimation algorithm used in a Doppler-only navigation system, not the acquisition and tracking of LEO signals. In contrast to [47], this work includes other LEO constellations that provide a larger number of visible signals, a higher geometric diversity of satellites, and a higher diversity of the rate of change of the line-of-sight unit direction vectors between satellites and the receiver than the Iridium constellation.

Other works, such as [42], [38], and [39] analyze the potential for LEO satellites to form a navigation system. In [42] and [39] the navigation error of different LEO constellations is compared. In this paper, the impacts of changing constellation parameters on navigation errors are investigated in more detail. Specifically, discussed are the maximum time between signal availability, certain of the constellations' spot beam steering protocols, and the effects of constellations' orbit designs such as inclination and the grouping of ascending and descending nodes. Details regarding these topics are presented in subsequent sections.

This paper is a further development of preliminary findings investigated in [31]. One major change is the use of more realistic receiver clock properties. This results in more realistic simulation results for all cases. Another change is the addition of a discussion on how the

diversity of satellite motion and geometry impacts navigation.

This paper makes two contributions to the development of a navigation system that is independent of GPS and other pseudorange-based Medium Earth Orbit (MEO) GNSS. First, it shows the feasibility of fusing LEO constellation Doppler shift measurements and inertial sensors to navigate with low signal visibility without the use of GNSS initially as in [38]. The first contribution of this paper is to further develop the concept of a Doppler-only navigation system by implementing a tightly-coupled INS/radio-navigation filter that examines how the estimation error of a Doppler-only system develops over time with a moving receiver and a recursive Kalman-time filter. The performance of this Kalman filter is studied using simulated data from different LEO constellations and Inertial Measurement Units (IMUs). Although a tightly-coupled filter with inertial sensors and satellite data is not a novel concept, few prior results combine this with LEO constellation Doppler shift measurements and none consider using only carrier Doppler shift from the large number of LEO satellites whose signals could be used when the new constellations have been fully populated. Second, this paper discusses the impact of various constellation parameters on navigation solution error. The parameters discussed include spot beam steering protocols, maximum time between signal availability, inclination, and grouping of ascending and descending nodes. Investigation of these parameters are major parts of the second main contribution of this paper. These investigations help inform LEO constellation owners on design choices that would aid a LEO navigation system.

This paper does not make contributions to the implementation of a Doppler-only navigation receiver. Thus, specifics on how Doppler shift measurements are acquired and details of signal tracking of satellites are not discussed. Future work may include these contributions, but lack of information about the new LEO constellations makes this difficult.

This investigation aims to convince LEO constellation developers that their communication

constellations could be used for navigation. Ideally, no changes would be required to the constellations, but analysis has shown how small changes in the constellation system could have a significant impact on navigation accuracy.

The remainder of the paper is organized as follows. The second section reviews the different LEO constellations, including Iridium, OneWeb, Starlink, and Kuiper. The third section presents the state vector and the dynamics model used by the Kalman filter. The fourth section develops the Doppler shift measurement model that is used by the Kalman filter. The fifth section explains the SRIF implementation of the Extended Kalman filter. The sixth section discusses the truth-model simulation that has been used to test the filter. The seventh section presents representative results. The eighth section investigates the impact of system design parameter variations on navigation solution error. The paper finishes with a summary and conclusions. An appendix follows at the end to give details about the measurement model Jacobian matrix.

3.3 LEO Constellations

This section reviews the properties of multiple LEO constellations that are considered in the analysis. Iridium being an older, fully-populated constellation has more readily available information in [14]. The Starlink, Kuiper, and OneWeb Constellations are newer. Therefore, the majority of the information about them has been found in Federal Communications Commission (FCC) technical documents, mainly [13], [12], and [1].

3.3.1 Iridium Constellation

The Iridium constellation consists of 66 satellites arranged in six orbital planes at an altitude of 780 km with an inclination of 86.4 deg [14]. An illustration of the Iridium constellation orbital planes is shown in Fig. 3.1.

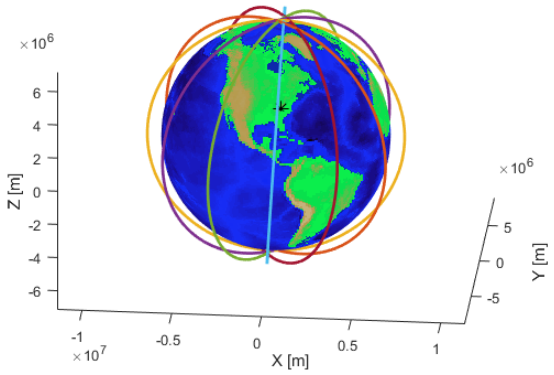

Figure 3.1: The satellite tracks of a representative Iridium constellation are shown with different orbital planes shown in different colors. The tracks are defined based on the information stated in the corresponding subsection.

Each satellite has 48 beams that cover a circular area with a diameter of about 4,700 km. The spot beams cover the entire visible footprint at all times and operate in the band 1616-1626.5 MHz [34]. By design, at least one satellite is visible at all times anywhere on Earth. Whereas a single satellite is not enough for navigation, it could be beneficial to use this constellation to increase the number of visible signals at any given time.

3.3.2 OneWeb Constellation

The OneWeb constellation was recently bought out of bankruptcy by a group of investors that included the UK government. One of the stated goals is to create a navigation system independent of the Galileo system [4]. All information regarding the constellation that is

used here has been found in [1]. Given that this information was published before the company was bought, it may be subject to change. The constellation is planned to have 720 satellites in 18 planes. Each satellite is planned to have an altitude of 1200 km and an inclination of 87.9 deg. An illustration of the OneWeb constellation orbital planes is shown in Fig. 3.2. The satellites are spaced evenly within each plane, and satellites in adjacent planes are offset in argument of latitude by half of the inter-satellite spacing, which creates a checkerboard pattern. For this paper, all ascending nodes were grouped, so that satellites in adjacent planes are orbiting in the same direction, except at two seams. Seams also appear in the Iridium constellation due to its polar orbits. Similar to the Iridium constellation, the

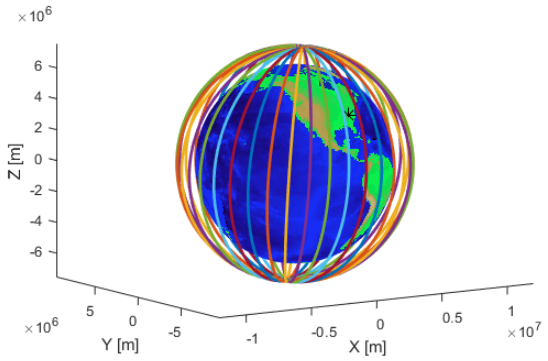

Figure 3.2: The satellite tracks of a representative OneWeb constellation are shown with different orbital planes shown in different colors. The tracks are defined based on the information stated in the corresponding subsection.

OneWeb constellation, normally only has one of 16 downlink beams available to a user at any given time. The beams are fixed relative to the satellite.

3.3.3 Starlink Constellation

One proposed version of the Starlink constellation has two main parts, [13]. The first is the LEO constellation, which will eventually consist of 2825 satellites with altitudes ranging from 1110 km to 1325 km. It will have inclinations ranging from 53 deg to 81 deg, with the majority being around 53 deg. Deployment of the Starlink constellation will proceed in phases. For this paper, only the initial deployment is considered. The initial deployment will consist of 1600 satellites with an inclination of 53 deg at an altitude of 1150 km. The initial installment of the Starlink LEO satellites is illustrated in Fig. 3.3. Due to the inclination of the Starlink constellation, no prominent seams are found like in the polar constellations. Seams do not occur because of the overlap of orbital tracks which can be seen in Fig. 3.3.

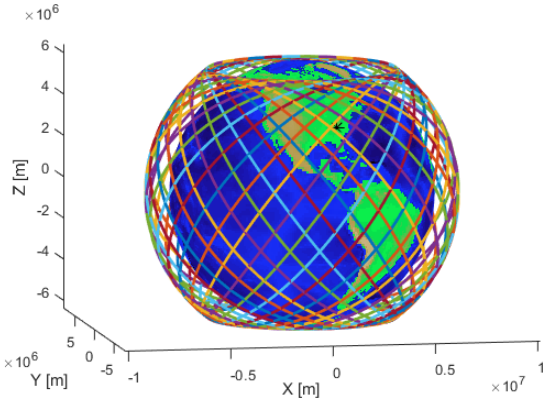

Figure 3.3: The satellite tracks of a representative Starlink constellation are shown with different orbital planes shown in different colors. The tracks are defined based on the information stated in the corresponding subsection.

The second part will be the Very Low Earth Orbit (VLEO) constellation which will consist of about 7500 satellites at altitudes around 340 km and inclinations ranging from 42 deg to 53 deg. All information regarding the Starlink constellation has been found in [13].

Each satellite will utilize a phased array antenna with multiple independently steerable spot

beams to provide internet service to customers. The full potential LEO satellite footprint area for a single satellite is about 4.5 million km^2, while an individual steerable spot beam has a footprint area of around 550 km^2. Similarly, a VLEO satellite will have a full footprint area of around 607,000 km^2 and a spot beam area of around 53 km^2 [13]. Based on these numbers, it is unlikely that the entire area in a footprint will be serviced by spot beams. This means that even though a satellite may be visible from the ground, there might not be a signal available to produce a measurement. It is unclear how Starlink plans to service the entire globe with this constellation design.

No information has been found about how the spot beams will be distributed within a footprint. Neither could any information be found about whether there will be several spot beams scanning the entire footprint to look for customers. Without this information, significant assumptions had to be made to simulate this constellation. These assumptions will be discussed later in the Truth-Model Simulation section.

3.3.4 Kuiper Constellation

Similar to the Starlink constellation, the Kuiper constellation planned by Amazon will consist of a large number of LEO satellites that send downlink signals in the Ka-band. Specifically, it will have 3,236 satellites at altitudes of 590, 610, and 630 km. The three orbital altitudes will have inclinations of 51.9 deg, 42 deg, and 33 deg, respectively. Also similar to the Starlink constellation, the Kuiper constellation will be deployed in phases. The initial deployment of the Kuiper constellation is depicted in Fig. 3.4, which includes 1156 satellites at 590 km altitude and 51.9 deg inclination.

Also similar to Starlink, the Kuiper constellation is designed to provide internet to users. All information used here regarding the Kuiper constellation has been taken from the FCC

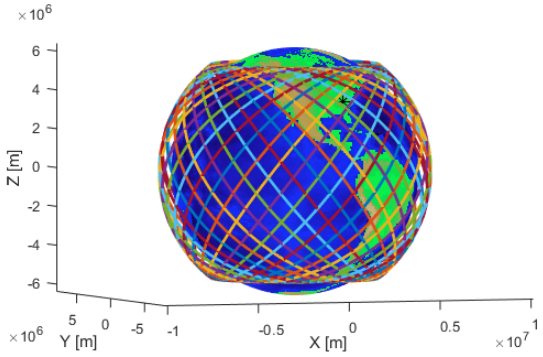

Figure 3.4: The satellite tracks of a representative Kuiper constellation are shown with different orbital planes shown in different colors. The tracks are defined based on the information stated in the corresponding subsection.

Technical Application, [12].

Each satellite will have a high gain, steerable, and shapeable phased array antenna with two main downlink beam types. The first is a narrow beam that has a visible area on Earth's surface of about 300 km^2, and the second larger beam has a footprint of about 500 km^2 at the cost of a 2 dB loss in power. The constellation and antenna design results in a "honeycomb" pattern on the Earth's surface in which only a single satellite will be transmitting a signal to a single cell or specific area on the Earth [12].

In the FCC document, there is a brief discussion about how the spot beams will be managed. In short, there will be a ground system that handles where each spot beam is pointing. This system is called the Kuiper Software Defined Network. There are no specific details on exactly how the system optimizes beam allocation and other factors. Therefore, the present study has made assumptions similar to those used for the Starlink constellation. They will also be discussed below.

One other note about the Kuiper constellation is that each satellite will have a Telemetry,

Tracking, and Command (TT&C) link. This link uses a wide-gain pattern antenna with a significantly larger coverage area of around 3,200,000 km^2 [12]. If this link were always active on every satellite, then it would eliminate the need for an IMU in the navigation filter due to the large number of visible satellites. With eight or more satellites visible, which would be the case in this situation, a GPS-like point solution could be used which would not require any additional sensors to determine a position fix. A similar system with a wide-angle downlink antenna was going to be used on Starlink but was removed for unknown reasons. Thus, it is not unreasonable to think that these TT&C links from the Kuiper satellites will not be available for use for navigation. Finally, it should be noted that, due to the inclinations of the Starlink and Kuiper constellations, satellite visibility at high latitudes will be significantly decreased.

3.4 Kalman Filter State Vector and Dynamics Model

This section defines the Kalman filter state vector and its dynamic model. The state vector used by the filter has 24 elements. It is

$$\underline{x} = \left[\underline{q};\ \underline{r};\ \underline{v};\ \Delta\underline{b}_{RG};\ \Delta\underline{b}_{ACC};\ \underline{b}_{RG_0};\ \underline{b}_{ACC_0};\ c\delta_R;\ c\dot{\delta}_R\right] \tag{3.1}$$

The first ten states characterize the user vehicle's attitude, position, and velocity. The quantity $\underline{q}$ is the unit-normalized attitude quaternion, which has four components and parameterizes the transformation from Earth-Centered, Earth-Fixed (ECEF) coordinates to IMU coordinates, $\underline{r}$ contains the three Cartesian components of the ECEF position of the receiver, and $\underline{v}$ represents the corresponding three components of the ECEF velocity of the receiver. Twelve of the states are IMU biases. The quantities $\Delta\underline{b}_{RG}$ and $\Delta\underline{b}_{ACC}$ each contain the three in-run stability biases of, respectively, the rate gyro and the accelerometer. The

next six bias states are the rate gyro and accelerometer turn-on repeatability biases represented by $\underline{b}_{RG_0}$ and $\underline{b}_{ACC_0}$, respectively. Repeatability biases are similar to stability biases, except that they represent constant offsets that change only between successive turn-ons of the IMU, whereas stability biases are the bias components that can drift during a given data run of the IMU. The remaining two states are the range-equivalent receiver clock offset and its rate, respectively, $c\delta_R$ and $c\dot{\delta}_R$. As previously stated, the reason for including the receiver clock offset in the state vector for a Doppler-only Kalman filter may not be obvious to all practitioners, but its effect on the carrier Doppler shift measurement model is shown in [42], and this effect implies that the Kalman filter must estimate it.

Also used by the filter is the 23-element error state vector, $\Delta\underline{x}$.

$$\Delta\underline{x} = \begin{bmatrix} \Delta\underline{q} \\ \underline{r}_{true} - \underline{r} \\ \underline{v}_{true} - \underline{v} \\ \Delta\underline{b}_{RGtrue} - \Delta\underline{b}_{RG} \\ \Delta\underline{b}_{ACCtrue} - \Delta\underline{b}_{ACC} \\ \Delta\underline{b}_{RG_0true} - \Delta\underline{b}_{RG_0} \\ \Delta\underline{b}_{ACC_0true} - \Delta\underline{b}_{ACC_0} \\ c\delta_{Rtrue} - c\delta_R \\ c\dot{\delta}_{Rtrue} - c\dot{\delta}_R \end{bmatrix} \tag{3.2}$$

It has one fewer element because it uses the 3×1 multiplicative quaternion error state, $\Delta\underline{q}$, such that

$$\underline{q} = \underline{q}_{error} \otimes \hat{\underline{q}} \tag{3.3}$$

where

$$\underline{q}_{error} = \begin{bmatrix} \Delta\underline{q} \\ 1 \end{bmatrix} \frac{1}{\sqrt{1 + \Delta\underline{q}^T \Delta\underline{q}}} \tag{3.4}$$

In Eq. (3.3), $\otimes$ represents quaternion multiplication, $\hat{\underline{q}}$ represents the estimated quaternion, and $\underline{q}$ represents the true quaternion [25]. The error state is used in conjunction with the square-root information matrices that will be discussed in subsequent sections.

3.4.1 Clock Offset Dynamics

The receiver clock offset model has two states. Each state is driven by process noise in the clock offset dynamics model. The discrete-time dynamics model for the clock offset and the clock offset rate takes the following form:

$$\begin{bmatrix} (c\delta_R)_{k+1} \\ (c\dot{\delta}_R)_{k+1} \end{bmatrix} = \begin{bmatrix} 1 & \frac{\Delta t}{1+\dot{\delta}_{Rk}} \\ 0 & 1 \end{bmatrix} \begin{bmatrix} (c\delta_R)_k \\ (c\dot{\delta}_R)_k \end{bmatrix} + \begin{bmatrix} (\nu_{clck1})_k \\ (\nu_{clck2})_k \end{bmatrix} \tag{3.5}$$

where the subscript $()_k$ indicates quantities that apply at discrete-time Kalman filter sample time t_k or for the sample interval from t_k to t_{k+1} and the subscript $()_{k+1}$ indicates quantities that apply at discrete-time Kalman filter sample time t_{k+1}. Note that t_k and t_{k+1} are both erroneous receiver clock times. The quantity $\Delta t = t_{k+1} - t_k$ is the sample interval of the receiver, and the terms ν_{clck1} and ν_{clck2} are, respectively the receiver clock offset and offset rate random process noise terms that apply for this sample interval. Both process noise terms are modeled as being Gaussian random variables with means of zero. Their covariance matrix depends on the minimum root Allan variance of the clock, σ_{av}, and on the time delay at which this minimum occurs, τ_{min} [10]. These values can be used to determine two

parameters h_0 and h_{-2} as follows.

$$h_0 = \sigma_{av}^2 \tau_{min} \tag{3.6}$$

$$h_{-2} = \frac{3h_0}{4\pi^2 \tau_{min}^2} \tag{3.7}$$

Both of these equations can be derived based on the model in [10] and are used along with Δt to determine the process noise covariance matrix for the clock states, which is defined in [10].

3.4.2 Dynamics Based on IMU Model Replacement

Model replacement is used to describe the evolution of the state. In model replacement, accelerometer and rate gyro measurements from the IMU are used in the dynamic propagation of the state. Unlike typical measurements in a measurement update, the accelerometer and rate gyro measurements are used in the dynamic propagation step to propagate the attitude, position, and velocity states. Therefore, their measurements cannot be used again in the measurement update step of the filter. For more information on model replacement see [29] and [17].

The IMU model will comprise of a dynamic model that accounts for measurement errors. Counter-intuitively, these measurement errors are not treated as measurement errors when using model replacement. Instead, some give rise to states and some become process noise. Measurements from an IMU have biases in them as well as white-noise error components. These biases need to be estimated as part of the Kalman filter state because the Kalman filter uses them in the IMU model replacement process. The equation used to correct for

the biases and, in theory, for the white process noise is as follows.

$$\underline{y}_{IMUcorr_k} = \underline{y}_{IMU_k} - \underline{\beta}_{IMU_k} - \underline{\nu}_{IMUk} \tag{3.8}$$

where $\underline{y}_{IMUcorr_k}$ is the corrected measurement, $\underline{y}_{IMU_k}$ is the raw measurement, $\underline{\beta}_{IMU_k}$ is the IMU bias vector, and $\underline{\nu}_{IMUk}$ is the IMU white noise vector. The latter vector becomes part of the Kalman filter's process noise when using the model-replacement approach. Each of the vectors above has six elements, one for each of the three axes of the rate gyro and one for each of the three axes of the accelerometer. The bias vector is defined as follows.

$$\underline{\beta}_{IMU} = \begin{bmatrix} \Delta\underline{b}_{RG} + \underline{b}_{RG_0} \\ \Delta\underline{b}_{ACC} + \underline{b}_{ACC_0} \end{bmatrix} \tag{3.9}$$

The state vector has six bias states associated with the rate gyro and six more associated with the accelerometer. The first three of each are related to the in-run stability of each sensor, which are denoted as $\Delta\underline{b}_{RG}$ and $\Delta\underline{b}_{ACC}$, respectively. The dynamics models for these states are as follows.

$$\Delta\underline{b}_{RG_{k+1}} = e^{\frac{-\Delta t}{\tau_{RG}}} \Delta\underline{b}_{RG_k} + \underline{\nu}_{bRGk} \tag{3.10}$$

$$\Delta\underline{b}_{ACC_{k+1}} = e^{\frac{-\Delta t}{\tau_{ACC}}} \Delta\underline{b}_{ACC_k} + \underline{\nu}_{bACCk} \tag{3.11}$$

where the two τ parameters are the time constants of the first-order Markov processes that model the time correlation in each respective axis of the rate gyro bias and the accelerometer bias. Both have units of seconds. The two $\underline{\nu}$ terms are white noise.

The other six bias terms are the turn-on repeatability terms. They have much simpler

dynamics models. They are modeled as being constants:

$$(\underline{b}_{RG_0})_{k+1} = (\underline{b}_{RG_0})_k \tag{3.12}$$

$$(\underline{b}_{ACC_0})_{k+1} = (\underline{b}_{ACC_0})_k \tag{3.13}$$

3.4.3 Quaternion, Position, and Velocity Dynamics Models based on IMU Model Replacement

The dynamic propagation of the attitude quaternion, the position, and the velocity relies on IMU measurements of angular rates from the rate gyro and accelerations from the accelerometer to propagate these components from time t_k to time t_{k+1}. The calculations that perform these states' propagation assumes that the k^{th} rate gyro and accelerometer measurements apply from time t_k to time $t_k + \Delta t/2$, and that the $(k+1)^{th}$ measurements apply from time $t_k + \Delta t/2$ to t_{k+1}. The propagation is calculated using explicit integration of the quaternion kinematic differential equation, which uses corrected rate gyro measurements. It takes the form:

$$\dot{\underline{q}} = \frac{1}{2}\Omega[\underline{y}_{RG} - (\Delta\underline{b}_{RG} + \underline{b}_{RG_0}) - \underline{\nu}_{RG} - A(\underline{q})\underline{\omega}_E]\underline{q} \tag{3.14}$$

where $\underline{y}_{RG}$ is the raw rate gyro measurement and $\underline{\omega}_E$ is the rotation rate vector of the Earth given in ECEF coordinates. The matrix $\Omega[\underline{\omega}]$ is defined as:

$$\Omega[\underline{\omega}] = \begin{bmatrix} 0 & \omega_3 & -\omega_2 & \omega_1 \\ -\omega_3 & 0 & \omega_1 & \omega_2 \\ \omega_2 & -\omega_1 & 0 & \omega_3 \\ -\omega_1 & -\omega_2 & -\omega_3 & 0 \end{bmatrix} \tag{3.15}$$

The 3×3 matrix $A(\underline{q})$ is the direction cosines matrix that rotates ECEF coordinates axes to IMU axes is defined as:

$$A(\underline{q}) = \begin{bmatrix} q_1^2 - q_2^2 - q_3^2 + q_4^2 & 2(q_1q_2 + q_3q_4) & 2(q_1q_3 - q_2q_4) \\ 2(q_1q_2 - q_3q_4) & -q_1^2 + q_2^2 - q_3^2 + q_4^2 & 2(q_2q_3 + q_1q_4) \\ 2(q_1q_3 + q_2q_4) & 2(q_2q_3 - q_1q_4) & -q_1^2 - q_2^2 + q_3^2 + q_4^2 \end{bmatrix} \tag{3.16}$$

where q_i denotes the i^{th} element of the quaternion. A more detailed description of the quaternion model and the INS mechanization can be found in [50].

The position/velocity dynamic propagation uses implicit trapezoidal integration of the following system of differential equations, which make use of the corrected accelerometer measurements:

$$\begin{aligned} \dot{\underline{r}} &= \underline{v} \\ \dot{\underline{v}} &= -2\underline{\omega}_E \times \underline{v} - \underline{\omega}_E \times (\underline{\omega}_E \times \underline{r}) \\ &\quad + \; A^T(\underline{q})[\underline{y}_{ACC} - (\Delta\underline{b}_{ACC} + \underline{b}_{ACC_0}) - \underline{\nu}_{ACC}] \\ &\quad + \; \underline{g}(\underline{r}) \end{aligned} \tag{3.17}$$

where $\underline{y}_{ACC}$ is the raw accelerometer measurement and $\underline{g}$ is the acceleration due to grav-

ity given in ECEF coordinates. A simple approximation for the gravity model is $\underline{g}(\underline{r}) \approx -\mu \underline{r}/(\underline{r}^T \underline{r})^{3/2}$ where μ is Earth's central gravitational parameter. A more robust model involving spherical harmonic coefficients of the EGM96 model is used in the filter. More details for the full model of $\underline{g}$ can be found in [27]. Both measurements at time t_k and t_{k+1} have to be corrected using the most recent IMU biases estimates and the current process noise estimate in conjunction with Eq. (3.8). The use of measurements from two different times creates an extra complication when performing SRIF calculations. This complication will be discussed further in subsequent sections.

3.4.4 General Form of Kalman Filter Dynamics Model

The full Kalman filter dynamics model takes the following general discrete-time form after integration of Eqs. (3.14) and (3.17) using implicit trapezoidal integration and using Eqs. (3.10 - 3.13) in their discrete form:

$$\underline{x}_{k+1} = \underline{f}_k(\underline{x}_k, \underline{\nu}_k, \underline{\nu}_{k+1}) \tag{3.18}$$

where

$$\underline{\nu}_k = \begin{bmatrix} \underline{\nu}_{RGk} \\ \underline{\nu}_{ACCk} \\ \underline{\nu}_{bRGk} \\ \underline{\nu}_{bACCk} \\ (\nu_{clck1})_k \\ (\nu_{clck2})_k \end{bmatrix} \tag{3.19}$$

Equations (3.14) and (3.17) use rate gyro and accelerometer measurements respectively in accordance with the model replacement method when performing the trapezoidal integration.

The inclusion of noise state vectors from the k^{th} and $k+1^{th}$ samples is not typical in a normal filter. Both are included due to the assumptions made about the accelerometer and rate gyro measurements. The k^{th} measurements are assumed to apply from time t_k to $t_k + \Delta t/2$ while the $k+1^{th}$ measurements are assumed to apply from time $t_k + \Delta t/2$ to time $t_{k+1} + \Delta t/2$. This results in two accelerometer and rate gyro measurements being used in the model replacement method for the dynamic propagation of the state vector. A linearized dynamics model for the error state vector is defined via the equation:

$$\Delta \underline{x}_{k+1} = \tilde{F}_k \Delta \underline{x}_k + \tilde{\Gamma}_{kk} \underline{\nu}_k + \tilde{\Gamma}_{kk+1} \underline{\nu}_{k+1} \tag{3.20}$$

where $\tilde{F}_k$, $\tilde{\Gamma}_{kk}$, and $\tilde{\Gamma}_{kk+1}$ are computed by taking partial derivatives of $\underline{f}_k(\underline{x}_k, \underline{\nu}_k, \underline{\nu}_{k+1})$ with respect to, respectively, $\underline{x}_k$, $\underline{\nu}_k$, and $\underline{\nu}_{k+1}$ and then projecting the results from the 24-dimensional $\underline{x}_k$ state down onto the 23-dimensional error state, $\Delta \underline{x}_k$ through the use of the Ξ matrix at time steps k and $k+1$. The Ξ matrix is defined as:

$$\Xi(\underline{q}_k) = \begin{bmatrix} q_{4k} & -q_{3k} & q_{2k} \\ q_{3k} & q_{4k} & -q_{1k} \\ -q_{2k} & q_{1k} & q_{4k} \\ -q_{1k} & -q_{2k} & -q_{3k} \end{bmatrix} \tag{3.21}$$

where q_{ik} is the i^{th} element of the quaternion for the k^{th} state estimate. More details regarding the calculation of $\tilde{F}_k$, $\tilde{\Gamma}_{kk}$, and $\tilde{\Gamma}_{kk+1}$ are shown in Eqs. (3.37 - 3.40).

3.5 Kalman Filter Measurement Model

This section briefly reviews the Doppler shift measurement model and the atmospheric models used in the simulation and filter.

3.5.1 Carrier Doppler Shift Model

A typical carrier Doppler shift measurement model used in a GPS-based velocity solution is [36]:

$$-\lambda_i D_i = \frac{\hat{\rho}_i^T(\underline{v} - \vec{v}_i)\left(\frac{1+\dot{\delta}_i}{1+[\frac{a_i - \hat{\rho}_i^T \vec{v}_i}{c}]}\right) + c\dot{\delta}_R - c\dot{\delta}_i}{1 + \dot{\delta}_R} \tag{3.22}$$

where λ_i is the nominal carrier wavelength of the signal from the i^{th} satellite, D_i is the measured carrier Doppler shift, $\hat{\rho}_i$ is the unit direction vector from the satellite to the receiver, $\underline{v}$ is the unknown receiver velocity, $\vec{v}_i$ is the satellite's velocity, $\dot{\delta}_i$ is the satellite's transmitter clock offset rate, a_i accounts for the rotation of ECEF coordinates as the signal propagates, and $\dot{\delta}_R$ is the receiver clock offset rate.

This model works well for a GPS velocity solution, but it ignores the time derivatives of the ionosphere carrier phase advance and the neutral atmosphere delay. Neglect of these two terms may cause problems for a Doppler-only navigation solution. The magnitudes of the time derivatives of the atmospheric terms have not been studied. In the case that the impact is large, significant problems could arise in a navigation filter using only Doppler shift measurements if these effects are not modeled. To err on the side of caution, the decision was made to model these derivatives. To include these atmospheric effects a 5-point central difference derivative with respect to erroneous receiver clock time of Accumulated Delta Range (ADR) is used to model Doppler shift measurements. By taking a numerical

derivative of an equation with the atmospheric terms, the derivative of these terms are implicitly included in the model while not requiring the derivation of analytical derivatives. This model takes the form:

$$\begin{aligned} D_i &= (\frac{-1}{\lambda_i})\Bigg(\frac{ADR_i(t_k - 2\Delta_{FD}) - 8ADR_i(t_k - \Delta_{FD})}{12\Delta_{FD}} \\ &\quad + \frac{8ADR_i(t_k + \Delta_{FD}) - ADR_i(t_k + 2\Delta_{FD})}{12\Delta_{FD}}\Bigg) \\ &= h_{ik}(\underline{x}_k, t_k) \end{aligned} \tag{3.23}$$

The quantity Δ_{FD} is the nominal receiver clock time difference used in the finite difference derivative calculation. Reasonable values fall in the range of 0.1 to 0.25 seconds. The finite difference formula on the right-hand side of the first line of this equation serves to define the general measurement model function form on the right-hand side of the second line, $h_{ik}(\underline{x}_k, t_k)$. This computation uses the ADR measurement model at different times with state vectors that have been adjusted for the time differences. By using the finite difference derivative of an ADR model that includes the ionosphere and neutral atmosphere effects, the Doppler shift model accounts for the time derivative of these delays without actually having to calculate the complicated time derivatives of these terms. While Eqs. (3.22) and (3.23) appear different at first glance, all terms in Eq. (3.22) are implicit in Eq. (3.23) due to Doppler shift being proportional to the time derivative of ADR. The ADR equation takes the form:

$$\begin{aligned} ADR_i = \lambda_i\phi_i &= \sqrt{[\vec{r}_i - \underline{r}]^T[\vec{r}_i - \underline{r}]} + c\delta_R - c\delta_i \\ &\quad - c\delta_{IONO_i} + c\delta_{NA_i} + \lambda_i\beta_i + \lambda_i\nu_{\phi_i} \end{aligned} \tag{3.24}$$

The term ϕ_i is the beat carrier phase for the i^{th} satellite, $\vec{r}_i$ is the ECEF position of the

satellite, $\underline{r}$ is the ECEF position of the receiver, $-c\delta_{IONO_i}$ is the carrier phase advance in meters caused by the ionosphere, $c\delta_{NA_i}$ is the delay in meters caused by the neutral atmosphere, β_i is the beat carrier phase bias, and ν_{ϕ_i} is the noise in the beat carrier phase value. Multiplying the beat carrier phase by the wavelength of the signal results in the ADR. This is almost identical to the equation for pseudorange except for the reversal of the sign for the ionospheric term and the inclusion of the bias term. The ADR equation in Eq. (3.24) is used in the calculation of the Doppler shift model. It is not used as a measurement in the filter. The only observation the filter uses is carrier Doppler shift in Eq. (3.23). For more information about this model and related carrier Doppler shift models see [42].

3.5.2 Atmospheric Models

The atmospheric model involves two parts, the ionosphere carrier phase advance and the neutral atmosphere delay. The ionospheric model uses the eight parameters given in the GPS navigation message along with the Klobuchar model to determine the ionospheric carrier phase advance for a given satellite location and estimated vehicle location. The neutral atmosphere delay is calculated using the Saastamoinen Zenith dry and wet delays and the Ifadis dry and wet elevation mapping functions [33].

3.5.3 General Form of Kalman Filter Measurement Model

The full Kalman filter measurement model takes the following general discrete-time form:

$$\underline{z}_{k+1} = \underline{h}_{k+1}(\underline{x}_{k+1}) + \underline{w}_{k+1} \tag{3.25}$$

where $\underline{h}_{k+1}$ comes from Eq. (3.23) and

$$\underline{z}_{k+1} = \begin{bmatrix} -D_{1k+1} \\ \vdots \\ -D_{N_k k+1} \end{bmatrix} \tag{3.26}$$

is the $N_k \times 1$ vector of range-rate-equivalent measured carrier Doppler shifts, with N_k being the number of satellites whose carrier Doppler shifts have been measured at sample time t_{k+1}. The corresponding $N_k \times 1$ measurement model function is

$$\underline{h}_{k+1}(\underline{x}_{k+1}) = \begin{bmatrix} h_{1k+1}(\underline{x}_{k+1}, t_{k+1}) \\ \vdots \\ h_{N_k k+1}(\underline{x}_{k+1}, t_{k+1}) \end{bmatrix} \tag{3.27}$$

The $N_k \times 1$ measurement error vector is $\underline{w}_{k+1}$. It is assumed to be zero-mean Gaussian random noise with the covariance matrix:

$$R_{k+1} = \begin{bmatrix} (\lambda_{1k+1}\sigma_{D_{1k+1}})^2 & 0 & \dots & 0 \\ 0 & (\lambda_{2k+1}\sigma_{D_{2k+1}})^2 & \dots & 0 \\ \vdots & \vdots & \ddots & \vdots \\ 0 & 0 & \dots & (\lambda_{N_k k+1}\sigma_{D_{N_k k+1}})^2 \end{bmatrix} \tag{3.28}$$

where $\sigma_{D_{ik+1}}$ is the carrier Doppler shift measurement error standard deviation for the i^{th} satellite at sample time t_{k+1} for all $i = 1, \dots, N_k$.

The SRIF uses a normalized measurement vector and corresponding measurement model

function:

$$\underline{z}_{ak+1} = R_{ak+1}^{-T}\underline{z}_{k+1}$$
$$\underline{h}_{ak+1}(\underline{x}_{k+1}) = R_{ak+1}^{-T}\underline{h}_{k+1}(\underline{x}_{k+1}) \tag{3.29}$$

where R_{ak+1} is a Cholesky square-root matrix of the measurement error covariance matrix R_{k+1}, such that $R_{ak+1}^{\mathrm{T}}R_{ak+1} = R_{k+1}$. The matrix R_{ak+1}^{-T} is the transpose of the inverse of R_{ak+1}.

The linearized measurement model in terms of the error state vector that is used in the SRIF takes the form:

$$\Delta\underline{z}_{ak+1} = H_{ak+1}\Delta\underline{x}_{k+1} + \underline{w}_{k+1} \tag{3.30}$$

where $\Delta\underline{z}_{ak+1} = \underline{z}_{ak+1} - \underline{h}_{ak+1}(\bar{\underline{x}}_{k+1})$ is the *a priori* measurement error and the matrix H_{ak+1} is computed by taking the partial derivative of $\underline{h}_{ak+1}(\underline{x}_{k+1})$ with respect to $\underline{x}_{k+1}$ and then projecting the result from the 24-dimensional $\underline{x}_{k+1}$ state down onto the 23-dimensional error state, $\Delta\underline{x}_{k+1}$. The formula for H_{ak+1} is complicated. The analytic partial derivatives of Eq. (3.24) with respect to the state vector are numerically differentiated with respect to time using the same finite difference procedure as is in Eq. (3.23) to find H_{ak+1}. This is implemented in the code of the filter but is too complicated to show in its entirety in this paper. More information about H_{ak+1} can be found in the Appendix.

3.6 Square-Root Information Filter

The SRIF used in this analysis is an implementation of an Extended Kalman Filter. The main focus of this section is to highlight the differences between the SRIF used here and a

typical SRIF. Thus, only a brief overview of the equations used in an SRIF are given in this section. For more detailed information about the general SRIF see [9].

A standard SRIF consists of two main parts, the dynamic propagation and the measurement update. The dynamic propagation uses the *a posteriori* state and square-root information matrix at time t_k along with the state dynamics model and measurements from the IMU to propagate the state and square-root information matrices to time t_{k+1}. This results in an *a priori* state estimate and the corresponding square-root information matrix at sample time t_{k+1}. The outputs of the dynamic propagation provide the inputs to the measurement update if a measurement is available at time t_{k+1}. The measurement update uses the difference between the *a priori* modeled value of the measurement vector and the measurement itself to update the *a priori* state estimate and square-root information matrix to yield the *a posteriori* values at time t_{k+1}.

The SRIF involves using square-root information matrices instead of the error covariance matrix typically used in Kalman filters [9]. The square-root information matrix, $R_{\Delta\underline{x}_k\Delta\underline{x}_k}$, is related to the error covariance matrix $P_{\Delta\underline{x}_k\Delta\underline{x}_k}$ as follows:

$$R^{-1}_{\Delta\underline{x}_k\Delta\underline{x}_k} R^{-T}_{\Delta\underline{x}_k\Delta\underline{x}_k} = P_{\Delta\underline{x}_k\Delta\underline{x}_k} = E\{\Delta\underline{x}_k \Delta\underline{x}_k^T\} \tag{3.31}$$

where $E\{\ \}$ is the expectation operator.

This particular SRIF also computes an estimate of the process noise, $\underline{\nu}_k$, its square-root information matrix, and a cross-square-root information matrix for $\underline{\nu}_k$ and $\underline{x}_k$. The vector $\underline{\nu}_k$ is defined in Eq. (3.19). This vector has an associated square-root information matrix $R_{\underline{\nu}_k\underline{\nu}_k}$. The process noise covariance matrix is defined as $P_{\underline{\nu}_k\underline{\nu}_k}$:

$$R^{-1}_{\underline{\nu}_k\underline{\nu}_k} R^{-T}_{\underline{\nu}_k\underline{\nu}_k} + R^{-1}_{\underline{\nu}_k\underline{\nu}_k} R_{\underline{\nu}_k\Delta\underline{x}_k} R^{-1}_{\Delta\underline{x}_k\Delta\underline{x}_k} R^{-T}_{\Delta\underline{x}_k\Delta\underline{x}_k} R^{T}_{\underline{\nu}_k\Delta\underline{x}_k} R^{-T}_{\underline{\nu}_k\underline{\nu}_k} = P_{\underline{\nu}_k\underline{\nu}_k} = E\{\underline{\nu}_k \underline{\nu}_k^T\} \tag{3.32}$$

The SRIF also computes the coupling square-root information matrix, $R_{\underline{\nu}_k \Delta \underline{x}_k}$, which defines the effect of the uncertainty in $\Delta \underline{x}_k$ on the uncertainty in the process noise estimate, $\hat{\underline{\nu}}_k$. The matrix $R_{\underline{\nu}_k \Delta \underline{x}_k}$ is initialized as a matrix of zeroes. The associated cross-correlation matrix is defined as:

$$-R^{-1}_{\underline{\nu}_k \underline{\nu}_k} R_{\underline{\nu}_k \Delta \underline{x}_k} R^{-1}_{\Delta \underline{x}_k \Delta \underline{x}_k} R^{-T}_{\Delta \underline{x}_k \Delta \underline{x}_k} = P_{\underline{\nu}_k \Delta \underline{x}_k} = E\{\underline{\nu}_k \Delta \underline{x}_k^T\} \tag{3.33}$$

Due to the non-zero $P_{\underline{\nu}_k \Delta \underline{x}_k}$, the square-root information matrices, $R_{\Delta \underline{x}_k \Delta \underline{x}_k}$, $R_{\underline{\nu}_k \underline{\nu}_k}$, and $R_{\underline{\nu}_k \Delta \underline{x}_k}$ have to be determined by taking the Cholesky factor of a large block matrix. The square-root information matrices are defined via the equation:

$$\begin{bmatrix} P_{\underline{\nu}_k \underline{\nu}_k} & P_{\underline{\nu}_k \Delta \underline{x}_k} \\ P^T_{\underline{\nu}_k \Delta \underline{x}_k} & P_{\Delta \underline{x}_k \Delta \underline{x}_k} \end{bmatrix}^{-1} = \begin{bmatrix} R_{\underline{\nu}_k \underline{\nu}_k} & R_{\underline{\nu}_k \Delta \underline{x}_k} \\ 0 & R_{\Delta \underline{x}_k \Delta \underline{x}_k} \end{bmatrix}^T \begin{bmatrix} R_{\underline{\nu}_k \underline{\nu}_k} & R_{\underline{\nu}_k \Delta \underline{x}_k} \\ 0 & R_{\Delta \underline{x}_k \Delta \underline{x}_k} \end{bmatrix} \tag{3.34}$$

The current SRIF's dynamic propagation and measurement update involve computing the QR factorizations of large block matrices. These block matrices are similar to block matrices used in [9]. The differences are caused by the dependence of Eq. (3.20) on $\underline{\nu}_k$ and $\underline{\nu}_{k+1}$. Both equations for the QR factorization of the block matrices are shown below.

The dynamic propagation begins by propagating the state vector from the *a posteriori* estimate $\hat{\underline{x}}_k$ to the *a priori* estimate at the next time step, $\overline{\underline{x}}_{k+1}$. This is done by using the nonlinear dynamics model Eq. (3.35) evaluated at $\hat{\underline{x}}_k$, $\hat{\underline{\nu}}_k$, and $\overline{\underline{\nu}}_{k+1} = 0$ which takes the form:

$$\overline{\underline{x}}_{k+1} = \underline{f}_k(\hat{\underline{x}}_k, \hat{\underline{\nu}}_k, \overline{\underline{\nu}}_{k+1}) \tag{3.35}$$

Equation (3.35) is a restatement of Eq. (3.18) with the inputs and outputs being explicitly defined for use in the SRIF. The function $\underline{f}_k$ is the same as Eq. (3.18). It is found using implicit trapezoidal integration of Eqs. (3.14) and (3.17) with the already discretized Eqs.

(3.10 - 3.13). Then the linearized model, which takes the form:

$$\underline{x}_{k+1} = \overline{\underline{x}}_{k+1} + F_k(\underline{x}_k - \hat{\underline{x}}_k) + \Gamma_{kk}(\underline{\nu}_k - \hat{\underline{\nu}}_k) + \Gamma_{kk+1}(\underline{\nu}_{k+1} - \overline{\underline{\nu}}_{k+1}) \tag{3.36}$$

is used to develop the matrices used in Eq. (3.41). The quantities F_k, Γ_{kk}, and Γ_{kk+1} are the partial derivatives of f_k evaluated at $\hat{\underline{x}}_k$, $\hat{\underline{\nu}}_k$, and $\overline{\underline{\nu}}_{k+1} = 0$, which are the current estimates of the state and process noise vectors. These three matrices, F_k, Γ_{kk}, and Γ_{kk+1}, are denoted as $\tilde{F}_k$, $\tilde{\Gamma}_{kk}$, and $\tilde{\Gamma}_{kk+1}$ respectively, when they have been projected onto the error state. The projected matrices are defined as:

$$\tilde{F}_k = \begin{bmatrix} \tilde{F}_{q_k} \\ \tilde{F}_{x_k} \end{bmatrix} = \begin{bmatrix} \Xi(\overline{\underline{q}}_{k+1})^T F_{qq_k} \Xi(\hat{\underline{q}}_k) & \Xi(\overline{\underline{q}}_{k+1})^T F_{qx_k} \\ F_{xq_k} \Xi(\hat{\underline{q}}_k) & F_{xx_k} \end{bmatrix} \tag{3.37}$$

where $\tilde{F}_{q_k}$ is a 3×23 matrix that corresponds to the projected quaternion states, $\tilde{F}_{x_k}$ is a 20×23 matrix that corresponds to the projection of all non-quaternion states, Ξ is found using Eq. (3.21). The matrix F_k has been similarly partitioned into four parts defined as:

$$F_k = \begin{bmatrix} F_{qq_k} & F_{qx_k} \\ F_{xq_k} & F_{xx_k} \end{bmatrix} \tag{3.38}$$

where F_{qq_k} is a 4×4 matrix, F_{qx_k} is a 4×20 matrix, F_{xq_k} is a 20×4 matrix, and F_{xx_k} is a 20×20 matrix. In a similar manner, $\tilde{\Gamma}_{kk}$ and $\tilde{\Gamma}_{kk+1}$ are defined.

$$\tilde{\Gamma}_{kk} = \begin{bmatrix} \Xi(\overline{\underline{q}}_{k+1})^T \Gamma_{q_{kk}} \\ \Gamma_{x_{kk}} \end{bmatrix} \tag{3.39}$$

$$\tilde{\Gamma}_{kk+1} = \begin{bmatrix} \Xi(\overline{\underline{q}}_{k+1})^T \Gamma_{q_{kk+1}} \\ \Gamma_{x_{kk+1}} \end{bmatrix} \tag{3.40}$$

where $\Gamma_{q_{kk}}$ is the 4×24 partitioned matrix of Γ_{kk} associated with the quaternion and $\Gamma_{x_{kk}}$ is the 20×24 partitioned matrix of Γ_{kk} associated with all non-quaternion states. These matrices are then used in the square-root information matrix equations.

The next part of the dynamic propagation computes the square-root information matrices for the next sample as follows:

$$\begin{bmatrix} R^*_{\underline{\nu}_k \underline{\nu}_k} & R^*_{\underline{\nu}_k \underline{\nu}_{k+1}} & R^*_{\underline{\nu}_k \Delta \underline{x}_{k+1}} \\ 0 & \overline{R}_{\underline{\nu}_{k+1} \underline{\nu}_{k+1}} & \overline{R}_{\underline{\nu}_{k+1} \Delta \underline{x}_{k+1}} \\ 0 & 0 & \overline{R}_{\Delta \underline{x}_{k+1} \Delta \underline{x}_{k+1}} \end{bmatrix} = T_{ak} \begin{bmatrix} 0 & R_{\underline{\nu}_{k+1} \underline{\nu}_{k+1}} & 0 \\ \overline{R}_{\underline{\nu}_k \underline{\nu}_k} - \overline{R}_{\underline{\nu}_k \Delta \underline{x}_k} \tilde{F}_k^{-1} \tilde{\Gamma}_{kk} & -\overline{R}_{\underline{\nu}_k \Delta \underline{x}_k} \tilde{F}_k^{-1} \tilde{\Gamma}_{kk+1} & \overline{R}_{\underline{\nu}_k \Delta \underline{x}_k} \tilde{F}_k^{-1} \\ -\hat{R}_{\Delta \underline{x}_k \Delta \underline{x}_k} \tilde{F}_k^{-1} \tilde{\Gamma}_{kk} & -\hat{R}_{\Delta \underline{x}_k \Delta \underline{x}_k} \tilde{F}_k^{-1} \tilde{\Gamma}_{kk+1} & \hat{R}_{\Delta \underline{x}_k \Delta \underline{x}_k} \tilde{F}_k^{-1} \end{bmatrix} \tag{3.41}$$

where T_{ak} is an orthonormal matrix and where the submatrices in the large block matrix on the left-hand side of this equation are the outputs of this QR factorization along with T_{ak}. The large block matrix on the right-hand side of this equation is the input to the QR factorization. The block matrices on the diagonal of the left-hand-side matrix are all square and upper-triangular. The first column of the large block matrices on both sides of this equation is associated with the process noise estimate at time t_k, $\underline{\nu}_k$, the second column is associated with the estimate of the process noise at time t_{k+1}, $\underline{\nu}_{k+1}$, and the third column is associated with the error state vector, $\Delta \underline{x}_{k+1}$. Each square-root information matrix denoted with an R has two subscripts. These subscripts denote the two vectors associated with the matrix, with the first subscript designating the variable whose square-root information equation the matrix appears in and with the second subscript designating the variable whose residual difference from an estimate is multiplied by the corresponding matrix in the given square-root information equation.

The measurement update of the square-root information matrices also uses QR factorization

and is defined by the following standard equation:

$$\begin{bmatrix} \hat{R}_{\Delta\underline{x}_{k+1}\Delta\underline{x}_{k+1}} \\ 0 \end{bmatrix} = T_{bk+1} \begin{bmatrix} \overline{R}_{\Delta\underline{x}_{k+1}\Delta\underline{x}_{k+1}} \\ H_{ak+1} \end{bmatrix} \tag{3.42}$$

The update to the state vector starts with calculations that are defined by the following equation:

$$\begin{bmatrix} \Delta\hat{\underline{z}}_{xk+1} \\ \Delta\underline{z}_{rk+1} \end{bmatrix} = T_{bk+1} \begin{bmatrix} 0 \\ \Delta\underline{z}_{ak+1} \end{bmatrix} \tag{3.43}$$

where $\Delta\underline{z}_{ak}$ is defined immediately below Eq. (3.30), $\Delta\hat{\underline{z}}_{xk+1}$ is a non-homogeneous term in a transformed *a posteriori* state square-root information equation at sample $k+1$, and $\Delta\underline{z}_{rk+1}$ defines the residual error vector. Then the equation for the *a posteriori* estimate of the error state vector takes the form:

$$\Delta\hat{\underline{x}}_{k+1} = \hat{R}^{-1}_{\Delta\underline{x}_{k+1}\Delta\underline{x}_{k+1}} \Delta\hat{\underline{z}}_{xk+1} \tag{3.44}$$

This equation along with Eqs. (3.3) and (3.4) can be used to determine the estimate for the first four elements of the *a posteriori* state vector which denote the quaternion. The first three elements of $\Delta\hat{\underline{x}}_{k+1}$ are $\Delta\tilde{\underline{q}}_{k+1}$ which can be used with the multiplicative quaternion update that utilizes $\overline{\underline{q}}_{k+1}$, the current guess of the quaternion, with Eqs. (3.4) and (3.3), to find $\hat{\underline{q}}_{k+1}$, the updated guess of the quaternion. This update takes the form:

$$\hat{\underline{q}}_{k+1} = \Delta\hat{\underline{q}}_{k+1} \otimes \overline{\underline{q}}_{k+1} \tag{3.45}$$

where $\otimes$ represents quaternion multiplication, and $\Delta\hat{\underline{q}}_{k+1}$ is found by using:

$$\Delta\tilde{\underline{q}}_{4,k+1} = \begin{bmatrix} \Delta\tilde{\underline{q}}_{k+1} \\ 1 \end{bmatrix} \tag{3.46}$$

and

$$\Delta\hat{\underline{q}}_{k+1} = \frac{\Delta\tilde{\underline{q}}_{4,k+1}}{||\Delta\tilde{\underline{q}}_{4,k+1}||} \tag{3.47}$$

The remaining elements of the *a posteriori* state vector can be found by adding the corresponding element of the error state found in Eq. (3.44) to the *a priori* state vector $\overline{\underline{x}}_{k+1}$. This concludes the SRIF algorithm for a single time step.

3.7 Truth-Model Simulation

A truth-model simulation has been developed to test the Kalman filter. It models an aircraft flying in a figure-eight pattern over Blacksburg, Virginia. The simulation lasts about 16 minutes with a sampling frequency of 100 Hz. The flight path for the duration of the simulation can be seen in Fig. 3.5. All states from Eq. (3.1) have been simulated. Additionally, Keplerian elements and equations have been used to simulate the orbital positions and velocities of all satellites. The rate gyro and accelerometer measurements have been generated using a cubic spline that can be differentiated twice to deduce acceleration from the aircraft trajectory and using the assumption of coordinated flight to define the aircraft's attitude time history.

The coordinated turns of the aircraft cause losses of visibility of satellites as they fall below the elevation mask, 5 deg, of the receiver antenna in its own rolling and pitching antenna-

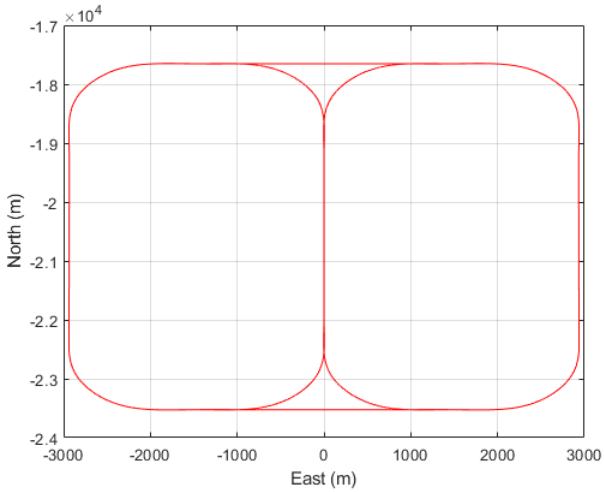

Figure 3.5: The figure-eight pattern flown by the simulated aircraft.

fixed coordinate system.

The receiver clock stability has been defined in terms of its minimum root Allan variance and the time delay at which this minimum occurs. Equation (3.5) defines the dynamic model for the receiver clock offset and offset rate for the simulation as well as for the Kalman filter. For this simulation, the minimum root Allan variance has been set to 10^{-10} seconds per second, and the time delay at which this minimum occurs, τ_{min}, has been set to 10 seconds.

For the initial deployments of the Starlink and Kuiper constellations described in Section II, an assumption had to be made about how often signals would be available to the receiver via steering of a spot beam towards the location of the receiver. An exponential distribution for the gap time between signal availability with a mean of 10 seconds per gap has been used to determine how long the receiver would go without seeing a signal. In addition to the exponential distribution, a maximum time gap between visible signals has been incorporated into the simulation. Thus, the probability distribution is not exactly an exponential distribution. The default maximum gap is 20 seconds, but the impact of changing this parameter on navigation error has also been investigated in Section 3.9.2. The use of the modified ex-

ponential distribution relies on the assumption that the constellation is constantly scanning the Earth in a coordinated manner for potential new hook-ups to the satellite network.

When a signal has been determined to be available from the Starlink or Kuiper constellation per the modified exponential time gap distribution, a steering protocol has been used to determine which visible satellite will steer a spot beam to scan the selected area. A detailed description of the different spot beam steering protocol cases can be found below. Once a satellite has been selected, a simulated Doppler shift measurement is generated. For simplicity, each measurement has been timed to occur exactly at an IMU sample time. Figure 3.6 shows a representative situation to further explain the measurement observation scenario. The blue lines show visible Iridium satellites with the blue circles indicating carrier Doppler shift measurements. For any time sample that an Iridium satellite is visible, a Doppler shift measurement is produced. The red lines indicate visible Starlink satellites with red circles indicating that a Doppler shift measurement is produced from that satellite at that sample time. Notice that a measurement is not produced for every sample even though multiple Starlink satellites are visible. The decision to produce a simulated Doppler shift measurement is made by sampling from a modified exponential distribution that describes the length of time between carrier Doppler shift measurements for the entire constellation. As this distribution changes, the number of red circles increases or decreases to reflect the change. Different Starlink satellites are selected at each sample a measurement is produced. The satellite is selected based on the spot beam steering protocol. The protocols define a probability distribution of satellite selection based on the off-nadir angle between the satellite and the user. For some cases, the same Starlink satellite is chosen to produce the measurements. In other cases, a different satellite is chosen every time.

Another assumption has been to neglect atmospheric modeling error effects by giving the filter the same atmospheric model parameters as the simulation. Finally, carrier Doppler

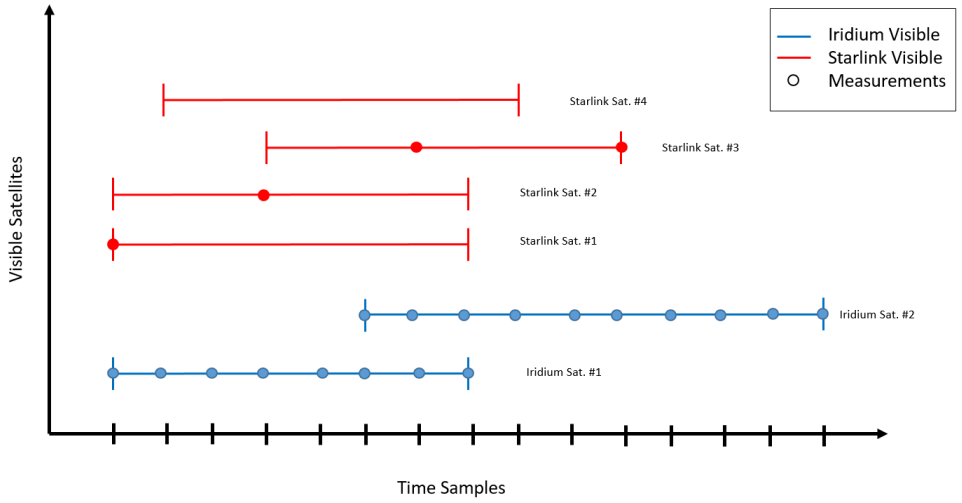

Figure 3.6: A possible scenario of how measurements are produced from given satellites. Blue lines show when Iridium satellites are visible. Blue circles indicate Doppler measurements are being made for that satellite at that sample. Red lines indicate a visible Starlink satellite with red circles indicating a Doppler measurement being produced.

shift measurement noise with 0.01 m/s range-rate-equivalent standard deviation has been added to each Doppler measurement. This is a reasonable estimate of the error standard deviation assuming the Iridium Carrier-to-Noise Density ratio (C/N0) is 68 dB-Hz over a 0.02032 s accumulation interval with a 0.1844 m wavelength and assuming the Starlink C/N0 is 46 dB-Hz over a 0.030 s interval with a 0.0256 m wavelength. The IMU measurements and Doppler shift measurements have then been stored for each sample time. Also, the true state vector has been saved to compare with the results from the SRIF.

3.8 Kalman Filter Performance on Simulated Data

3.8.1 Representative Results

The SRIF discussed above has been tested with data from the truth-model simulation. One simulation has included the entire initial deployment of the Starlink and the Iridium constel-

lations. The Iridium constellation is important because it provides constant measurements from one or two satellites. Even though the Starlink constellation has significantly more satellites than Iridium, only one measurement is provided by the entire Starlink constellation at any given time. The simulated IMU used in the particular simulation discussed here has the drift characteristics of the Honeywell HG4930 Micro-Electro-Mechanical Systems (MEMS)-grade IMU. The HG4930 has an angular random walk of 0.04 deg/hr.$^{1/2}$, a rate gyro stability of 0.25 deg/hr., and an accelerometer stability of 0.025 mg. A more complete listing of IMU parameters for the HG4930 can be found in [19]. The constellation-wide availability has followed the exponential distribution for gaps between availability with a maximum gap of 20 seconds.

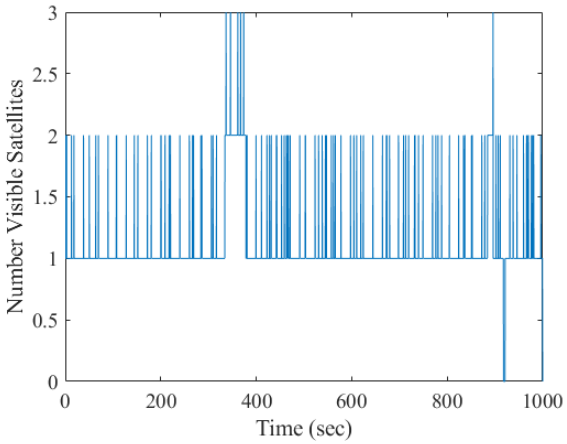

Figure 3.7: The number of visible signals over time for the simulated test case.

A plot of the signal availability versus time for this specific test case is shown in Fig. 3.7. In this figure, usually one, and for a brief moment, two signals are visible from the Iridium constellation. There is a brief moment when the number of visible signals drops to zero. This occurs when the simulated aircraft is in a coordinated turn which causes the Iridium satellite to fall below the antenna-relative elevation mask of the receiver resulting in a loss of signal. The short jumps in the number of available signals in Fig. 3.7 are the result of the

assumed Starlink spot beam scanning. Most of the brief jumps are from one to two satellites, except that they go from two to three satellites during the short intervals when two Iridium satellites are visible. Each Starlink signal availability window is assumed to be 30 ms long. The Doppler shift 1-σ measurement error is 0.01 m/s in the simulation.

The filter's results for position, attitude, and velocity error magnitude are plotted in Fig. 3.8. Each plot has two curves. The blue curve shows the magnitude of the error between the truth-

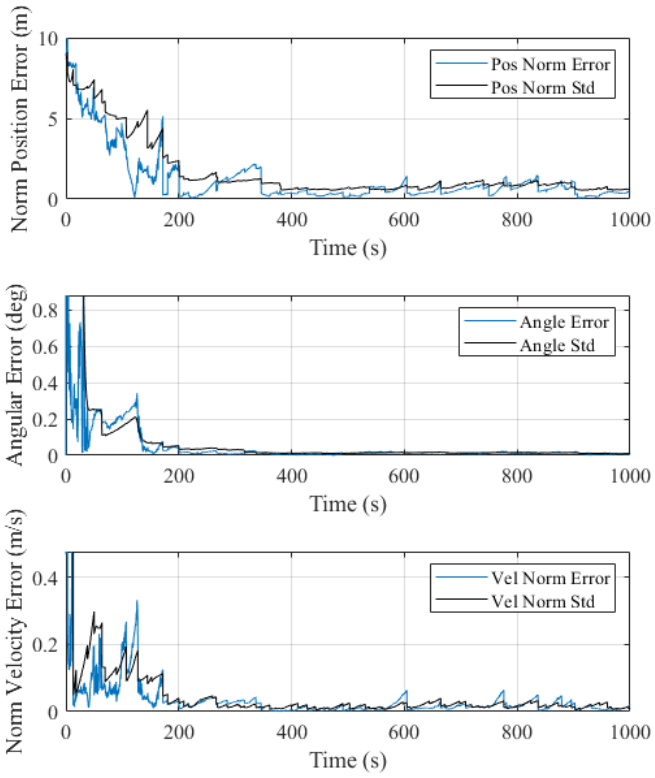

Figure 3.8: Example SRIF error time histories. Top: position error magnitude; Middle: attitude error magnitude; Bottom: velocity error magnitude.

model simulation and the filter results, and the black curve shows the 1-σ standard deviation that is computed by the filter based on computing its estimation error covariance matrix from its square-root information matrix. Note that the results in Fig. 3.8 are probably

optimistic relative to what is possible when using only Doppler shift measurements from these two LEO constellations. The filter does not include any atmospheric mis-modeling, transmitter clock frequency errors, or multipath errors. It has also been assumed that the satellites' ephemerides are known by the filter. This allows the filter to perfectly propagate a satellite's position and velocity to any time, although errors in the filter's knowledge of time can result in disagreement between the satellite position and velocity used in the truth-model and those used in the filter. These error source omissions result in a lower navigation solution error than is likely when using this system in a more realistic scenario. While the results may be optimistic, they are an indication of the feasibility of this method. It can be seen in the top plot of Fig. 3.8 that, once converged, the position estimate has an error magnitude below one meter. This shows that a tightly-coupled INS/radio-navigation filter using only carrier Doppler shifts measured from a LEO constellation has the potential to provide a navigation system independent of current GNSS. Without the carrier Doppler shifts from the LEO constellations, the errors would drift without correction in accordance with the IMU properties. The constant carrier Doppler shift measurements from the Iridium constellation reduce the rate of this drift. The carrier Doppler shift measurements from Starlink satellites produce the sharp reductions in the error magnitude.

Looking more closely at the velocity and position error plots, a pattern of increasing error followed by a correction can be seen repeatedly. This is due to the effect of the IMU between Starlink measurements. The IMU state drifts away from truth over time when there is a low number of available signals. When additional signals become available, the solution estimation accuracy is improved. This is the cause of the pattern seen in the plots in Fig. 3.8. A better IMU would result in a smaller increase in error when relying mainly on the IMU, and seeing signals more often would result in a reduction in the length of time of the increasing error.

A simplified study of the Kalman filter's ability to converge from elevated initial position error magnitudes has been carried out. It has considered initial position error magnitudes of 10, 100, and 1000 m to test whether the filter's steady-state accuracy is influenced by the accuracy of its initialization. These initial error levels, while large enough to probe the question of whether the filter owes much of its accuracy to a good initialization, do not attempt to probe fully the related issue of when nonlinearities would cause problems with filter convergence. They do, however, indicate that convergence issues due to nonlinearity do not occur with initial position errors up to 1000 m in magnitude.

Table 3.1: Root mean square (RMS) of steady-state position, velocity, and angular error magnitudes of the SRIF as a function of initial position error magnitude when using the Starlink and Iridium constellations.

Initial Pos. Error Mag. (m)	Steady-State RMS Pos. Error Mag. (m)	Steady-State RMS Vel. Error Mag. (m/s)	Steady-State RMS Angular Error Mag. (°)
10	2.3516	0.0390	0.0182
100	2.3385	0.0383	0.0173
1000	2.3627	0.0380	0.0143

For all cases in Table 3.1, the steady-state accuracy of the filter is not affected by the initial position error magnitude. Increases in the initial position error magnitude only lead to increases in the convergence times. In a similar study, initial receiver clock offset errors were increased to the order of one second. The Kalman filter still converged to the same level of steady-state accuracy regardless of the level of the initial clock offset error, up to one second.

Larger initial errors may result in convergence failure due to poor modeling of nonlinear effects in this EKF. It is well known that large initial errors can invalidate an EKF's linearization assumptions. The initial convergence problem might be resolved by the use of a pre-processing algorithm that used only Doppler shift measurements. A potential pre-processing algorithm, when eight or more Doppler shift measurements are available, can be

found in [42]. A fuller study of the convergence characteristics of the Doppler-only Kalman filter is left as a topic for research.

3.9 Performance Impact of System Design Variable Changes

This section investigates the impacts of IMU quality, signal availability, spot beam steering protocols, and constellation characteristics on navigation solution error. The first subsection explores the effects of IMU quality and aims to determine how the quality of the IMU can change the navigation error performance. The second and third subsections aim to demonstrate how changes in a constellation spot beam scanning procedure could have a significant impact on whether or not that constellation could be used for navigation. The fourth subsection examines the impact of constellation geometry and relative motion on accuracy.

3.9.1 IMU Quality Effects

In this section, three different IMUs are considered, each with a different quality. The first is the Honeywell I300 MEMS-grade IMU. MEMS-grade IMUs are generally smaller, lightweight, and low-power. Their position/velocity/attitude propagation inaccuracies tend to generate the largest amount of drift. The next IMU is the Honeywell HG1700 ring laser gyro tactical-grade IMU. These IMUs are generally bulkier and used in military applications such as in missiles. Finally, the last IMU investigated is the Honeywell HG5700 navigation-grade IMU. This IMU also uses ring laser gyros, and it is the largest and most accurate IMU.

For each IMU, simulated measurements are made and coupled with simulated carrier Doppler

shift measurements from various LEO constellations. The resulting simulated measurements are then processed by the SRIF. The results are compiled in Table 3.2.

Table 3.2: Root mean square (RMS) position error magnitudes (m) of the converged solution of the SRIF as a function of IMU quality and constellation. Use of the Iridium constellation is assumed for all cases. The "+" denotes that the OneWeb and Iridium satellites are traveling in the same direction while the "-" denotes that they are traveling in opposite directions.

Constellation	HGI300 (MEMS)	HG1700 (Tactical)	HG5700 (Nav.)
Starlink	1.6154	1.1533	0.3739
OneWeb^{+}	46.3533	40.2941	10.3330
OneWeb^{-}	7.2733	7.2887	6.8259
Kuiper	1.3832	1.2819	0.4315

For each result in Table 3.2, the maximum time between spot beam availability is 20 seconds. Also, the Iridium constellation is used in addition to the listed constellation. Thus, the first row includes both the Starlink constellation and the Iridium constellation in the simulation and filter. There are two rows for the OneWeb constellation. The first denoted with a "+", indicates the OneWeb and Iridium satellites are traveling in the same direction in their polar orbits. The second OneWeb row has a "-" to indicate that the OneWeb and Iridium satellites are traveling in opposite directions. This simulation used an equal probability spot beam steering protocol for the Starlink and Kuiper constellations, which will be discussed in detail later. The data shown are the Root Mean Square (RMS) position error magnitudes in meters of the converged solution of the filter. It is clear from the table that, as the quality of the IMU increases, the converged error decreases. Whereas the MEMS-grade IMU has an RMS error above one meter, this could be improved with a change in spot beam steering protocol. Also, this error is comparable to normal GPS C/A-code navigation error.

Looking at the different constellations, it appears that Starlink and Kuiper have the best error and OneWeb has the worst. It should be noted that this was not a Monte-Carlo analysis, so it is possible that changes in the geometry of the constellations relative to

different user locations could change the results. Thus, the data in Table 3.2 is only a representation of possible results. The Kuiper and Starlink results are comparable, with the Kuiper results slightly better for the MEMS-grade IMU and the Starlink results slightly better for the tactical-grade and navigation-grade IMUs. The difference between the two OneWeb cases may be explained as follows: Having the visible satellites of the two polar-orbiting constellations travel in opposite directions results in a wider variety of the rate of change of line-of-sight unit direction vectors. The diversity of the line-of-sight direction rate vectors has been shown to be important for a related method of Doppler-shift-based navigation, see [42]. The final subsection of this section further explores this question.

The better performance of the Starlink and Kuiper constellations might be explainable in terms of geometric diversity. The OneWeb constellation does not have steerable spot beams. Therefore, the receiver is only seeing a single orbital plane of satellites while Starlink and Kuiper can allow a larger geometric diversity of satellites with receivable signals, depending on their spot beam steering protocols. While there are differences between the constellations, the impact of different constellations is lessened as the quality of the IMU increases, especially in the case of the OneWeb and Iridium satellites traveling in the same direction.

3.9.2 Signal Availability Rate Effects

This section analyzes the impact of the frequency of signal availability on navigation solution error. To investigate this, the maximum gap time between Kuiper and Starlink spot beam scans has been varied in the truth-model simulation. While the maximum gap time between signals is changed, the underlying exponential distribution remains the same. Due to the constellation design, the OneWeb constellation is not included in this analysis because the OneWeb constellation has constant signal availability similar to Iridium based on a fixed

overlapping downlink beam pattern. The overlapping beam patterns provide continuous measurements as satellites enter and exit the visible area. Table 3.3 shows the results for the different constellations as they vary with the maximum gap between signal availability times.

Table 3.3: Root mean square (RMS) position error magnitude (m) of the converged solution of the SRIF as a function of the maximum time between spot beam scans.

Constellation	5(s)	20(s)	30(s)
Starlink	0.4669	1.6154	2.1871
Kuiper	0.4999	1.3832	2.1908

Similar to Table 3.2, Table 3.3 shows the RMS position magnitude error of the converged solution in meters. The Iridium constellation is also used in addition to the listed constellation. The Honeywell I300 MEMS-grade IMU is used in each simulation. Each column is labeled by the maximum gap in seconds that has been allowed between signal availability. Thus, a lower number indicates a signal is available more often on average. To relate this to Fig. 3.6, the values in the first row of Table 3.3 result in the red circles, indicating measurements, occurring at a minimum every 5, 20, or 30 seconds. The table shows that a lower maximum gap time results in a lower position solution error. This agrees with the idea that seeing signals more often results in a lower position error. Once again, one sees that the Starlink constellation has a similar error to the Kuiper constellation.

3.9.3 Spot Beam Steering Protocol Effects

This section explores how a constellation's protocol for steering its spot beams to a specific location on Earth affects navigation solution error. For the designer of a LEO constellation, this section provides guidance that will make the constellation's signals more suitable for carrier-Doppler-shift-based navigation. This section will demonstrate that the steering pro-

tocol of spot beams could have a significant impact on the ability to use a constellation for navigation. In particular, this section considers how the constellation decides which available satellite's spot beam is chosen to scan a given location on the Earth's surface that is due for scanning in order to check whether a currently unserviced communications customer is making a new request to link to the constellation. Four different candidate steering protocols are analyzed. For each protocol, the probability of a given satellite's spot beam being selected is determined based on the magnitude of the off-nadir angle, which is the angle between the nadir vector of the satellite and the vector from the satellite to the location on the Earth's surface that must be scanned. To aid in understanding, a simplified case is depicted in Fig. 3.9. Three different satellites are all sufficiently close to a point on the Earth that is scheduled for a scan. That point also happens to have an aircraft flying above it that would like to use the generated scan signal for carrier-Doppler-shift-based navigation even though the aircraft may not be a subscriber to the constellation's communications system. The three different off-nadir angles of the three different satellites are also shown, θ_1, θ_2, and θ_3.

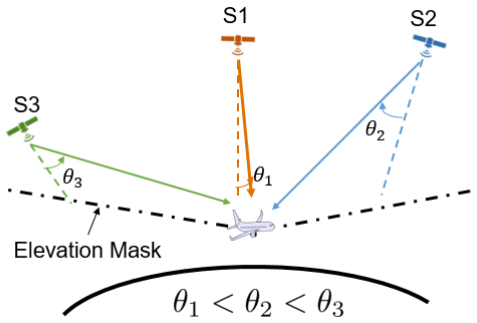

Figure 3.9: The simplified spot beam steering protocol scenario involving three satellites is shown.

In this scenario, Satellite 1 has the smallest off-nadir angle, Satellite 2 has an angle larger than Satellite 1, and Satellite 3 has the largest off-nadir angle. The first protocol analyzed is the case where the probability of a satellite's spot beam being selected is equal to that

of any other visible satellite that is close enough to service the point in question. Referring back to Fig. 3.6, in this scenario, each red line, representing a visible satellite, would have an equal probability of producing a measurement at any given epoch. In mathematical terms, and using the simplified scenario, the probability of a satellite's spot beam being selected would be:

$$P(S1) = P(S2) = P(S3) = \frac{1}{3}$$

Thus, the probability of Satellite 1 producing a measurement is equal to all other visible satellites. This protocol has been used to generate the results in Tables 3.2 and 3.3. In the next protocol, the satellite with the minimum off-nadir angle is always chosen. In other words, the satellite most directly overhead will always be chosen to scan that area. Referencing Fig. 3.6, a single red line, representing a visible satellite, would produce all of that constellation's measurements while it has the smallest off-nadir angle. All other red lines, representing visible satellites, would produce no measurements. In mathematical terms, this would translate to:

$$P(S1) = 1$$
$$P(S2) = P(S3) = 0$$

This second protocol is expected to be the worst-case protocol in terms of navigation accuracy due to its reduced geometric diversity of the satellites whose signals can be received from a given location.

The third protocol has a linearly decaying probability based on the magnitude of the off-nadir angle. This case gives a satellite with a smaller off-nadir angle a higher probability of being selected. For this protocol, Fig. 3.6 would have red circles, representing Doppler

measurements, distributed across multiple red lines, but red lines, representing satellites with smaller off-nadir angles, would be selected to produce measurements more often. In mathematical terms for the simplified example, this would yield:

$$P(S1) > P(S2) > P(S3)$$

Thus, the probability of Satellite 1 producing a measurement would be greater than the probability of Satellite 2 producing a measurement which would be greater than the probability of Satellite 3 producing a measurement. The fourth and final case is similar to the third case. There is also a linear probability based on the off-nadir angle, but there is a maximum off-nadir angle that cannot be exceeded. For the simplified example, in mathematical terms this would translate to:

$$P(S1) > P(S2)$$

$$P(S3) = 0$$

The probability of Satellite 3 scanning the location is set to zero because its off-nadir angle exceeds the maximum angle. Each of the above scenarios is used in the truth-model simulation with different constellations, and the results are presented in Table 3.4. Two of the cases in Table 3.4 have percentages describing them. The percentage indicates the amount of linearly decaying probability curve being used. For the 100% case, all satellites below the maximum off-nadir angle can be selected, but in the 75% case, only 75% of the maximum off-nadir angle follows the linearly decaying probability, beyond that the probability of selection drops to zero.

This table shows a clear worst protocol. The protocol in the last column, the one in which the minimum off-nadir angle is always chosen, has a significantly larger RMS of converged

Table 3.4: Root mean square (RMS) position error magnitude (m) of the converged solution of the SRIF as a function of spot beam steering protocol.

Constellation	Equal	Linear (100%)	Linear (75%)	Use Minimum-Angle Sat
Starlink	1.6154	1.0027	0.9678	6.6833
Kuiper	1.3832	1.1907	1.9174	5.4370

position error. This might seem somewhat surprising because the minimum off-nadir angle satellite has the highest rate of change of the line-of-sight vector. While this is true, the problem with this case is that the same satellite is being chosen repeatedly. This results in a low geometric diversity which causes a larger error. In all other cases, the satellite being chosen is changed from time to time which results in a better geometric diversity of the line-of-sight vectors and of their time rates of change. For a constellation designer, choosing the nearest satellite to scan an area is logical and tempting, but for navigation purposes, this may be a poor choice. All other cases do not show a significant accuracy difference, but once again this is not a Monte-Carlo analysis, so with more data there may be a distinction between the other three cases. One might expect that a linear probability with a certain maximum off-nadir angle would be the best choice because the satellites used would change giving good geometric diversity and the most nearly overhead satellites with the highest rate of change of the line-of-sight vector would be chosen more often. By further analyzing this, an optimal maximum off-nadir angle for each constellation that would result in the best position solution error may be found.

3.9.4 Case Study of the Effects of Diversity of Satellite Line-of-Sight Motion

Reference [42] demonstrates that the geometric diversity of the line-of-site rate vectors is an important factor in reducing the effective GDOP of Doppler-only point solutions based

on data from eight or more satellites. A comparison between the second and third lines of Table 3.2 indicates that the present IMU/Doppler-navigation concept may be affected in a similar way by the rate diversity of the line-of-sight vectors. This subsection considers this possibility further in the context of using the OneWeb constellation.

In the nominal configuration, the OneWeb constellation has adjacent planes' satellites traveling in the same direction, either North to South or South to North. The only exception is at two seams where the North to South and South to North traveling satellites are in adjacent planes. Figure 3.10 gives a visual representation of one of the seams. In Fig. 3.10, the red lines indicate orbital planes with satellites traveling from South to North, and the blue lines indicate orbital planes with satellites traveling from North to South. The black star's longitude is considered as the center of the seam for this analysis.

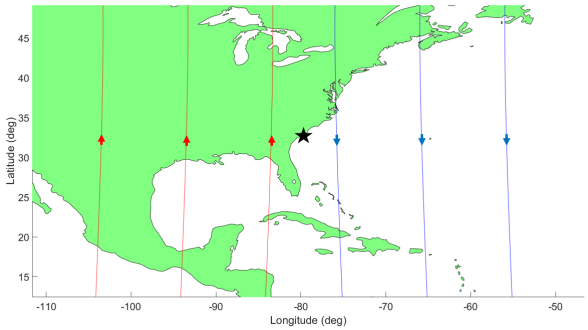

Figure 3.10: The ground track of six OneWeb constellation orbital planes. Red planes have satellites traveling from South to North, and blue planes have satellites traveling from North to South. The black star indicates the center of a seam.

The question of interest for the current subsection concerns whether the use of an IMU overcomes the problem, seen in [42], caused by a lack of diversity in the rate of change of direction vectors between the satellites and the receiver. This section aims to answer that question using the simulation and filter described above.

For this section, only the OneWeb constellation will be used, but the downlink beams used to determine carrier Doppler shift will be widened to be visible above a 27 deg elevation

mask from the surface of the Earth. This allows for more satellites to be visible, but only a single signal will be available at any given time, similar to how the Starlink and Kuiper constellation simulations worked above. In the previous OneWeb analysis, a receiver could only see satellites in a single plane unless the receiver was directly between two planes. In this section, satellites from multiple planes are visible regardless of the receiver's position.

To analyze the situation presented in [42], the simulated receiver is initially placed in different locations relative to the center of the seam of the OneWeb constellation, as depicted by the star in Fig. 3.10. The receiver is simulated as being on-board an aircraft flying in the pattern shown in Fig. 3.5. The position and range-equivalent clock estimates are initialized with errors on the order of 10s of meters. The velocity and range-rate-equivalent clock rate are initialized with errors on the order of a couple of meters per second. The attitude is initialized with errors on the order of half a degree. The initial convergence properties of a Doppler-only filter are not the focus of this study. Therefore, the initial errors are relatively low.

To parameterize the different locations, a longitudinal angular offset is used. Zero degrees is defined as the point directly between the two planes with satellites traveling in opposite directions. All distances are measured relative to this spot. This means that at an angular offset of around five degrees the receiver will be directly below one of the planes. In other words, as the angular offset increases, the ability to see satellites traveling in a direction opposite to the overhead satellites becomes less likely. Reference [42] shows that the navigation error increases significantly when signals are available from satellites only traveling in a single direction. Thus, a diversity in the rate of change of line-of-sight vectors between the satellites and a receiver is needed to perform accurate navigation using only carrier Doppler shift. In this section's analysis, the question of interest concerns whether or not the navigation error of the tightly-coupled filter increases significantly at a certain longitudinal angular

offset from the center of the seam. It is conjectured that this might occur when the signals from satellites traveling in the opposite direction to the most directly overhead satellites are no longer available.

Figure 3.11 shows the RMS position error magnitude of a number of simulation runs of the converged position error. Fifteen runs for each angular offset are simulated. Each run has different initial errors and different signals randomly selected from visible satellites. Every simulation uses the HG1120 MEMS IMU and the equal probability spot beam steering protocol discussed above. A maximum time of 0.5 seconds between each available signal is used, which should be noted as being significantly shorter than previous simulations. In Fig. 3.11, a significant increase in the RMS position error magnitude can be seen above a certain longitudinal angular offset from the center of the seam. Below an offset of around 10 deg, there is a navigation error on the order of meters. On the other hand, at larger offsets, the navigation error jumps significantly to tens of meters.

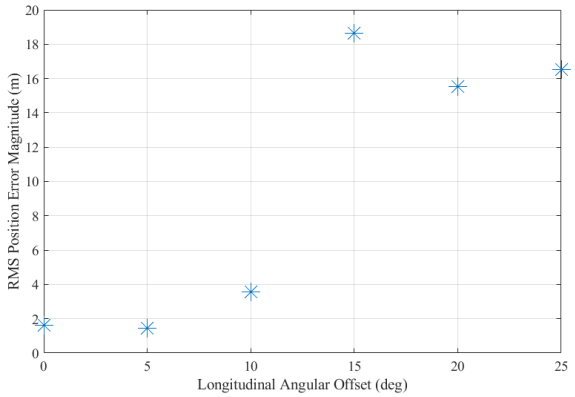

Figure 3.11: The RMS magnitude of the converged position error as a function of the longitudinal angle from the center of the seam.

The results shown in Fig. 3.11 agree with [42] and results from the IMU analysis given in Table 3.2. In the subsection that contains Table 3.2, it has been observed that, when OneWeb and Iridium satellites are traveling in the same direction, the navigation error is significantly

increased. These analyses show that an IMU does not obviate the need to have a diversity in the satellite geometry and the rates of change of the line-of-sight direction vectors between the satellites and the receiver. Also, it is clear that it would be beneficial for carrier Doppler shift navigation if the OneWeb constellation were to change the location of the ascending nodes of the orbits so that adjacent planes have satellites traveling in opposite directions for every combination of planes, not just at two seams. Without such a change, the navigation error using a carrier-Doppler-shift-only method would be significantly increased.

3.10 Summary and Conclusions

This paper has investigated a method for navigation independent of current GNSS. The method uses the carrier Doppler shifts of Radio Frequency signals from LEO satellites and inertial sensors. Through the use of a tightly-coupled INS/radio-navigation filter, the position, velocity, and attitude of a receiver INS sensor suite can be estimated. The choice of carrier Doppler shift as the radio-navigation observable has been dictated by the lack of atomic clocks on large LEO constellations and by the likely lack of spread-spectrum ranging signals. Although this concept has been studied before, this new study has considered the beneficial effects of having large constellations to provide carrier Doppler shift measurements. In theory, point solutions can be determined for position, clock offset, velocity, and clock offset rate solely from carrier Doppler shift measurements when eight or more satellites are visible. In practice, satellite downlink beam footprints dictate that the simultaneous reception of signals from eight or more satellites is unlikely. This study has considered whether the introduction of INS data and a tightly-coupled filter can remedy this lack of simultaneous availability and still exploit the opportunities afforded by the new large constellations.

Results based on data from a truth-model simulation show that sub-meter accuracy may

be possible when performing Doppler-only navigation if combined with a sufficiently high quality IMU and a reasonable spot beam steering protocol. It is clear from the data that a higher quality IMU results in a smaller converged navigation solution error, but a reasonable navigation solution is still possible even with a small MEMS-based IMU. The study made several optimistic assumptions and simplifications. These assumptions included no atmosphere mis-modeling, no ephemeris errors, no transmitter clock rate uncertainty, and no multipath error. Nevertheless, the encouraging simulation results obtained here may not degrade so much that this concept would become uncompetitive with current GNSS accuracy.

The different constellations have slightly different accuracies, but the differences are not significant except in the OneWeb cases. The data shows that more frequent signal availability results in a better solution, and that the steering protocols of spot beams could have a significant impact on navigation error. Ideally, the constellations' designers would make slight changes to their constellations in order to allow them to be used more effectively for navigation in addition to their primary use as communication systems.

3.11 Appendix: Details of the H_{ak+1} Matrix Derivation:

The H_{ak+1} matrix in Eq. (3.30) is complicated to derive analytically. It is defined as:

$$H_{ak+1} = \begin{bmatrix} \frac{\partial h_{1ak+1}}{\partial \underline{q}_k}\Xi(\overline{q}_k) & \frac{\partial h_{1ak+1}}{\partial \underline{r}_k} & \frac{\partial h_{1ak+1}}{\partial \underline{v}_k} & \frac{\partial h_{1ak+1}}{\partial \Delta \underline{b}_{RGk}} & \frac{\partial h_{1ak+1}}{\partial \Delta \underline{b}_{ACCk}} & \frac{\partial h_{1ak+1}}{\partial \Delta \underline{b}_{RG_0k}} & \frac{\partial h_{1ak+1}}{\partial \Delta \underline{b}_{ACC_0k}} & \frac{\partial h_{1ak+1}}{\partial (c\dot{\delta}_R)_k} & \frac{\partial h_{1ak+1}}{\partial (c\dot{\delta}_R)_k} \\ \vdots & \vdots & \vdots & \vdots & \vdots & \vdots & \vdots & \vdots & \vdots \\ \frac{\partial h_{N_k ak+1}}{\partial \underline{q}_k}\Xi(\overline{q}_k) & \frac{\partial h_{N_k ak+1}}{\partial \underline{r}_k} & \frac{\partial h_{N_k ak+1}}{\partial \underline{v}_k} & \frac{\partial h_{N_k ak+1}}{\partial \Delta \underline{b}_{RGk}} & \frac{\partial h_{N_k ak+1}}{\partial \Delta \underline{b}_{ACCk}} & \frac{\partial h_{N_k ak+1}}{\partial \Delta \underline{b}_{RG_0k}} & \frac{\partial h_{N_k ak+1}}{\partial \Delta \underline{b}_{ACC_0k}} & \frac{\partial h_{N_k ak+1}}{\partial (c\dot{\delta}_R)_k} & \frac{\partial h_{N_k ak+1}}{\partial (c\dot{\delta}_R)_k} \end{bmatrix} \tag{3.48}$$

The function h_{iak+1} is found using Eqs. (3.23), (3.24), (3.27), and (3.29). Since h_{iak+1} is already a numerical differentiation of Eq. (3.24), the full analytical expression for Eq. (3.48) is complex. For brevity, the entire analytical expression is not shown here, but it is implemented in the code that runs the filter. To determine the H_{ak+1} matrix, the derivative of Eq. (3.24) is found with respect to the state vector. Then, this derivative is numerically time-differentiated using 5-point finite differencing. This process results in the H_{ak+1} matrix when performed for every satellite producing a carrier Doppler shift measurement. Even the derivative of Eq. (3.24) is complicated and difficult to show in its entirety. Thus, only a part of this analytical expression will be shown below.

Before more details of the H_{ak+1} derivation are described, an approximation of the H_{ak+1} matrix is shown. This approximation is derived in [42]. It is derived for use in a GDOP analysis of a Doppler-only system. Note, this matrix is an approximation and may not be suitable for use in an implementation of the SRIF used in this work. It is shown to give an idea of the values this matrix may take. The approximate version of the H_{ak+1} matrix takes the form:

$$H_{ak+1} \approx \begin{bmatrix} 0 & (\dot{\hat{\rho}}^1)^T & (\hat{\rho}^1)^T & 0 & 0 & 0 & 0 & [(\hat{\rho}^1)^T\dot{\vec{v}}^1 + (\dot{\hat{\rho}}^1)^T\vec{v}^1]/c & 1 \\ \vdots & \vdots & \vdots & \vdots & \vdots & \vdots & \vdots & \vdots & \vdots \\ 0 & (\dot{\hat{\rho}}^{N_k})^T & (\hat{\rho}^{N_k})^T & 0 & 0 & 0 & 0 & [(\hat{\rho}^{N_k})^T\dot{\vec{v}}^{N_k} + (\dot{\hat{\rho}}^{N_k})^T\vec{v}^{N_k}]/c & 1 \end{bmatrix} \tag{3.49}$$

where $\hat{\rho}^i$ is the ECEF unit direction vector that points from the i^{th} satellite to the receiver, $\dot{\hat{\rho}}^i$ is the time rate of change of this unit direction vector, and $\dot{\vec{v}}^i$ is the ECEF acceleration of the i^{th} satellite. For more details on the formation of this approximation see [42].

Due to the additional states included in the SRIF of this paper, Eq. (3.49) has more columns than the matrix in [42]. The columns are rearranged to match the order of the state vector defined in Eq. (3.1).

In calculating the full analytical expression of H_{ak+1}, the partial derivatives of Eq. (3.24), with respect to each state element, need to be calculated. Many of these partial derivatives are zero. Others are more complicated. Additional complications and non-zero derivatives occur when the antenna has a moment arm relative to the IMU accelerometer triad. The filter discussed above, is capable of handling this complication. For the following derivation, it will be assumed that the IMU and antenna are co-located.

The partial derivatives of Eq. (3.24) with respect to position take the form:

$$\frac{\partial ADR}{\partial \underline{r}} = \frac{\partial ADR_{NoAtmos}}{\partial \underline{r}} - \frac{\partial (c\delta_{IONO})}{\partial \underline{r}} + \frac{\partial (c\delta_{NA})}{\partial \underline{r}} \tag{3.50}$$

where ADR represents a model for Accumulated Delta Range. The model for ADR without atmospheric effects is:

$$ADR_{NoAtmos_i} = \sqrt{[\vec{r}_i - \underline{r}]^T[\vec{r}_i - \underline{r}]} + c\delta_R - c\delta_i - \lambda_i\beta_i + \lambda_i\nu_{\phi_i} \tag{3.51}$$

This is similar to Eq. (3.24) except that the atmospheric terms have been omitted. The last two partial derivatives on the right-hand side of Eq. (3.50) are complicated to determine analytically. They include a significant number of chain rule applications that can be derived using the models in [33]. Similarly, the first term on the right-hand side of Eq. (3.50) is

found using a number of chain rule applications that are not expressed here, but can be derived using Eq. (3.51). Thus, Eq. (3.50) is simply a starting point for deriving a full analytical derivative of Eq. (3.24).

The partial derivative of Eq. (3.24) with respect to the receiver clock offset is:

$$\frac{\partial ADR}{\partial c\delta_R} = \frac{\partial ADR_{NoAtmos}}{\partial c\delta_R} - \frac{\partial (c\delta_{IONO})}{\partial c\delta_R} + \frac{\partial (c\delta_{NA})}{\partial c\delta_R} \tag{3.52}$$

The partial derivatives on the right-hand side of Eq. (3.52) also used the models in Eq. (3.51) and [33]. These partial derivatives also are determined using a combination of chain rule applications.

Under the given assumptions, all partial derivatives of Eq. (3.24) with respect to the remaining state vector elements are zero:

$$\frac{\partial ADR}{\partial \underline{q}} = 0 \tag{3.53}$$

$$\frac{\partial ADR}{\partial \underline{v}} = 0 \tag{3.54}$$

$$\frac{\partial ADR}{\partial \Delta \underline{b}_{RG}} = 0 \tag{3.55}$$

$$\frac{\partial ADR}{\partial \Delta \underline{b}_{ACC}} = 0 \tag{3.56}$$

$$\frac{\partial ADR}{\partial \Delta \underline{b}_{RG_0}} = 0 \tag{3.57}$$

$$\frac{\partial ADR}{\partial \Delta \underline{b}_{ACC_0}} = 0 \tag{3.58}$$

$$\frac{\partial ADR}{\partial c\dot{\delta}_R} = 0 \tag{3.59}$$

Equations (3.50) and (3.52) are just a starting point for deriving the full H_{ak+1} matrix. The above equations help in determining the partial derivative of Eq. (3.24) with respect to the state vector. The resulting derivative is then numerically time-differentiated using the

5-point finite differencing formula shown in Eq. (3.23). The final H_{ak+1} matrix is formed by stacking the numerical derivatives for each satellite that produces a carrier Doppler shift measurement and then left-multiplying the result by the matrix $R_{ak+1}^{-\mathrm{T}}$ as in Eq. (3.29).

Chapter 4

Tightly-Coupled INS/RF Navigation Filter to Compare Model Replacement and other Methods

4.1 Abstract

A study is conducted of algorithms to incorporate Inertial Navigation System (INS) measurements into a tightly-coupled INS/Radio Frequency (RF) navigation filter. The goal is to compare the traditional model replacement method with a Gauss-Markov model of acceleration and angular velocity states. Mathematical descriptions of both methods are developed in this study. Each method is implemented and analyzed using a Monte Carlo simulation. The Monte Carlo simulations indicate that all of the methods studied produce similar navigation accuracy. This study determines the costs and benefits of using each method for navigation.

4.2 Introduction

In the past, positioning through dead-reckoning of missiles, submarines, and other vehicles relied on Inertial Navigation Systems (INSs) [48], [18]. While accurate enough for short-duration flights, systems using only inertial measurements experience exponential error growth [15]. To reduce the error growth rate, INSs have been fused with external measurement sources such as pressure altimeters, magnetometers, and satellite signals. In, for example, [49], [17], [24], [15], and [51], Global Positioning System (GPS) signals are fused with INS measurements to improve navigation accuracy. Likewise, [38], [32], [8], and [37] fused INS measurements with signals from Low Earth Orbit (LEO) satellites to determine a navigation solution. In each of these papers, satellite measurements are fused with INS measurements in a tightly-coupled fashion. The term tightly-coupled indicates that raw Radio Frequency (RF) measurements are fused with INS measurements before a position solution is determined. In a loosely-coupled system, RF measurements are used to compute a position before fusing with INS measurements. An advantage of tightly-coupled systems is that they can determine a navigation solution without receiving the minimum number of RF measurements required for a point solution that depends entirely on radio-navigation data from a single epoch.

The tightly-coupled filters mentioned above have different methods for incorporating INS measurements. One method is called model replacement. Model replacement is the most popular method for incorporating INS measurements into a tightly-coupled navigation filter. Another approach is to use INS measurements in a measurement update of a Kalman Filter (KF) in the same manner as all other measurements are applied. Although a straightforward application of Kalman filtering principles to INS-aided navigation would use this latter approach, many tightly-coupled INS/RF navigation filters use the markedly different method known as “model replacement”.

In model replacement, a filter uses measured accelerations and angular rates in the dynamic propagation step rather than the measurement update step. This step typically uses a dynamics model to propagate the current state estimate to a future time. For example, a traditional Kalman filter for an aircraft navigation system might use a flight-dynamics model of the aircraft during this step. In place of a dynamics model, model replacement uses the INS measurement model equations in order to propagate the attitude, position, and velocity states forward in time. Model replacement accomplishes this by integrating angular rate and acceleration measurements. The authors of [38], [49], [17], and [15] use model replacement. In each of these papers, the reasons for using model replacement are not stated. This is likely due to the fact that model replacement has long been the norm in INS-based navigation systems. These papers also fail to emphasize that the dynamic propagation step uses measurements, which is unusual for a Kalman filter. Also, most do not mathematically describe the model replacement method well. The authors of [29] provide a reasonable description of model replacement, although they are concerned only with (spacecraft) attitude, not with position or velocity. Thus, only the model replacement equations for rate gyro measurements are shown.

One must think differently about INS measurements and the filter's state propagation if one wants to use these data in a traditional KF measurement update rather than in its dynamic propagation. Using INS measurements in the measurement update requires the creation of a dynamics model to propagate the estimated state forward in time. Such a navigation filter could be biased to a single type of moving system when using a specific dynamics model. For example, if such a filter were designed for a General Aviation aircraft, it might not be applicable to a large jetliner. Some classes of dynamics models, however, might enable a navigation filter to be applicable to a generalized set of moving systems. A Gauss-Markov model could be such a class of dynamics models. Therefore, this type of model is studied in

the present work. Its use, however, creates other challenges that this work will discuss.

In [21], [51], [7], and [35], INS measurements are used in a measurement update. In [21], attitude dynamic propagation without rate gyro measurements is performed. Instead, the rate gyro measurements are used in the measurement update step. An INS/GPS navigation filter in [51] uses a Gauss-Markov model for jerk. A navigation system using an INS is developed in [7] to navigate a mobile robot using Markov models to propagate states. INS measurements are fused with other sensors in a measurement update in [35] to navigate an autonomous underwater vehicle. While these papers use INS measurements in the traditional Kalman filter measurement update, they are in the minority of published works. Additionally, these papers do not discuss the reasons for using the INS measurements in a measurement update instead of using them in the standard model replacement mode.

This paper makes three contributions to the development of tightly-coupled INS/RF navigation filters. First, it mathematically describes the model replacement and Gauss-Markov model methods that can be used in the dynamic propagation step of the tightly-coupled Kalman filter. It emphasizes the differences between the two methods. Second, the pros and cons of using each method are discussed. Although neither of these two methods is novel, works in the current literature containing the mathematical description and comparing each method were not found. Third, this paper implements a filter using each of these methods. A truth-model simulation generates data, and a Monte Carlo simulation is performed on each filter implementation. By analyzing the results of the Monte Carlo analysis, this paper determines when it is reasonable to use model replacement or a measurement-update approach. This paper describes some of the challenges and benefits of using each method.

The remainder of the paper is organized as follows. The second section reviews the extended Kalman filter for discrete-time systems. The third section presents the model replacement and Gauss-Markov filter models, their dynamic propagation equations, and their measure-

ment models. The fourth section discusses the truth-model simulation and filter. The fifth section presents representative results from two different cases. The sixth section presents results from using the different algorithms to navigate a fast-moving airplane and a slow-moving wheeled vehicle. The seventh section is a summary and conclusions. The paper finishes with a section on potential future work.

4.3 Extended Kalman Filter Overview

This section reviews the basics of an extended Kalman filter. It does not define the equations in a KF in their entirety. Instead, its purpose is to ensure that terms such as *dynamic propagation* and *measurement update* are well defined. These terms are needed in order to understand the contributions of this work.

A Kalman filter is one method to combine INS and RF measurements to determine a receiver's position, velocity, and attitude. A KF has two phases. The first is the dynamic propagation step. In this phase, an *a posteriori* state estimate at time step k, $\underline{\hat{x}}_k$, is propagated to a future time step, $k+1$, using a dynamics model. The updated state estimate, $\underline{\overline{x}}_{k+1}$, is called an *a priori* state estimate at the next time step, $k+1$. State estimates are called *a priori* when they have not been conditioned on the most recent measurements, and they are called *a posteriori* when they have been conditioned on the most recent measurement data. The second phase of a Kalman filter is the measurement update step. In this phase, the state estimate is conditioned on information from the set of measurements that become available at sample $k+1$, $\underline{z}_{k+1}$. Conditioning of the state estimate on measurement data updates the state estimate from its *a priori* form at time step $k+1$ to its *a posteriori* form at the same time step. Changes to these two Kalman filtering phases are needed in order to switch from a model-replacement filter to one that uses INS data in a measurement update. Methods for

dealing with the needed changes and the effects of making such changes constitute most of the contributions of this paper.

The original KF assumes that all dynamics and measurement models are linear [23], but in the case of tightly-coupled INS/RF navigation filter, the dynamics and measurement models of the system are nonlinear. The Extended Kalman Filter (EKF) is one of the earliest Kalman filters that was developed for nonlinear systems. The first-order EKF uses linearizations of nonlinear functions about current estimates in order to enable the use of many of Kalman's original linear-system filter operations. An EKF can work poorly for problems with large uncertainties that extend beyond the valid regions of its linear approximations. For navigation filters, however, the EKF has proved reliable in many cases. Therefore, this paper concentrates its analyses entirely on first-order EKF forms of tightly-coupled INS/RF navigation filters. The underlying structure of the KF remains unchanged in an EKF, but the EKF requires additional steps in order to deal with the nonlinear models. The basic EKF algorithm described in this section serves to specify what constitutes a dynamic propagation step and a measurement update step. It does not contain a complete derivation. For a full derivation of the first-order and second-order EKF equations see [6].

The general forms of a discrete-time Kalman filter's nonlinear dynamics and measurement models are defined as:

$$\underline{x}_{k+1} = \underline{f}[k, \underline{x}_k, \underline{u}_k, \underline{v}_k] \tag{4.1}$$

$$\underline{z}_k = \underline{h}[k, \underline{x}_k] + \underline{w}_k \tag{4.2}$$

where $\underline{f}$ is the nonlinear dynamics model function, $\underline{x}_k$ is the system state, $\underline{u}_k$ is the known control input vector (if there is a control input), $\underline{v}_k$ is the random process noise vector, $\underline{h}$ is the nonlinear measurement model function, and $\underline{w}_k$ is the random measurement noise.

The process noise statistics are defined as:

$$E\{\underline{v}_k\} = 0 \tag{4.3}$$

$$E\{\underline{v}_k \underline{v}_j^T\} = \delta_{jk} Q_k \tag{4.4}$$

where δ_{jk} is the Kronecker delta function, Q_k is the process noise covariance matrix, and where $E\{\ \}$ indicates the expectation operator without conditioning on any of the measurements.

The measurement noise vector has the statistics:

$$E\{\underline{w}_k\} = 0 \tag{4.5}$$

$$E\{\underline{w}_k \underline{w}_j^T\} = \delta_{jk} R_k \tag{4.6}$$

where R_k is the measurement noise covariance matrix. Note, also, the measurement noise and the process noise are assumed to be uncorrelated so that $E\{\underline{w}_k \underline{v}_j^T\} = 0$ for all k and j.

A Kalman filter keeps track of a state estimate and its estimation error covariance matrix, or rather, an approximation of the latter quantity. It keeps track of two such pairs of quantities. The first pair constitutes the *a priori* state estimate at sample k and its covariance approximation:

$$\begin{aligned} \bar{\underline{x}}_k &= E\{\underline{x}_k | k-1\} \\ \bar{P}_k &= E\{(\underline{x}_k - \bar{\underline{x}}_k)(\underline{x}_k - \bar{\underline{x}}_k)^T | k-1\} \end{aligned} \tag{4.7}$$

where $E\{\ \ |k-1\}$ is the expectation operator conditioned on the measurement data up

through $\underline{z}_{k-1}$. The second pair constitutes the *a posteriori* state estimate at sample k and its covariance approximation:

$$\begin{aligned}\hat{\underline{x}}_k &= E\{\underline{x}_k|k\} \\ P_k &= E\{(\underline{x}_k - \hat{\underline{x}}_k)(\underline{x}_k - \hat{\underline{x}}_k)^T|k\}\end{aligned} \tag{4.8}$$

where $E\{\ \ |k\}$ is the expectation operator conditioned on the measurement data up through $\underline{z}_k$.

The EKF linearizes the two models in Eqs. (4.1) and (4.2) at each time step using a Taylor series expansion. The equations for the dynamic propagation phase of a first-order EKF are [6]:

$$\overline{\underline{x}}_{k+1} = \underline{f}[k, \hat{\underline{x}}_k, \underline{u}_k, 0] \tag{4.9}$$

$$F_k = \frac{\partial \underline{f}}{\partial \underline{x}}|_{[k,\hat{\underline{x}}_k,\underline{u}_k,0]} \tag{4.10}$$

$$\Gamma_k = \frac{\partial \underline{f}}{\partial \underline{v}}|_{[k,\hat{\underline{x}}_k,\underline{u}_k,0]} \tag{4.11}$$

$$\overline{P}_{k+1} = F_k P_k F_k^T + \Gamma_k Q_k \Gamma_k^T \tag{4.12}$$

This phase takes the *a posteriori* state estimate and its corresponding covariance matrix as inputs at sample k, and it calculates the *a priori* state estimate and its corresponding covariance matrix at sample $k+1$. The state covariance matrix update equation, Eq. (4.12), is the same as a linear Kalman filter. The differences from a linear KF only occur when computing the *a priori* state in Eq. (4.9) and the F_k and Γ_k matrices in Eqs. (4.10) and (4.11). The dynamic update phase propagates the state and its covariance matrix to the next sample time without using any external measurements.

The measurement update equations in the first-order EKF are defined as [6]:

$$\overline{\underline{z}}_{k+1} = \underline{h}[k+1, \overline{\underline{x}}_{k+1}] \tag{4.13}$$

$$\underline{\nu}_{k+1} = \underline{z}_{k+1} - \overline{\underline{z}}_{k+1} \tag{4.14}$$

$$H_{k+1} = \frac{\partial \underline{h}}{\partial \underline{x}}|_{[k+1, \overline{\underline{x}}_{k+1}]} \tag{4.15}$$

$$S_{k+1} = H_{k+1} \overline{P}_{k+1} H_{k+1}^T + R_{k+1} \tag{4.16}$$

$$W_{k+1} = \overline{P}_{k+1} H_{k+1}^T S_{k+1}^{-1} \tag{4.17}$$

$$\hat{\underline{x}}_{k+1} = \overline{\underline{x}}_{k+1} + W_{k+1} \underline{\nu}_{k+1} \tag{4.18}$$

$$P_{k+1} = \overline{P}_{k+1} - W_{k+1} S_{k+1} W_{k+1}^T \tag{4.19}$$

The two quantities, $\hat{\underline{x}}_{k+1}$ and P_{k+1}, are the key outputs of the measurement update step. All other variables are intermediate values. Similar to the EKF's dynamic propagation, the measurement update equations are the same as the linear KF except for the innovation vector, ν_{k+1}, and the H_{k+1} matrix. The measurement update step conditions the state and its covariance matrix on the most recent measurement data.

Notice that Eq. (4.14), in the measurement update phase, is the only equation that includes measurement data. Typically, a measurement update phase always follows a dynamic propagation phase, but there can be special model forms that sometimes have an empty "measurement" vector where this will not always be the case. These two phases can repeat for all $k = 1, 2, ..., N$ just as in a linear Kalman filter, where N is the number of time steps.

A Kalman filter needs to be initialized with an initial guess for the state vector and its covariance, unless one is working with an Information Filter or a Square-Root Information Filter (SRIF). Information filters allow for an infinite covariance, which translates into a zero-valued information matrix (the covariance inverse) or a zero-valued square-root infor-

mation matrix. A first-order EKF, however, requires some reasonable initial estimate and a reasonably small initial covariance of that estimate. Otherwise, it will run into problems due to the resulting poor performance of its linear approximations. The EKF's linearizations of the nonlinear system's equations can result in divergence of the filter if the current state estimate error is sufficiently large. This work assumes that a sufficiently accurate initial state estimate is used to initialize all of the tightly-coupled EKFs that it considers.

An SRIF version of an EKF is used for the work here and is described in [32]. A complete derivation of an SRIF can be found in [9]. For more information on Kalman filters and their derivations, see [6] and [9].

4.4 Models for the Use of INS Measurements in a Tightly-Coupled INS/RF Navigation Filter

This section discusses two different algorithms for the incorporation of INS data into an EKF for navigation. The two algorithms considered here are the model replacement algorithm and algorithms that use Gauss-Markov dynamics models instead of model replacement. In model replacement, the dynamic propagation step uses the INS measurement model in place of a traditional system dynamics model to propagate attitude, position, and velocity states. For the Gauss-Markov methods, the use of the INS measurements is restricted to the measurement update step. A Gauss-Markov model is used in the dynamic propagation step to propagate the position and velocity states and new acceleration states to the next sample time. There are two versions of this paper's Gauss-Markov model. One of them reverts to traditional INS model-replacement methods for the attitude state's dynamic model. The other one also applies Gauss-Markov techniques to the attitude dynamics model. The latter

filter model includes the rate gyro measurements in its measurement model, whereas the former filter does not. This section presents the model equations used in each method.

4.4.1 Model Replacement

Model replacement differs from the traditional Kalman filter measurement update because it uses measurements in the dynamic propagation step. Typically in this step, a dynamics model is used to propagate the estimated state values from the current sample time to the next sample time. The dynamics models are derived from the physics of the receiver's motion. They can be time-consuming and complicated to derive. In model replacement, the dynamic propagation of the attitude quaternion, the position vector, and the velocity vector relies on the integration of INS measurements. In this work, INS measurements are assumed to come from a strap-down INS, i.e., a 3-axis rate gyro and a 3-axis accelerometer that are hard-mounted to a fixed INS coordinate frame. Their outputs include a 3×1 vector of measured angular rates relative to inertial coordinates and a 3×1 vector of the measured difference between the inertial acceleration and gravity. The angular rates from the rate gyro and accelerations from the accelerometer are used to propagate the attitude, position, and velocity states from time t_k to time t_{k+1} in place of a specific system's dynamics model. In theory, the lack of a requirement for a specialized dynamics model results in a generalization of the dynamic propagation step to work with the motion of any type of system, ranging from a pedestrian to a submarine, a fighter jet, or a ballistic missile. A filter using model replacement will not include any *a priori* information about the expected receiver motion due to the lack of a specific dynamics model.

The model replacement filter considered in this paper estimates the following 24-element

state vector:

$$\underline{x} = \left[\underline{q};\ \underline{r};\ \underline{v};\ \Delta\underline{b}_{RG};\ \Delta\underline{b}_{ACC};\ \underline{b}_{RG_0};\ \underline{b}_{ACC_0};\ c\delta_R;\ c\dot{\delta}_R\right] \tag{4.20}$$

where $\underline{q}$ is the 4×1 unit-normalized attitude quaternion that characterizes the transformation from Earth-Centered Earth-Fixed (ECEF) to INS coordinates, $\underline{r}$ is the 3×1 ECEF position vector, and $\underline{v}$ is the 3×1 ECEF velocity vector. The next four vector components constitute 12 elements of the state vector and define the in-run stability and turn-on biases of the rate gyro and the accelerometer. The rate gyro and accelerometer in-run stability biases are defined as $\Delta\underline{b}_{RG}$ and $\Delta\underline{b}_{ACC}$, respectively. The turn-on biases for the rate gyro and accelerometer are defined as $\underline{b}_{RG_0}$ and $\underline{b}_{ACC_0}$, respectively. The last two states are the range-equivalent receiver clock offset, $c\delta_R$, and the range-rate-equivalent receiver clock offset rate, $c\dot{\delta}_R$.

The equations and dynamics models used in model replacement are described in [32]. Some of the equations are expanded upon here. The explicit integration of the quaternion kinematic differential equation uses rate gyro measurements. It takes the form [32]:

$$\dot{\underline{q}} = \frac{1}{2}\Omega[\underline{y}_{RG} - (\Delta\underline{b}_{RG} + \underline{b}_{RG_0}) - \underline{\nu}_{RG} - A(\underline{q})\underline{\omega}_E]\underline{q} \tag{4.21}$$

where the uncorrected rate gyro measurement is denoted as $\underline{y}_{RG}$, $\underline{\nu}_{RG}$ is the 3×1 Gaussian, white process noise vector that models the rate gyro's angular random walk error, and the Earth's ECEF rotation rate vector is $\underline{\omega}_E$. The formula for the 4×4 matrix $\Omega[\underline{\omega}]$ is [50]:

$$\Omega[\underline{\omega}] = \begin{bmatrix} 0 & \omega_3 & -\omega_2 & \omega_1 \\ -\omega_3 & 0 & \omega_1 & \omega_2 \\ \omega_2 & -\omega_1 & 0 & \omega_3 \\ -\omega_1 & -\omega_2 & -\omega_3 & 0 \end{bmatrix} \tag{4.22}$$

Note that the angular velocity argument of the $\Omega[\ \ ]$ matrix in Eq. (4.21) is the filter's best estimate of the rotation rate of the INS relative to ECEF axes and expressed along the INS axis. The expression corrects the raw measured angular velocity for the total rate gyro bias, the angular random walk, and the inertial rotation of the ECEF reference frame. The unknown angular random walk component is included in this formula only for theoretical purposes. In practice, it is not known, and its *a priori* estimate of zero is used in the filter's dynamic propagation of the attitude that determines its *a priori* estimate at sample $k+1$.

The 3×3 matrix $A(\underline{q})$ defines the rotation from ECEF coordinates to INS coordinates and is computed using the attitude quaternion as follows [50]:

$$A(\underline{q}) = \begin{bmatrix} q_1^2 - q_2^2 - q_3^2 + q_4^2 & 2(q_1q_2 + q_3q_4) & 2(q_1q_3 - q_2q_4) \\ 2(q_1q_2 - q_3q_4) & -q_1^2 + q_2^2 - q_3^2 + q_4^2 & 2(q_2q_3 + q_1q_4) \\ 2(q_1q_3 + q_2q_4) & 2(q_2q_3 - q_1q_4) & -q_1^2 - q_2^2 + q_3^2 + q_4^2 \end{bmatrix} \tag{4.23}$$

where the four components of the quaternion are written as q_i for $i = 1, .., 4$. Reference [50] provides a more in-depth discussion of the quaternion model and typical attitude propagation methods that use INS measurements.

The model replacement differential equations for position and velocity are propagated using numerical integration. Measurements from the accelerometer are used in the velocity differential equation instead of a dynamics model for acceleration. After correction for measurement errors, the addition of gravity, and the inclusion of Coriolis and centrifugal effects,

the model-replacement system of position and velocity differential equations becomes [32]:

$$\begin{aligned}
\dot{\underline{r}} &= \underline{v} \\
\dot{\underline{v}} &= -2\underline{\omega}_E \times \underline{v} - \underline{\omega}_E \times (\underline{\omega}_E \times \underline{r}) \\
&\quad + A^T(\underline{q})[\underline{y}_{ACC} - (\Delta\underline{b}_{ACC} + \underline{b}_{ACC_0}) - \underline{\nu}_{ACC}] + \underline{g}(\underline{r})
\end{aligned} \tag{4.24}$$

where the uncorrected INS measurement of the acceleration vector minus gravity is denoted as $\underline{y}_{ACC}$, $\underline{\nu}_{ACC}$ is the 3×1 accelerometer velocity random walk process noise vector, and $\underline{g}$ is the ECEF gravitational acceleration vector at the current position. Like the angular random walk term in Eq. (4.21), the velocity random walk term in this system of equations is included for theoretical purposes only. In practice, it is unknown, and its *a priori* estimate of zero is used in the EKF's dynamic propagation calculations that determine the *a priori* state estimate at sample $k+1$. The simplest $1/r^2$ gravity acceleration vector model takes the form: $\underline{g}(\underline{r}) = -\mu\underline{r}/(\underline{r}^T\underline{r})^{3/2}$, where μ is defined as the central gravitational parameter of the Earth. A more accurate model that includes higher-order Earth gravity model effects can be found in [27]. One possible source for the high-order coefficients in this model is the EGM96 [26]. The filter in this work uses the gravity model from [27] with EGM96 coefficients out to degree and order seven.

Similar to the attitude dynamics model replacement equation in Eq. (4.21), this model-replacement form of the position/velocity dynamics uses a corrected form of the accelerometer output. The corrections subtract off the total bias vector and, in theory, the velocity random walk vector. After this initial set of corrections, the resulting acceleration is rotated from INS coordinates into ECEF coordinates with the help of the transpose of the $A(\underline{q})$ matrix. Finally, the resulting acceleration is added to the gravitational acceleration and corrected for the Coriolis and centrifugal effects of the rotating ECEF coordinate frame.

The need to add the gravity vector arises because of the nature of the accelerometer's measurement: It senses only the difference between the system's inertial acceleration and the acceleration of gravity.

It is assumed that the k^{th} INS measurements apply from time $t_k - \Delta t/2$ to time $t_k + \Delta t/2$, with $\Delta t = t_{k+1} - t_k$. Therefore, the interval from t_k to t_{k+1} is assumed to use two different INS measurements. This assumption causes the implementation of the SRIF calculations to include an additional complication described in [32]. The filter cannot easily use the INS biases at t_{k+1} during the propagation of the state from $\hat{x}_k$ to $\overline{x}_{k+1}$. Therefore, all the INS measurements are corrected using the k^{th} sample's INS bias estimates.

The two systems of dynamic propagation equations, Eqs. (4.21) and (4.24), use measurements from the INS. The first uses $\underline{y}_{RG}$, the 3×1 angular rate vector measured by the rate gyro, and the second uses $\underline{y}_{ACC}$, the 3-axis difference between the acceleration and gravity measured by the accelerometer. Using measurements in the dynamic propagation is non-standard in a KF, but it is often employed by navigation filters that use INS data, and in particular, by filters that fuse INS and RF measurements in a tightly-coupled manner.

The use of model replacement is similar to the direct integration of INS measurements in dead-reckoning. The dead-reckoning method integrates the measured accelerations and angular rates to determine the future position, velocity, and attitude states. In theory, a Kalman filter using model replacement could be run without measurement updates and produce results similar to a dead-reckoning-based INS. Model replacement Kalman filters are natural extensions of older navigation systems that used INS measurements for dead-reckoning.

Model replacement's use of INS measurements in the dynamic propagation step removes the need for specific dynamics models. Model replacement also obviates the need for measure-

ment models that compute the acceleration minus gravity and the rotation rate as functions of system states. This advantage can reduce the needed dimension of the filter's state vector. Another benefit of model replacement is that measurement updates only need to be performed when a new measurement is available from a source other than the INS. Any filter that uses inertial measurements in a standard measurement update will require such an update at every INS sample. The reduced number of states and measurement updates in model replacement reduces the computational cost of the filter. Model replacement comes at the cost of employing a non-standard KF implementation, needing to treat INS measurement noise as process noise, and losing a straight-forward ability to exploit any existing dynamics-model-based information about the expected vehicle motion. Model replacement seems to be the predominant method for using INS measurements in a tightly-coupled INS/RF KF. The literature, however, lacks research showing that the model replacement method is the best method for incorporating INS measurements into a tightly-coupled filter.

For a sampled-data discrete-time Kalman filter, the model replacement method requires some form of numerical integration of the coupled systems of differential equations in Eqs. (4.21) and (4.24). Various numerical schemes would be suitable for use in such a filter. This paper presumes that the attitude dynamics model in Eq. (4.21) is integrated using trapezoidal integration. This allows the integration to be performed using a sequence of two quaternion multiplications. The position/velocity dynamics model in Eq. (4.24) is integrated using implicit trapezoidal integration. It is implicit because the gravitational acceleration at the final time of the integration interval is evaluated at the final position, as determined by the integration. A simple iterative non-linear equation solver for the correct final position is used in order to solve the resulting implicit equation. For small enough sample intervals, Δt, these numerical integration schemes are adequate.

4.4.2 Gauss-Markov Models

A Gauss-Markov model can be used to dynamically propagate acceleration, velocity, and position states. Additionally, a separate Gauss-Markov model can be used to propagate angular rate and quaternion states. The following subsections discuss sensible ways to define the needed Gauss-Markov system state vectors and their dynamic propagation models. The position/velocity Gauss-Markov model can be used with the model replacement method for rotational motion in order to propagate the position, velocity, acceleration, and attitude quaternion. Alternatively, both Gauss-Markov models can be used to remove the use of model replacement entirely. The Gauss-Markov models provide substitutes for the elements of the $\underline{f}$ function in Eq. (4.1) that would otherwise be defined using model replacement and numerical integration. In addition, they provide the additional components of the $\underline{f}$ function which are required for the dynamic propagation of all additional states that get introduced by the Gauss-Markov model.

A Gauss-Markov Position/Velocity/Acceleration Dynamic Model and its Associated Accelerometer Measurement Model

The Gauss-Markov model in this section integrates a new set of acceleration state vector elements once in order to propagate the corresponding velocity states forward in time and a second time in order to propagate the corresponding position states forward in time. Suppose that the time propagation interval is $\Delta t = t_{k+1} - t_k$. Acceleration is propagated as a first-order Gauss-Markov process, driven by white noise. The discrete-time model to propagate the position, velocity, and acceleration states is defined as:

$$\begin{bmatrix} \underline{r}_{k+1} \\ \underline{v}_{k+1} \\ \underline{a}_{k+1} \end{bmatrix} = \begin{bmatrix} I & \Delta t I & \frac{1}{2}\Delta t^2 I \\ 0 & I & \Delta t I \\ 0 & 0 & e^{-\frac{\Delta t}{\tau_{ACC}}} I \end{bmatrix} \begin{bmatrix} \underline{r}_k \\ \underline{v}_k \\ \underline{a}_k \end{bmatrix} + \begin{bmatrix} 0 \\ 0 \\ I \end{bmatrix} \underline{\nu}_{ACCGMk} \tag{4.25}$$

where I is the 3×3 identity matrix, $\underline{a}_k$ is the 3×1 ECEF acceleration vector at time t_k, τ_{ACC} is the time constant of the Gauss-Markov process, and $\underline{\nu}_{ACCGMk}$ is the process noise vector, which is assumed to be Gaussian and white. The covariance of the process noise vector and τ_{ACC} are tuning parameters. The covariance of the process noise vector should vary based on the magnitude of the expected acceleration. Receivers on platforms with higher possible accelerations, like fighter aircraft, should have higher process noise covariances. The time constant τ_{ACC} is a forgetting factor. Depending on whether it is large or small, it increases or decreases the correlation of the current acceleration with the acceleration at a particular time offset into the future or past relative to the current time. Increasing τ_{ACC} to infinity results in a random walk process driven by the white process noise.

Equation (4.25) can be modified so that the acceleration process noise vector is defined in INS coordinates or in local-level East-North-Up (ENU) coordinates. The different coordinate systems enable more realistic values to be used in the process noise covariance matrix. For instance, if the receiver is on a car, the vertical acceleration should be much less than the East and North accelerations. Therefore, if the ENU coordinate frame is used, then the element of the process noise covariance matrix that corresponds to the *Up* direction's variance can be set to a smaller value than the other two components. Although such changes of coordinate systems may improve results, they are not considered in this work. They are left as a subject for future study.

The use of this position/velocity/acceleration Gauss-Markov model does not obviate the

need for a method to propagate the attitude quaternion. One form of Gauss-Markov filter considered in this work uses rate gyro measurements in a model-replacement process, as already discussed in conjunction with Eq. (4.21) in the preceding subsection. A filter might use model replacement with the rate gyro measurements in order to reduce the number of states in the filter, reduce the amount of tuning required, or obviate the need for developing a Gauss-Markov attitude dynamics model. Alternatively, using a Gauss-Markov model to propagate the angular rates enables INS measurements to be incorporated using standard KF measurement updates, but at the cost of additional state elements and more tuning. Note, however, that the tuning of such a Gauss-Markov model permits the filter to use additional information about the expected motion of the receiver without deriving a specific dynamics model for the platform on which the receiver is mounted.

The ECEF acceleration vector that appears in Eq. (4.25) needs to be appended to the filter state vector. The modified filter state vector becomes:

$$\underline{x} = \left[\underline{q};\, \underline{r};\, \underline{v};\, \underline{a};\, \Delta\underline{b}_{RG};\, \Delta\underline{b}_{ACC};\, \underline{b}_{RG_0};\, \underline{b}_{ACC_0};\, c\delta_R;\, c\dot{\delta}_R\right] \tag{4.26}$$

where $\underline{a}$ is the 3×1 ECEF acceleration vector of the receiver. The other states are the same as those defined in connection with Eq. (4.20). This state vector has 27 elements. This particular state vector assumes that the attitude dynamics model is still based on INS model replacement.

Since the accelerometer measurements are not used in the dynamic propagation step when using a Gauss-Markov model, they must be included in the measurement update step. Thus, a measurement model for acceleration is needed as part of the measurement model function

that is defined in Eq. (4.2). The accelerometer measurement model used in this work is:

$$\underline{h}_{ACC}(\underline{x}) = A(\underline{q})[\underline{a} + 2\underline{\omega}_E \times \underline{v} + \underline{\omega}_E \times (\underline{\omega}_E \times \underline{r}) - \underline{g}(\underline{r})] + \Delta\underline{b}_{ACC} + \underline{b}_{ACC_0} + \underline{w}_{ACC} \quad (4.27)$$

where $\underline{w}_{ACC} = \underline{\nu}_{ACC}$ is the same velocity random walk accelerometer measurement noise as appears in Eq. (4.24), but re-named to maintain the convention in Eqs. (4.1) and (4.2) of designating process noise components as $\underline{\nu}$ and measurement noise components as $\underline{w}$. This accelerometer measurement model is mathematically equivalent to the second line of Eq. (4.24), but the result on the right-hand side of Eq. (4.27) is given in INS coordinates instead of ECEF coordinates. The measurement model in Eq. (4.27) uses the new ECEF acceleration state element, $\underline{a}$. One of the principal reasons for adding this state is to enable this definition of a sensible measurement model for the accelerometer outputs. A model-replacement dynamic propagation of the position and velocity states would obviate the need for such a new state and the associated measurement model. The accelerometer measurements and the new model are appended to, respectively, $\underline{z}_k$ and $\underline{h}[k, \underline{x}_k]$ in Eq. (4.2).

The use of the acceleration vector in a measurement update requires that a measurement update be performed at every INS time step, which may result in more measurement updates than the model replacement method would require. Additional measurement updates require increased computations. Extra computations and state vector elements make the Gauss-Markov model a less attractive method than the model replacement method in cases where system memory or computation speed is limited.

Angular Rate

A Gauss-Markov process for angular rate can be used to dynamically propagate the attitude quaternion state. With the angular rates defined by the Gauss-Markov process, the attitude

quaternion can be propagated similarly to the model replacement method. Instead of using the rate gyro measurements in Eq. (4.21), the angular rate states are used. The Gauss-Markov model for the angular rate vector is similar to the last line of Eq. (4.25). White noise drives the angular rate propagation in the Gauss-Markov process. The discrete-time Gauss-Markov process to propagate the angular rate state to a future time is defined as:

$$\underline{\omega}_{k+1} = e^{\frac{-\Delta t}{\tau_{AR}}} \underline{\omega}_k + \underline{\nu}_{ARGMk} \tag{4.28}$$

where $\underline{\omega}_k$ is the 3×1 angular rate vector of the receiver at time t_k relative to inertial coordinates but measured along INS axes, τ_{AR} is the time constant of this first-order Gauss-Markov process, and ν_{ARGMk} is the Gaussian, white process noise vector. Similar to Eq. (4.25), the term τ_{AR} and the covariance matrix of $\underline{\nu}_{ARGMk}$ are tuning parameters for the angular rate Gauss-Markov model. Increasing the value of τ_{AR} to infinity results in a random walk process.

The attitude quaternion is propagated under the assumptions that a constant angular rate applies from t_k to $t_k + \Delta t/2$, $\underline{\omega}_k$, and that a different constant angular rate applies from $t_k + \Delta t/2$ to t_{k+1}, $\underline{\omega}_{k+1}$. A quaternion is computed for each rotation that applies over each interval of duration of $\Delta t/2$. Additionally, the inverse of the quaternion due to the Earth's rotation over the entire time interval Δt is needed. Quaternion multiplication of the three quaternions computed from the angular rates propagates $\underline{q}_k$ to $\underline{q}_{k+1}$:

$$\underline{q}_{k+1} = [(\underline{q}_{\underline{\omega}_{k+1}} \otimes \underline{q}_{\underline{\omega}_k}) \otimes \underline{q}_k] \otimes \underline{q}_{\underline{\omega}_E}^{-1} \tag{4.29}$$

where $\otimes$ denotes quaternion multiplication, $\underline{q}_{\underline{\omega}_{k+1}}$ is the quaternion that parameterizes the

rotation during the second half of the interval:

$$\underline{q}_{\underline{\omega}_{k+1}} = \begin{bmatrix} \frac{1}{4}\Delta t \underline{\omega}_{k+1} sinc(\frac{1}{4}\Delta t||\underline{\omega}_{k+1}||) \\ cos(\frac{1}{4}\Delta t||\underline{\omega}_{k+1}||) \end{bmatrix} \tag{4.30}$$

where $||\ \ ||$ is the 2-norm function and the *sinc* function is defined as follows:

$$sinc(x) = \begin{cases} \frac{sin(x)}{x} & x \neq 0 \\ 1 & x = 0 \end{cases} \tag{4.31}$$

$\underline{q}_{\underline{\omega}_k}$ is the quaternion that parameterizes the rotation during the first half of the interval:

$$\underline{q}_{\underline{\omega}_k} = \begin{bmatrix} \frac{1}{4}\Delta t \underline{\omega}_k sinc(\frac{1}{4}\Delta t||\underline{\omega}_k||) \\ cos(\frac{1}{4}\Delta t||\underline{\omega}_k||) \end{bmatrix} \tag{4.32}$$

and $\underline{q}_{\underline{\omega}_E}$ is the quaternion that parameterizes the Earth's rotation over the entire interval from t_k to t_{k+1}:

$$\underline{q}_{\underline{\omega}_E} = \begin{bmatrix} 0 \\ 0 \\ sin(\frac{1}{2}\Delta t||\underline{\omega}_E||) \\ cos(\frac{1}{2}\Delta t||\underline{\omega}_E||) \end{bmatrix} \tag{4.33}$$

Its inverse is:

$$\underline{q}_{\underline{\omega}_E}^{-1} = \begin{bmatrix} 0 \\ 0 \\ -sin(\frac{1}{2}\Delta t||\underline{\omega}_E||) \\ cos(\frac{1}{2}\Delta t||\underline{\omega}_E||) \end{bmatrix} \tag{4.34}$$

Quaternion multiplication can be defined by the following matrix-vector equation [50]:

$$\underline{q}_{BA} = \underline{q}_B \otimes \underline{q}_A = \begin{bmatrix} q_{B4} & q_{B3} & -q_{B2} & q_{B1} \\ -q_{B3} & q_{B4} & q_{B1} & q_{B2} \\ q_{B2} & -q_{B1} & q_{B4} & q_{B3} \\ -q_{B1} & -q_{B2} & -q_{B3} & q_{B4} \end{bmatrix} \underline{q}_A \tag{4.35}$$

where q_{Bi} for $i = 1, ..., 4$ are the four individual elements of the quaternion $\underline{q}_B$.

When the Gauss-Markov model propagates the angular rates, the acceleration measurements can be used in either a model replacement method or a Gauss-Markov model method to propagate position and velocity. Thus, acceleration does not necessarily need to be included in the state vector. The angular rate vector, however, needs to be included in the state vector because it is used in Eq. (4.28), it is used to define terms in Eq. (4.29), and it is used in the rate gyro measurement model, which is defined below. The updated Kalman filter state vector is defined as:

$$\underline{x} = \left[\underline{q};\ \underline{\omega};\ \underline{r};\ \underline{v};\ \Delta\underline{b}_{RG};\ \Delta\underline{b}_{ACC};\ \underline{b}_{RG_0};\ \underline{b}_{ACC_0};\ c\delta_R;\ c\dot{\delta}_R\right] \tag{4.36}$$

if a Gauss-Markov model is used for the attitude dynamics while model replacement is used for the position/velocity dynamic propagation. This state vector has 27 elements. If Gauss-

Markov models are used for both the attitude dynamics and the position/velocity dynamics, then the updated Kalman filter state vector becomes:

$$\underline{x} = \left[\underline{q};\ \underline{\omega};\ \underline{r};\ \underline{v};\ \underline{a};\ \Delta\underline{b}_{RG};\ \Delta\underline{b}_{ACC};\ \underline{b}_{RG_0};\ \underline{b}_{ACC_0};\ c\delta_R;\ c\dot{\delta}_R\right] \tag{4.37}$$

This state vector has 30 elements.

When working with this Gauss-Markov attitude rate model, the actual rate gyro measurements can affect the filter's state estimate only through the measurement update step. Thus, a measurement model for the angular rate vector is needed. The measurement model used for the rate gyro outputs is:

$$\underline{h}_{\omega}(\underline{x}) = \underline{\omega} + \Delta\underline{b}_{RG} + \underline{b}_{RG_0} + \underline{w}_{RG} \tag{4.38}$$

where $\underline{w}_{RG}$=$\underline{\nu}_{RG}$ is the same angular random walk rate gyro measurement noise as appears in Eq. (4.21), but re-named to maintain the convention in Eqs. (4.1) and (4.2) of designating process noise components as $\underline{\nu}$ and measurement noise components as $\underline{w}$. This rate gyro measurement model is mathematically consistent with the argument of the Ω matrix factor in Eq. (4.21). This model adds errors to construct the measurement from the true rotation rate, whereas Eq. (4.21) subtracts errors from the measurement to construct the truth. This model does not include an Earth rotation rate term because that effect has been incorporated into the dynamic propagation of Eq. (4.29) and, therefore, does not belong here. The rate gyro measurements and the new model are appended to, respectively, $\underline{z}_k$ and $\underline{h}[k, \underline{x}_k]$ in Eq. (4.2).

Discussion of Benefits of Gauss-Markov Models

One of the benefits of the Gauss-Markov model method is the ability to include information about the expected receiver motion. By tuning the process noise covariance matrices for $\underline{\nu}_{ACCGMk}$ and $\underline{\nu}_{ARGMk}$, the filter incorporates information about the receiver's expected motion while keeping the dynamics models general.

The covariance matrix of the $\underline{\nu}_{ARGMk}$ process noise vector in Eq. (4.28) can be modified based on the expected roll, pitch, and yaw rate magnitudes of the vehicle. Similarly, the covariance matrix of the $\underline{\nu}_{ACCGMk}$ process noise vector in Eq. (4.25) can be modified based on the expected acceleration capability of the platform on which the receiver is mounted. Such tunings can result in better performance. Improper tuning can make performance worse. Additionally, the more precise the tuning, the less generalized the dynamics model becomes. A filter perfectly tuned for a car might not perform well for a receiver on an airplane.

Another potential benefit of the Gauss-Markov model method is the ease of including more than one accelerometer or rate gyro measurement. The additional measurements can be included in the measurement update step. Note that new accelerometer and rate gyro bias states would need to be appended to the state vector in order to account for such errors in the new INS measurements. Multiple instances of the measurement models in Eqs. (4.27) and (4.38) would need to be used in the measurement update, one for each new accelerometer and rate gyro measurement. The measurement models might also need to be slightly adjusted to account for different positions and orientations of the additional accelerometer or rate gyro.

It is less clear how one would include multiple redundant INS measurements in the model replacement method. One possible strategy for incorporating multiple redundant INS measurements is to create average synthetic INS measurements, one that averages all of the

accelerometer measurements and another that averages all of the rate gyro measurements. The averaging of the measurements results in averaged bias vectors. Thus, the true INS biases for each accelerometer and rate gyro would not be observable from the averaged measurements. It might be possible, however, to design a good navigation filter that only included accelerometer and rate gyro bias averages in its Kalman filter state vector rather than the individual biases of each device. A similar averaging strategy could be employed by a navigation filter that used Gauss-Markov dynamics rather than model-replacement dynamics. Although the combination of measurements from multiple INSs is not a focus of this work, some preliminary results using multiple redundant INS sensors are presented in Section 4.7.3.

4.5 Filter and Truth-model Simulation

The Kalman filters that are evaluated in this work are SRIF-forms of first-order EKFs. The details of the dynamics models, measurement models, and filter implementation for the model-replacement Kalman filter are described in [32]. The present work's Gauss-Markov filters make changes to the filter from [32] to account for the different methods of including inertial measurements described in Section 4.4. The dynamic propagation of all states not described in Section 4.4 follows the equations from [32]. While the details of the dynamic propagation and the measurement update vary, the core equations of the SRIF from [32] remain unchanged.

Satellite-based radio navigation data are simulated and used in each proposed filter. The measurement observables are carrier Doppler shifts simulated using Eq. (23) from [32]. Each filter's absolute navigation capability is based on the position information that is contained in accurate carrier Doppler shift measurements. The random noise added to the simulated

carrier Doppler shift measurements has a 0.01 m/s range-rate-equivalent standard deviation. The satellite constellation parameters and visibility are defined in detail in [32]. No more than three carrier Doppler shifts are ever simultaneously available in any simulation. This low number of simultaneous measurements implies that the point-solution batch filter proposed in [42] cannot be used because it requires eight or more simultaneous carrier Doppler shift measurements. The low number of simultaneous carrier Doppler shift measurements requires the system in this work to rely heavily on its INS-provided dynamic propagation capability in order to achieve full 3-axis observability and, therefore, a reasonable ability to do full 3-axis navigation. Therefore, this problem provides a challenging environment in which INS data must be used wisely.

This work uses two different truth-model simulations. The first is the same as in [32], in which a simulated receiver is flying on an aircraft over Blacksburg, Virginia in a double figure-eight pattern with a length of 6 km and width of 6 km, where the plane traverses the same figure-eight path twice. The nominal velocity of the airplane in the simulation is 59 m/s. The second simulation is of a tricycle slowly moving in a four-quadrant pattern in Blacksburg, Virginia. The nominal velocity of the tricycle simulation is 2.1 m/s. The true position time history of the tricycle can be seen in Fig. 4.1.

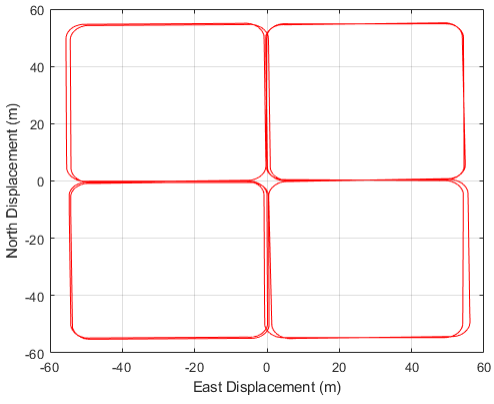

Figure 4.1: The four-quadrant pattern of the true tricycle position time history.

The duration of both simulations is around 16.67 minutes. The sampling frequency is 100 Hz for the INS and the radio-navigation observables. Each simulation uses a 5-degree elevation mask for the receiver antenna in its antenna-fixed coordinate system. The aircraft model rolls and pitches in order to execute coordinated turns at a constant altitude, which can affect satellite availability due to the corresponding rolling and pitching of the elevation mask window. The tricycle model does not roll or pitch. One difference between the simulations is that the tricycle moves slower than the airplane resulting in a lower diversity of the rate of change of the line-of-sight vectors between the satellite and the receiver. A reduction in this diversity has been shown to increase navigation error in [32, 42, 22]. The fast relative velocity of the LEO satellites may make the difference in receiver velocities negligible.

The truth-model simulation bases its generation of INS measurements on a cubic spline of the true positions of the receiver. The second derivatives of this spline give the receiver accelerations relative to ECEF coordinates. These, in turn, can be combined with Coriolis and centrifugal acceleration to give inertial acceleration. Afterward, gravity is subtracted from the result, and that result is transformed into INS coordinates and corrupted by biases and velocity random walk. Attitude time histories are generated for the aircraft or the tricycle that are consistent with the coordinated flight for the aircraft or the kinematics and steering of the tricycle in order to generate a sensible attitude time history for the vehicle. A smoothed derivative of this attitude time history is used to compute the rotation rate relative to ECEF coordinates. The Earth rotation rate is added to this rate, the result is transformed into INS coordinates, and biases and angular random walk are added in order to simulate the rate gyro measurements.

All states from Eqs. (4.20), (4.26), (4.36), and (4.37) are simulated. Depending on which type of Kalman filter is being tested, the appropriate subset that constitutes the defined filter state vector of Eqs. (4.20), (4.26), (4.36), or (4.37) is grouped into that definition in

order to yield the "truth" state time history. The simulated vector time histories of position, velocity, and acceleration, $\underline{r}(t)$, $\underline{v}(t)$, and $\underline{a}(t)$, have been generated using a cubic spline of the aircraft or tricycle position time history and its first and second time derivatives. The simulated attitude time history $\underline{q}(t)$ has been generated based on the $\underline{r}(t)$, $\underline{v}(t)$, and $\underline{a}(t)$ time histories and the needed attitude for a coordinated turn in the aircraft or for zero-side-slip kinematics in the tricycle. The simulated attitude rate time history $\underline{\omega}(t)$ has been generated by differentiating spline-smoothed version of $\underline{q}(t)$ modifying it to include the effects of Earth rotation. The INS bias states and the clock drift states are simulated using their respective Gauss-Markov models, which are given in Eqs. (10), (11), (12), (13), and (5) of [32]. Even when the simulated acceleration time history $\underline{a}(t)$ or the simulated rotation rate time history $\underline{\omega}(t)$ is not needed as part of the filter state vector, it will be used in order to generate the simulated INS measurements, either in Eq. (4.27) or in Eq. (4.38).

Keplerian elements are used to simulate the orbits of the satellites that provide radio-navigation signals. The Iridium and Starlink constellations described in [32] are simulated and produce carrier Doppler shift measurements. The carrier Doppler shift measurement model used in the filter and to simulate measurements is defined in Eq. (23) of [32].

Between the Iridium and Starlink constellations, there are thousands of satellites in LEO and tens of satellites visible from anywhere on the ground. With simultaneous signals from eight or more satellites, a point solution using carrier Doppler shift can be calculated which obviates the need for a tightly-coupled INS/carrier Doppler shift Kalman filter [42]. The Iridium and Starlink constellations, however, have been designed for communication. Thus, only a single satellite needs to service any area on the Earth. Each constellation's antenna beam patterns and beam steering laws preclude the simultaneous availability of eight or more signals at any given location because the constellation designers seek to minimize power usage and beam coverage overlap. Instead of using omnidirectional beacons to broadcast

signals, each satellite of a communication constellations transmits multiple narrow beams, each of which services a given area on the Earth. These beams are analogous to the cells of terrestrial cell-phone service. Starlink uses steerable spot beams. Iridium uses a pattern of (slightly) overlapping beams that provide a fixed pattern of coverage relative to the spacecraft. This effort has found information about the satellite constellations and beam properties in FCC documents. Not all information on spot beams is given in the documents. Therefore, assumptions are made about the availability of signals.

The beam properties found in [34] characterize the visibility of the Iridium constellation. Generally, only one satellite from the Iridium constellation has a strong enough signal to yield carrier Doppler shift measurements at any given time, but there are occasions where the beam patterns of multiple Iridium satellites overlap, resulting in the availability of multiple carrier Doppler shift measurements at a given location. Starlink FCC filing documents define the visibility of the Starlink constellation [13]. It is assumed that only one Starlink satellite will service a single location at any time. Thus, the Starlink constellation only provides a single carrier Doppler shift measurement at any given time. This work's simulation randomly selects the satellite that produces the simulated carrier Doppler shift measurement from the set of all visible Starlink satellites. Because of these simulated Iridium and Starlink beam coverage characteristics, the simulated receiver receives a minimum of zero satellites' carrier Doppler shift measurements and a maximum of three from the Iridium and Starlink constellations combined.

Noise is added to the true measurements during the truth-model simulation. The INS measurement noise values are defined using the manufacturer's specifications. The Honeywell HG4930 is the INS that is modeled in this work, and its properties are defined in [19]. It is a high-performance Micro-Electro-Mechanical-System-grade (MEMS-grade) INS. The range-rate equivalent carrier Doppler shift measurement error standard deviation is simulated as

being 0.01 m/s.

All Gauss-Markov-based filters in this work use a value of 7200 for both τ_{ACC} and τ_{AR}. Since the value of 7200 seconds is near that of the total length of the simulation, the Gauss-Markov models are effectively random-walk models over the duration of the tests. The Gauss-Markov models require tuning of the process noise covariance matrices. For Gauss-Markov filters that are applied to the airplane, the nominal acceleration process noise covariance is set to $(1\ m/s^2)^2$ for each diagonal element of the matrix. The Gauss-Markov-based filters for the tricycle reduced this nominal value by a factor of 25. The nominal angular rate process noise covariance for the Gauss-Markov-based filters is set to $(10^{-3}\ rad/s)^2$ for each diagonal element of the matrix. The sample interval associated with the equations using the process noise covariance, Eqs. (4.25) and (4.28), is 0.01 seconds. Different values than these nominal values were tested, and increasing or decreasing either process noise covariance by orders of magnitude resulted in navigation errors increasing by a factor of three or more. Changes to the nominal values of less than an order of magnitude resulted in negligible changes to the navigation errors.

The minimum root Allan variance and the time delay of the minimum define the receiver clock stability. The simulation uses a minimum root Allan variance of 10^{-10} seconds per second. Its time delay is set to 10 seconds. These numbers correspond to the performance of a very good crystal oscillator.

Table 4.1 presents the nominal values of important simulation and filter tuning parameters. The values include measurement and process noise nominal standard deviation values. The carrier Doppler shift measurement noise standard deviation is based on rough estimates of the carrier-to-noise density ratio, accumulation intervals, and wavelength for the Iridium and Starlink constellation signals. The random walk and bias drift parameter nominal values are based on the properties of the HG4930 and its manufacturer's design specifications and the

nominal time step. The rate gyro and accelerometer bias drift terms are defined by the manufacturer's specifications of the HG4930, the nominal time step of the simulation, and time constant parameters of the Markov models defined in Eqs. (10) and (11) of [32]. The clock offset and offset rate process noise nominal values are based on the minimum root Allan variance and the time delay of the minimum in addition to the nominal time step of the simulation. All of the simulations in this work use a nominal time step of 0.01 seconds.

The bottom four terms in Table 4.1 are the nominal standard deviations of the white process noise used to simulate and tune the dynamic models of $\Delta\underline{b}_{RG}$, $\Delta\underline{b}_{ACC}$, $c\delta_R$, and $c\dot{\delta}_R$, respectively. These models are defined in Eqs. (10), (11), and (5) of [32]. Each of these equations contains one white process noise term, $\underline{\nu}$, except for Eq. (5) of [32] which contains the clock offset and clock offset rate white process noise terms. The corresponding values in Table 4.1 are the nominal standard deviations used for these white noise terms in the truth-model simulations for $\Delta\underline{b}_{RG}$, $\Delta\underline{b}_{ACC}$, $c\delta_R$, and $c\dot{\delta}_R$. The diagonal elements corresponding to the $\Delta\underline{b}_{RG}$, $\Delta\underline{b}_{ACC}$, $c\delta_R$, and $c\dot{\delta}_R$ states of the tuned process noise covariance matrix Q_k, defined in Eq. (4.4), are also based on the last four terms of Table 4.1.

Table 4.1: Nominal values of noise standard deviations of relevant simulation and filter tuning parameters

Simulation Parameters	Nominal Values
Doppler Shift Measurement Noise	0.01 m/s
Angular Random Walk	1.1636e-05 $rad/s^{0.5}$
Velocity Random Walk	5e-04 $m/s^{1.5}$
RG Bias Drift	2.0201e-9 rad/s
Acc. Bias Drift	4.0875e-7 m/s^2
Clock Offset Process Noise	0.0095 m
Clock Offset Rate Process Noise	8.2102e-04 m/s

Two simplifying assumptions are made in this work. One assumption is that there is no

mismatch between the satellite ephemeris of the truth-model and the filter. An error in the receiver clock offset estimate, however, can result in errors in a Kalman filter's computed satellite position and velocity. The receiver lacks a perfect clock. Therefore, errors in the clock result in the filter using the wrong time to calculate the satellite's position and velocity from the perfect ephemeris. Another assumption is that the simulation and filter have identical ionosphere and neutral atmosphere delay models. A mismatch between the filter's model and the truth ionosphere and neutral atmosphere models can increase navigation errors. Both assumptions tend to decrease the absolute position error achieved by each filter compared to what the filter would achieve using real data. Therefore, all error results are optimistic compared to expected real-world results. For this work, comparing different Kalman filter implementations is more important than the absolute position error. Thus, these assumptions should not impact the results of this work significantly.

4.6 Representative Results

The methods described in Section 4.4 have been tested and compared using data from the truth-model simulations. The plots of this section compare a representative case that uses the fast-moving airplane simulation with an HG4930 MEMS-grade INS. The first three plots use larger initial position and attitude errors than all other cases. The larger initial errors allow for the comparison of the convergence properties of each method of incorporating the INS measurements into the Kalman filter. The first three plots of this section also compare the position, attitude, and velocity error magnitudes after the initial transients have settled. In this work error is defined as the difference between the Kalman filter's output and the "truth" values computed in the truth-model simulation.

Figure 4.2 shows the position error magnitude time history of four different methods to

incorporate INS data into a Kalman filter. The model replacement method is plotted in blue with triangle markers. The red line with square markers is the method that uses the model replacement method for the rate gyro measurements and a Gauss-Markov model for the accelerations. The green line with circle markers is the position error magnitude time history of the Kalman filter that uses the model replacement method for acceleration measurements and a Gauss-Markov model for angular rates. The purple line with "+" markers is the position error magnitude time history of the method that uses Gauss-Markov models for both the angular rates and accelerations. All of the lines in Fig. 4.2 use the same simulated data and initial conditions.

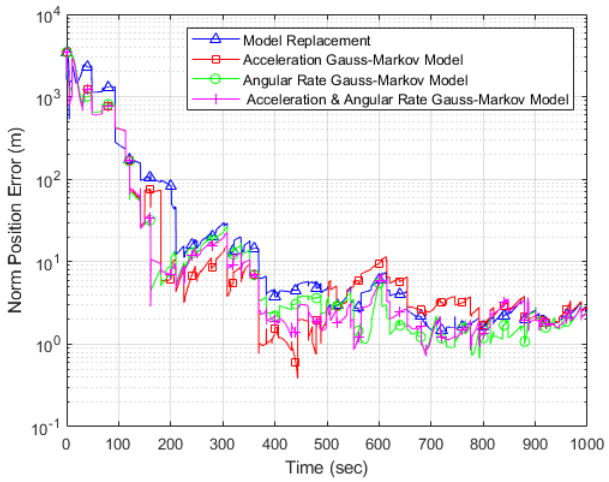

Figure 4.2: Position error magnitude time histories of a representative case using the airplane simulation with an HG4930 INS. The four filters' position error magnitude time histories are plotted on a logarithmic vertical axis.

Figure 4.2 shows that the different methods of incorporating INS data into a Kalman filter converge at about the same rate. All the position error magnitude time histories also converge to roughly the same quasi-steady-state values. There are only small differences between the position error magnitudes of the four the methods. These results indicate that the different methods perform similarly in terms of filter convergence speed and steady-state accuracy.

Figure 4.3 applies to the same simulation data and the same four filters as does Fig. 4.2. Instead of position error magnitudes, the attitude error magnitudes are plotted in Fig. 4.3. The line colors and marker types denoting each of the different Kalman filters are the same as in Fig. 4.2.

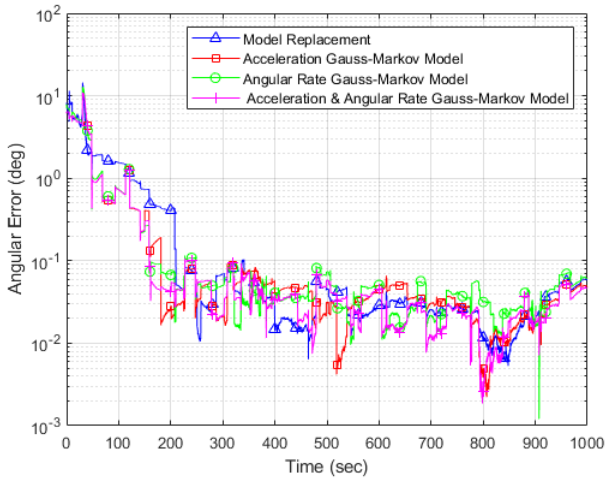

Figure 4.3: Angular error magnitude time histories of a representative case using the airplane simulation with an HG4930 INS. The four filters' angular error magnitude time histories are plotted on a logarithmic vertical axis.

The attitude error magnitude time histories for each of the four Kalman filters are similar in Fig. 4.3. The convergence rates are similar, except that the model replacement method exhibits slightly slower initial convergence. The Gauss-Markov model methods, which allow for additional tuning based on the expected motion of the receiver, may have exploited this additional information in order to achieve their slightly faster convergence rates in Fig. 4.3. All four Kalman filters converge to similar quasi-steady levels of angular error. Therefore, from an attitude error standpoint, all four filters exhibit similar performance.

Figure 4.4 applies to the same simulation data and the same four filters as Figs. 4.2 and 4.3. It plots the velocity error magnitude time histories that correspond to the four different methods of incorporating INS data into the Kalman filter. The initial velocity errors are

the same for all four filters. The line colors and marker types in Fig. 4.4 denote the same methods to incorporate INS data into the Kalman filter as in Figs. 4.2 and 4.3.

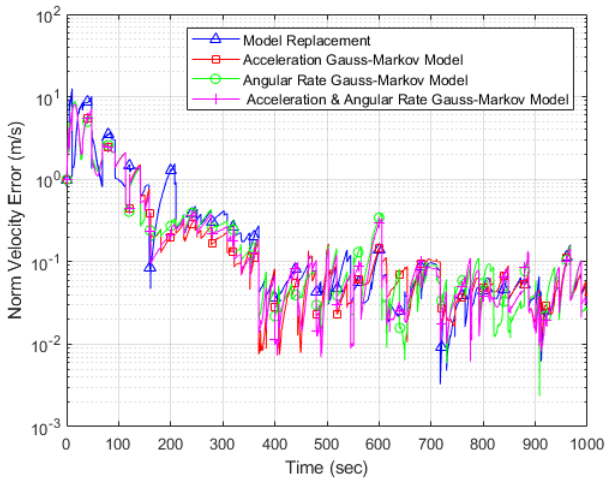

Figure 4.4: Velocity error magnitude time histories of a representative case using the airplane simulation with an HG4930 INS. The four filters' velocity error magnitude time histories are plotted on a logarithmic vertical axis.

The filter convergence properties depicted in Fig. 4.4 are similar for each of the four Kalman filters. The model replacement method exhibits somewhat larger initial gyrations. Perhaps the three Kalman filters that use Gauss-Markov models avoid this by exploiting their information about the expected receiver motion. Even with their slightly different convergence properties, all of the methods have similar quasi-steady-state velocity error magnitudes after the initial transients die out.

Figures 4.2, 4.3, and 4.4 indicate that all four methods of incorporating INS data into a Kalman filter in this work have similar convergence properties and position, attitude, and velocity quasi-steady-state error magnitudes. These results are only a single run of a representative case and have been included in order to show and compare how each method behaves. Section 4.7 runs more cases in a Monte Carlo simulation to form a better idea of the navigation errors of each method. The different architectures produce similar levels of

position, attitude, and velocity magnitude errors in the above plots. No evidence is shown that indicates model replacement produces lower errors than the methods involving well-tuned Gauss-Markov models.

Figure 4.5 shows the position, attitude, velocity, and acceleration error magnitudes of the Kalman filter's estimates based on the data generated by one truth-model simulation using the fast-moving airplane case. The Kalman filter in Fig. 4.5 uses Gauss-Markov models for both the angular rates and accelerations. The blue lines in Fig. 4.5 show the error magnitudes between the filter results and simulated truth data. The black lines indicate the $1-\sigma$ standard deviations found by taking the square root of the trace of the filter's corresponding 3×3 estimation error covariance matrix. The initial errors, in this case, are lower than in Figs. 4.2 and 4.3. The lower initial errors are used for all future cases. The results in Fig. 4.5 show a case with poorly tuned Gauss-Markov models. The quasi-steady-state position error magnitudes are a factor of about three larger than Fig. 4.2 even though the initial errors are an order of magnitude lower.

The results in Fig. 4.5 have larger errors than other cases. These errors are caused only by poorly tuned Gauss-Markov models. In Fig. 4.5, the fourth plot's disagreement between the error and its standard deviation – the former remains significantly larger than the latter after settling – is an indicator that the acceleration Gauss-Markov model is poorly tuned. The standard deviations do not follow the dynamic variations of the errors in the bottom plot, indicating that there is a mismatch between the simulation and the filter models.

The tuning of the Gauss-Markov models is an iterative process that is more of an art than a science. The initial choices for the values of the process noise parameters for the acceleration and angular rate Gauss-Markov models were made based on a rough guess of the expected accelerations and angular rates for the fast-moving or slow-moving case. The filter results with these values were stored, and the filter was then run multiple times with the parameters

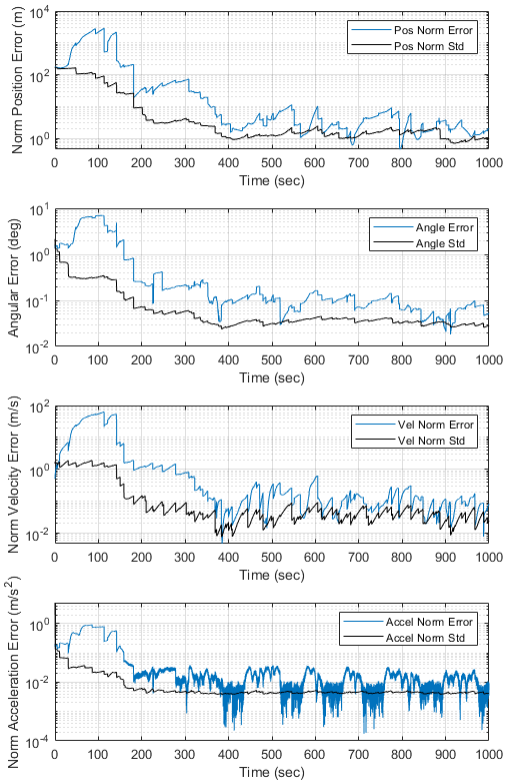

Figure 4.5: Error time histories of a representative case using a Gauss-Markov process to model the angular rate and acceleration vector. Top panel: position error magnitude; Second panel: attitude error magnitude; Third panel: velocity error magnitude; Fourth panel: angular rate error magnitude. This case uses the airplane model, but has poor tuning.

increased or decreased by an order of magnitude. The navigation error results were then compared. Filters with lower errors were considered better tuned. The plots of the error time histories and the corresponding estimation error standard deviations were also used to help decide which tuning values performed better. If the standard deviations were always smaller than the errors, the filter was overconfident and the process noise was increased. Once an order of magnitude estimate for the process noise parameters was determined, smaller variations were tested. The same metrics were compared until the navigation errors were low and the filter's computed covariance and errors were in agreement. It was found

that differences of less than an order of magnitude in the Gauss-Markov model process noise covariance had a negligible impact on the navigation error for the different cases run in this work.

4.7 Comprehensive Comparison of Gauss-Markov Filters' Performance with that of Model-Replacement Filter

This section compares the results from using different methods to incorporate INS data into a tightly-coupled INS/RF navigation filter. Data from three simulations are used to compare the methods. One is for a relatively fast-moving airplane. Another is for a relatively slow-moving tricycle. These two simulations are chosen to investigate whether the vehicle velocity impacts the navigation accuracy of the method. The final simulation includes simultaneous measurements from multiple INSs using the airplane simulation. It compares the accuracy when redundant INS measurements are available to the filter. One of the key benefits of the Gauss-Markov method is the ease of inclusion of additional INS measurements. The third simulation investigates whether this benefit is significant.

The comparison results are shown in tables of RMS errors between the truth-model simulation and the filters' converged estimates of the corresponding state components. The values shown are averaged over 20 Monte Carlo simulations for each case. Although 20 Monte Carlo simulations are not enough to fully understand the error statistics, the use of 20 simulations rather than one ensures that an outlier case does not form the basis of any comparison.

4.7.1 Fast-Moving Aircraft Case

Table 4.2 shows RMS results from 20 runs of the data simulated from a receiver on an airplane flying over Blacksburg, Virginia. Each row contains steady-state errors for the position, attitude, and velocity states for a different method of incorporating INS measurements. Each value is the RMS magnitude of the steady-state error vector for the corresponding subset of the filter states. The filter is time-varying. As such, it does not have a true steady-state as in a time-invariant filter. The term "steady-state", as used here, indicates the time after the obvious initial convergence that is depicted in Figs. 4.2, 4.3, and 4.4. Each value is averaged over 20 cases that follow the same nominal aircraft trajectory, but that have different randomized noise and initial state estimation errors. The first row contains results using the model replacement method for accelerometer and rate gyro measurements. The second-row results are found using the model replacement method for the rate gyro measurements and the Gauss-Markov model for accelerations. The filter uses the model replacement method for the accelerometer measurements and the Gauss-Markov model for angular rates to determine the third-row results. In the fourth-row results, the filter uses Gauss-Markov models for the accelerations and the angular rates.

The most accurate position results are found using the angular rate Gauss-Markov model and model replacement for the accelerometer measurements – see line 3 of Table 4.2. The filter that achieved the least accurate position results is the one that used the model replacement method for the accelerometer and rate gyro measurements – see the first line of Table 4.2. While there are differences in the results for the four filter types, none are substantially worse than any of the others. This statement holds true for all three types of accuracies that are documented in Table 4.2, i.e., for the position, attitude, and velocity accuracies. The results from Table 4.2 indicate that a Kalman filter can use a Gauss-Markov model and process the INS measurements in a traditional KF measurement update and achieve

Table 4.2: Root mean square (RMS) of steady-state position, angular, and velocity error magnitudes of the navigation Kalman filters averaged over 20 cases as functions of the filter method for incorporating INS measurements when using the Starlink and Iridium constellations, the case of a receiver on a plane with a single INS.

Kalman Filter Type	Steady-State RMS Pos. Error Mag. (m)	Steady-State RMS Angular Error Mag. (°)	Steady-State RMS Vel. Error Mag. (m/s)
Model Replacement	3.3850	0.0277	0.0811
Acceleration Gauss-Markov Model	3.3148	0.0353	0.0834
Angular Rate Gauss-Markov Model	3.2325	0.0371	0.0724
Acceleration & Angular Rate Gauss-Markov Model	3.3722	0.0382	0.0789

comparable or better performance than the model replacement method for the case with the radio-navigation receiver and the INS on a fast-moving airplane.

4.7.2 Slow-Moving Tricycle Case

Summary performance results for the case with a slow-moving wheeled vehicle are shown in Table 4.3. The simulated data in these cases are from a tricycle slowly driving around Blacksburg, Virginia. The tricycle follows the path shown in Fig. 4.1. The different rows of the table denote the same four filter design approaches as in Table 4.2. Also similar to Table 4.2, the results for the steady-state RMS position, attitude, and velocity error magnitudes averaged over 20 cases are listed in Table 4.3.

The magnitudes of the results from each of the filter design methods are similar. In this case, the model replacement filter's RMS steady-state position error is the lowest. The model replacement filter's better performance relative to the other methods could result from imperfect tuning of the other method's Gauss-Markov models. Alternatively, the direct integration of the INS measurements performed in the model replacement method may be

Table 4.3: RMS of steady-state position, angular, and velocity error magnitudes of the navigation Kalman filters as functions of the filter method for incorporating INS data when using the Starlink and Iridium constellations, the case of a receiver on a tricycle with a single INS.

Kalman Filter Type	Steady-State RMS Pos. Error Mag. (m)	Steady-State RMS Angular Error Mag. (°)	Steady-State RMS Vel. Error Mag. (m/s)
Model Replacement	1.3284	0.3899	0.0294
Acceleration Gauss-Markov Model	1.8579	0.5226	0.0458
Angular Rate Gauss-Markov Model	1.6880	0.3193	0.0466
Acceleration & Angular Rate Gauss-Markov Model	1.6430	0.3535	0.0405

more accurate for slower-moving vehicles. The relative differences in these results between the four filter designs are not very large. This fact suggests that, with proper tuning, any of the methods described in this work can be used to implement a tightly-coupled RF/INS navigation filter.

The RMS position errors and the RMS velocity errors are lower in this tricycle case compared to the aircraft case – compare the first and third results columns of Tables 4.2 and 4.3. It is conjectured that the lower overall speed of the tricycle may contribute to this improved position and velocity accuracy. Conversely, the RMS angular errors for the tricycle in the middle results column of Table 4.3 are worse than those of the aircraft, which appear in the middle results column of Table 4.2. The increased angular errors are primarily along the yaw axis. It is conjectured that the lowered lateral accelerations during the tricycle's turning maneuvers versus those of the aircraft are the cause of its degraded yaw accuracy. Yaw observability of a tightly-coupled INS/RF system requires that the horizontal component of the accelerometer's output be non-zero from time to time.

4.7.3 Multiple INS Simulation

Navigation Kalman filter results presented in this subsection are from a simulation with two sets of INS measurements at every INS sample time. The simulation is for the same fast-moving aircraft whose single-INS results have been presented in Subsection 4.7.1. The physical alignment of the two INSs is assumed to be known perfectly. The distance between the two INSs is assumed to be negligible. In the model replacement case, the two INS measurements are averaged. Averaging the INS measurements is expected to reduce the noise by a factor of $1/\sqrt{N}$, where N is the number of sets of INS measurements. In the Gauss-Markov model methods, the additional INS measurements are included in the measurement update. The filter state is extended to include two sets of independent biases for each INS data stream that employs a Gauss-Markov model rather than model replacement.

Table 4.4 shows additional results for the different Kalman filter methods of processing INS data when two INS measurements are provided at every time step. Similar to Tables 4.2 and 4.3, the results columns correspond, respectively, to the steady-state RMS position, angular, and velocity error magnitudes averaged over 20 cases. Error is computed between each filter's estimate and the truth-model simulation's truth state.

Table 4.4: RMS steady-state position, angular, and velocity error magnitudes of the navigation Kalman filters as functions of the filter method for incorporating INS data when using the Starlink and Iridium constellations for a receiver on a plane with two INSs.

Kalman Filter Type	Steady-State RMS Pos. Error Mag. (m)	Steady-State RMS Angular Error Mag. (°)	Steady-State RMS Vel. Error Mag. (m/s)
Model Replacement	2.8830	0.0288	0.0444
Acceleration Gauss-Markov Model	3.0982	0.0396	0.0566
Angular Rate Gauss-Markov Model	3.1620	0.0300	0.0591
Acceleration & Angular Rate Gauss-Markov Model	2.9813	0.0383	0.0528

The RMS errors in Table 4.4 are lower than those in Table 4.2, except for the angular error on the first, second, and fourth results row, which are very slightly larger. Smaller errors are expected when using additional INS measurements. The multi-INS position and velocity accuracy results when using the model replacement method improved more than the other methods. It is unclear why the improvements from incorporating a second INS in cases that use a Gauss-Markov model are not as significant as for the model replacement method. Overall, the error magnitudes are similar, indicating that any of the described methods can be used without substantially increasing the navigation error.

Including the additional measurements in the model replacement method by averaging the measurements is a simplistic way to handle the multiple INS measurements. While the results for the model replacement show the most improvement over the results from Table 4.2, it may be beneficial to integrate the INS measurements independently before combining them, although it is unclear how one would do that.

Table 4.5 shows results for the different Kalman filter methods of processing INS data when two INS measurements are provided at every time step. The simulation is identical to Table 4.4. The difference between Tables 4.4 and 4.5 is that the three filters that use Gauss-Markov models also use averaged INS outputs as though the averages were the outputs of a single INS. Therefore, they only use a single set of biases, which are effectively bias averages over the multiple INS. This results in less computational cost due to fewer measurements in the Gauss-Markov filters' measurement updates. The smaller number of filter states further decreases computational cost, but averaging the INS measurements before sending them to the filter results in the individual biases of each INS not being observable. The observable biases are the average of the two INS biases. The results columns correspond, respectively, to the steady-state RMS position, angular, and velocity error magnitudes averaged over 20 cases, similar to Table 4.4. Error is computed between each filter's estimate and the

truth-model simulation's truth state.

Table 4.5: RMS steady-state position, angular, and velocity error magnitudes of the navigation Kalman filters as functions of the filter method for incorporating INS data when using the Starlink and Iridium constellations for a receiver on a plane with two INSs. The INS data are pre-averaged to reduce the number of states and measurement updates in the three filter types that use Gauss-Markov models.

Kalman Filter Type	Steady-State RMS Pos. Error Mag. (m)	Steady-State RMS Angular Error Mag. (°)	Steady-State RMS Vel. Error Mag. (m/s)
Model Replacement	2.8830	0.0288	0.0444
Acceleration Gauss-Markov Model	3.1022	0.0375	0.0573
Angular Rate Gauss-Markov Model	3.1492	0.0269	0.0564
Acceleration & Angular Rate Gauss-Markov Model	2.9653	0.0403	0.0486

The first row of results in Tables 4.4 and 4.5 are identical since the model replacement method averages the two sets of INS measurements in Table 4.4. For all of the Gauss-Markov model methods, the RMS position errors in Table 4.5 are fairly close to those in Table 4.4. This suggests that pre-averaging two sets of INS measurements and only estimating the averaged INS biases does not influence the position error magnitudes. The model replacement method produces the lowest position and velocity errors in Tables 4.4 and 4.5. The ranked order of the different position error magnitudes is the same between both tables. This suggests, that pre-averaging the INS measurements and only estimating the averaged biases can be used with any model replacement or Gauss-Markov method.

4.8 Summary and Conclusions

This paper has defined and implemented multiple algorithms to include INS measurements in a tightly-coupled Radio-Frequency/INS navigation Kalman filter. The methods either

directly integrate INS measurements via model replacement or use a Gauss-Markov process driven by white noise and a typical KF measurement update to include INS data. The pros and cons of each method are discussed. Navigation error results for each algorithm from several simulations are shown. Iridium and Starlink LEO constellations are simulated to provide radio-navigation data in the form of carrier Doppler shift measurements. The simulations include a fast-moving receiver on an aircraft, a slow-moving receiver on a tricycle, and an aircraft case with two redundant sets of INS measurements.

All of the architectures produce similar levels of navigation accuracy. In some cases, the model replacement method yields more accurate results, but in others the Gauss-Markov algorithms are more accurate. While there are some differences in the navigation error results between algorithms, they are not large enough to justify using one method over another solely on the basis of improved accuracy. Thus, the method used to include INS measurements in a tightly-coupled RF/INS filter can be based on user preference and system requirements. The model replacement method requires fewer states and less tuning. This method, however, can be more difficult to implement because of the challenges of numerically integrating the INS model equations. Model replacement uses the measured INS sensor data outside the framework of the measurement update of a traditional Kalman filter. This can make the implementation of model replacement methods confusing for those only familiar with standard Kalman filters. The Gauss-Markov methods require more state elements and tuning parameters, and effort must be expended in order to pick reasonable values of the tuning parameters, but such filters can be implemented by applying standard Kalman filter measurement updates to the INS data. System memory and power requirements may limit the number of states, forcing the model replacement method to be chosen.

There is evidence that direct integration using model replacement may produce better results for systems with slow-moving receivers. Gauss-Markov models may produce more accurate

navigation results for systems with fast-moving receivers. More simulations and the consideration of additional cases are needed to make definitive conclusions.

To include multiple INS measurements, the Gauss-Markov algorithms can simply append measurement models and measurements to the existing measurement update step after adding additional bias states for the additional accelerometers and rate gyros. Model replacement requires averaging all INS measurements before its dynamic propagation step, unless one wants to develop some sort of multiple-model replacement algorithm, if such a thing is even practical. Initial results suggest averaging INS measurements and using model replacement outperforms Gauss-Markov filter designs. The RMS position error differences between the methods, however, are not large. If the Gauss-Markov methods are modified to use pre-averaged INS data and to estimate only averaged biases rather than individual INS units' biases, then their performance remains relatively unchanged.

4.9 Possible Future Work

Future work may include a deeper investigation into how to incorporate multiple simultaneous INS measurements. Another avenue of future work is to perform a more in-depth Monte Carlo analysis with different receiver velocities and initial conditions to better compare the different algorithms for incorporating INS measurements into a tightly-coupled filter.

4.10 Acknowledgements

This work was supported in part by the NAL Research Corp. under contract No. AMKH7VGZ. Dr. Matthew Zeiger was the contract monitor. Mark Psiaki has a financial interest in this research through related consulting work that he has conducted for NAL Research Corp.

Chapter 5

DOP Analysis for a LEO Navigation Constellation that Relies on Doppler Shift and Pseudorange

5.1 Abstract

A study is conducted on Dilution of Precision (DOP) metrics for a Low Earth Orbit (LEO) navigation constellation that uses a combination of carrier Doppler shift and pseudorange measurements to provide a point solution capability for position, clock offset, velocity, and clock offset rate. This study is being conducted in support of efforts to use radio-frequency signals from large LEO constellations as augmentations or alternatives of existing GNSS. This study develops methods to analyze the beneficial effects of adding a sparse set of pseudorange-capable satellites to a large LEO constellation that provides a global navigation capability primarily through the use of carrier Doppler shift. This study aims to find one or more DOP metrics that can be used to predict the navigation accuracy of any navigation system using carrier Doppler shift and pseudorange measurements. The study then considers how these DOP metrics can be used for LEO navigation constellation design. The OneWeb constellation is used as an example for constellation design based on DOP metrics.

5.2 Introduction

Navigation systems using massive LEO constellations as an alternative to current Medium Earth Orbit (MEO) Global Navigation Satellite Systems (GNSS) have been researched in a number of papers, including [46], [20], [42], [38], [32], [45], [8], and [30]. In [46], the costs and benefits of using LEO satellites for navigation are discussed. The paper analyzes the potential of a navigation system based on LEO satellites producing pseudorange measurements. Using LEO satellites to augment GNSS is examined in [20]. In [42], a point solution for position and velocity is proposed using only carrier Doppler shift from massive LEO constellations. In [38] and [32], carrier Doppler shift measurements from LEO satellites are fused with measurements from an Inertial Navigation System (INS) to navigate with fewer than the eight simultaneous measurements required for the carrier-Doppler-shift-based point solution of [42]. Carrier Doppler shift provides the capability to produce accurate position, velocity, and receiver clock offset rate estimates in [42], [38], and [32]. The receiver clock offset estimate, however, is orders of magnitude less accurate than traditional pseudorange-based MEO GNSS, when using only carrier Doppler shift. The poor clock accuracy poses a significant problem and degrades the utility of a Doppler-only navigation system.

Also, proposed in [42] is a Geometric Dilution of Precision (GDOP) analysis using only carrier Doppler shift. Reference [30] considers the inclusion of pseudorange measurement capabilities on the signals from a subset of the LEO satellites along with carrier Doppler shift measurements on all of the signals, and a GDOP analysis using both pseudorange and carrier Doppler shift measurements is investigated to attempt to increase the accuracy of the receiver clock offset estimate. Although a single GDOP metric was not found that worked for all cases in [30], it was shown that the addition of one or two pseudorange measurements to augment a Doppler-only system can significantly reduce the receiver clock offset error. By including a few coarse pseudorange measurements, the utility of a Doppler-

based navigation system is increased. This study extends the work of [42] and [30] by finding a single combined pseudorange and carrier Doppler shift DOP analysis that works for all cases. It has been carried out with the goal of developing constellation design and analysis methods that support the development of navigation systems which are based primarily on carrier Doppler shift observables while supporting sub-microsecond clock offset accuracy through the inclusion of a small number of pseudorange measurements.

DOP is a commonly used predictor of accuracy for radio-navigation systems. The traditional GNSS DOP analysis considers only a navigation system that relies on pseudorange [36]. In [2], a GDOP analysis using only carrier Doppler shift from GPS satellites is analyzed. The paper made the simplifying assumption that the receiver is not moving and that the receiver clock offset is known. These assumptions remove some challenges associated with a Doppler-only GDOP analysis, but they result in the GDOP analysis only being useful in situations when the receiver is not moving. Additionally, unit issues when using carrier Doppler shift measurements in the GDOP analysis are not addressed in [2]. In [39], the GDOP analysis from [2] is used to analyze the navigation potential of LEO constellations. The assumptions of [2] are not relaxed in [39] and the unit issues in [2] are not addressed. Thus, the results are useful only in specific situations. A GDOP analysis that addresses the general case when using only carrier Doppler shift observables is developed in [42]. The simplifying assumptions of [2] are discarded in [42]. Thus, the Doppler-only GDOP analysis in [42] predicts the accuracy of the position, receiver clock offset, velocity, and receiver clock offset rate for the system under conditions of general motion and without any assumptions of *a priori* knowledge about receiver clock offset or clock offset rate. Additionally, the unit issues when using carrier Doppler shift measurements in a GDOP analysis are resolved in [42] with the development of normalizing factors. Based on the work in [30], [36], and [42], this paper proposes a combined pseudorange and carrier Doppler shift DOP analysis

that predicts the likely accuracy of the position, clock offset, velocity, and clock offset rate of a LEO navigation system. The work focuses on systems with a small number of noisy pseudorange measurements with accuracies on the order of 100s of meters. In cases with four or more accurate pseudorange measurements, a traditional pseudorange-only GDOP analysis would be preferred in this paper's analysis.

A challenge when performing a combined DOP analysis involving pseudorange and carrier Doppler shift is the need for unit agreement. Achievement of the needed agreement produces a non-dimensional measurement sensitivity matrix and a corresponding non-dimensionalized approximation of the resultant batch filter estimation error covariance matrix. A suitable non-dimensionalized error covariance matrix can be used to define a sensible DOP parameter. Reference [30], which was an early effort on the same topic as the present paper, developed several non-dimensionalization schemes. None of them yielded a single useful DOP metric for all scenarios. The present study attempts to determine a single non-dimensionalized DOP parameter that can be used for all scenarios. In addition to the development of a DOP analysis to characterize quickly the navigation accuracy of a given system, this study presents an example of how to perform basic constellation design using its DOP analysis. The goal of the constellation design example is to identify the dominant factors that govern the achievable accuracy of a combined pseudorange and carrier Doppler shift LEO navigation system that uses a sparse set of pseudorange-capable satellites.

The development of a single DOP analysis that works for all scenarios is difficult due to the varying units and magnitudes of the values in the DOP matrix. A number of methods for non-dimensionalizing the terms in a GDOP analysis have been proposed in [30]. To find a method that works for all cases, this study splits the GDOP into two separate DOP metrics. One characterizes the accuracy of the position, velocity, and clock offset rate of a combined pseudorange and Doppler-shift navigation system. The other DOP metric characterizes

only the receiver clock offset accuracy. The use of two DOP metrics works well because there are, in reality, two nearly separate estimation problems when using noisy pseudorange measurements and carrier Doppler shift to navigate. One estimation problem relies mainly on the pseudorange measurements to estimate the clock offset. The other problem relies mainly on carrier Doppler shift to estimate the position, velocity, and clock offset rate.

This study tests its developments by using simulated data from LEO communication constellations such as Starlink, Kuiper, and OneWeb. The simulated data are used by a batch filter to determine the position/clock-offset/velocity/clock-offset-rate navigation solution error and its corresponding error covariance matrix. Results from the batch filter are used to verify that the DOP analyses produce accurate predictions about the covariance. Due to the use of two DOP metrics, two separate maps of DOP vs. latitude and longitude are created for each constellation. Although this constitutes more data to consider than a single GDOP map, the two DOP maps provide concise information on the accuracy of navigation for a combined pseudorange and carrier Doppler shift LEO navigation system. The use of the two DOP metrics allows this study to employ a single DOP non-dimensionalization method for a combined pseudorange and carrier Doppler shift system in all significant cases.

This study also performs basic constellation design guided by its DOP analysis using the OneWeb constellation as an example. The study considers how many and which satellites need to include a pseudorange capability in order to reduce navigation error significantly over the entire Earth. Also, the study investigates the benefits of alternating ascending and descending nodes versus grouped ascending and descending nodes, among other constellation design characteristics. The quick and simple implementation of a DOP analysis allows for the rapid evaluation of changes in navigation accuracy due to variations of the simulated constellations. Additionally, the simplified DOP matrix can be used to identify characteristics of the system that impact navigation accuracy.

This paper makes three contributions to the subject of navigation using the carrier Doppler shift and pseudorange observables from massive LEO constellations: First, it develops a DOP analysis that can be used in combined pseudorange and carrier Doppler shift systems to predict navigation accuracy. Second, an analysis is performed on the impacts of adding a spare set of pseudorange-capable satellites to LEO constellations that provide navigation through carrier Doppler shift measurements. Finally, the use of DOP metrics in an example LEO constellation design scenario is shown.

The remainder of this paper is organized as follows. The second section reviews the measurement models used in the analyses, pseudorange and carrier Doppler shift. The LEO constellations used in the paper are reviewed in the third section. In the fourth section, a batch filter is developed for the combined pseudorange/carrier Doppler shift navigation point solution problem. The fifth section presents a truth-model simulation and documents how the batch filter performs when used with the simulation's output data. The sixth section explains the DOP analysis, which is the main contribution of this paper, and studies its performance. The seventh section performs an example constellation design analysis utilizing the DOP analysis with the OneWeb constellation as a basis. The paper finishes with a summary and conclusions.

5.3 Measurement Models

This section presents the measurement models that are used to develop a point-solution batch filter and the corresponding DOP analysis. The included models are PseudoRange (PR) and carrier Doppler shift. High-fidelity versions of these models are used in the point-solution batch filter. Simplified versions are used in the DOP analysis.

5.3.1 Pseudorange

The pseudorange measurement model is

$$h^j_{PR} = \rho^j(\vec{r}, \delta_R, t_R) = \sqrt{[\vec{r} - A(\omega_E \delta t^j_p)\vec{r}^j(t_R - \delta_R - \delta t^j_p)]^T[\vec{r} - A(\omega_E \delta t^j_p)\vec{r}^j(t_R - \delta_R - \delta t^j_p)]} + c(\delta_R - \delta^j) + c\delta t^j_{trop} + c\delta t^j_{iono} \tag{5.1}$$

where ρ^j is the pseudorange from the j^{th} satellite, $\vec{r}$ is the unknown Earth-Centered Earth-Fixed (ECEF) position of the receiver, ω_E is the rotation rate of the Earth, $\vec{r}^j$ is the ECEF position of the jth satellite, t_R is the erroneous receiver clock time, δ_R is the unknown receiver clock offset, δ^j is the transmitter clock offset of the j^{th} satellite, δt^j_{trop} is the tropospheric delay of the signal from the j^{th} satellite, δt^j_{iono} is the delay due to ionosphere for the j^{th} satellite's signal, and δt^j_p is the propagation time from the j^{th} satellite to the receiver, which is found by solving the following equation [42]:

$$\delta t^j_p = \frac{1}{c}\sqrt{[\vec{r} - A(\omega_E \delta t^j_p)\vec{r}^j(t_R - \delta_R - \delta t^j_p)]^T[\vec{r} - A(\omega_E \delta t^j_p)\vec{r}^j(t_R - \delta_R - \delta t^j_p)]} + \delta t^j_{trop} + \delta t^j_{iono} \tag{5.2}$$

The Earth rotation direction cosines matrix which is used in Eqs. (5.1) and (5.2) is [42]:

$$A(\omega_E \delta t^j_p) = \begin{bmatrix} cos(\omega_E \delta t^j_p) & sin(\omega_E \delta t^j_p) & 0 \\ -sin(\omega_E \delta t^j_p) & cos(\omega_E \delta t^j_p) & 0 \\ 0 & 0 & 1 \end{bmatrix} \tag{5.3}$$

5.3.2 Carrier Doppler Shift

Carrier Doppler shift equals the negative derivative of Accumulated Delta Range (ADR) with respect to the erroneous receiver clock time divided by the nominal carrier wavelength [42]:

$$D^j = -\frac{1}{\lambda}\frac{d\Delta\rho^j_{ADR}}{dt_R} \tag{5.4}$$

where λ is the wavelength of the signal in meters, D^j is the carrier Doppler shift from the j^{th} satellite, and ADR in meters is denoted as $\Delta\rho^j_{ADR}$. The ADR model is [42]:

$$\begin{aligned}\Delta\rho^j_{ADR}(\vec{r},\delta_R,t_R) = \lambda\phi^j = \sqrt{[\vec{r}-A(\omega_E\delta t^j_p)\vec{r}^j(t_R-\delta_R-\delta t^j_p)]^T[\vec{r}-A(\omega_E\delta t^j_p)\vec{r}^j(t_R-\delta_R-\delta t^j_p)]} \\ + c(\delta_R-\delta^j) + c\delta t^j_{trop} - c\delta t^j_{iono} + \lambda\beta^j\end{aligned} \tag{5.5}$$

where the beat carrier phase is denoted as ϕ^j, and β^j is the beat carrier phase bias. Notice that the pseudorange and ADR equations in Eqs. (5.1) and (5.5) are nearly identical. The only differences are the sign of the ionospheric delay and the addition of the beat carrier phase bias term. Substitution of Eq. (5.5) into Eq. (5.4) followed by multiplication of both sides by λ and other manipulations yields the analytic carrier Doppler shift model [42]:

$$-\lambda D^j = \frac{(\hat{\rho}^j)^T(\vec{v}-\vec{v}^j)\left[\frac{1+\frac{d\delta^j}{dT^j}}{1+\frac{1}{c}\{a^j_{\delta tp}-(\hat{\rho})^T\vec{v}^j\}}\right] + c\frac{d\delta_R}{dT_R} - c\frac{d\delta^j}{dT^j}}{1+\frac{d\delta_R}{dT_R}} \tag{5.6}$$

if the time derivatives of the troposphere and ionosphere are ignored. The quantity $\hat{\rho}^j$ is the ECEF unit direction vector that points from the j^{th} satellite to the receiver, $\vec{v}$ is the unknown ECEF velocity of the receiver, $\vec{v}^j$ is the ECEF velocity of the j^{th} satellite, T^j is the true signal transmission time of the j^{th} satellite, T_R is the true signal reception time, and

the time rate of change of propagation delay causes the term, $a^j_{\delta tp}$, to appear. This term is defined as [42]:

$$a^j_{\delta tp} = -\hat{\rho}^j \cdot \{\vec{\omega}_E \times [A(\omega_E \delta t^j_p)\vec{r}^j(t_R - \delta_R - \delta t^j_p)]\} \tag{5.7}$$

where the ECEF rotation rate vector due to the Earth's rotation is defined as $\vec{\omega}_E = [0; 0; \omega_E]$.

The carrier Doppler shift model in Eq. (5.6) is sufficient for use in the GPS velocity solution, but the lack of the time derivatives of the atmospheric terms might cause issues when performing a carrier-Doppler-shift-only position solution. To be safe, the effects of the atmospheric terms on the carrier Doppler shift are included in the batch filter model. In order to make use of the ADR model in Eq. (5.5) and also include time derivatives of the atmospheric delay terms, a finite-difference method is used for the carrier Doppler shift measurement model of this paper's filter. This model implements a five-point central difference that approximates Eq. (5.4) [42]:

$$\begin{aligned} h^j_{Dopp} = \left(\frac{-1}{12\Delta_{FD}\lambda}\right) \Bigg[& \Delta\rho^j_{ADR}\left(\vec{r} - 2\frac{\vec{v}\Delta_{FD}}{1+\dot{\delta}_R}, \delta_R - 2\frac{\dot{\delta}_R\Delta_{FD}}{1+\dot{\delta}_R}, t_R - 2\Delta_{FD}\right) \\ & - 8\Delta\rho^j_{ADR}\left(\vec{r} - \frac{\vec{v}\Delta_{FD}}{1+\dot{\delta}_R}, \delta_R - \frac{\dot{\delta}_R\Delta_{FD}}{1+\dot{\delta}_R}, t_R - \Delta_{FD}\right) \\ & + 8\Delta\rho^j_{ADR}\left(\vec{r} + \frac{\vec{v}\Delta_{FD}}{1+\dot{\delta}_R}, \delta_R + \frac{\dot{\delta}_R\Delta_{FD}}{1+\dot{\delta}_R}, t_R + \Delta_{FD}\right) \\ & - \Delta\rho^j_{ADR}\left(\vec{r} + 2\frac{\vec{v}\Delta_{FD}}{1+\dot{\delta}_R}, \delta_R + 2\frac{\dot{\delta}_R\Delta_{FD}}{1+\dot{\delta}_R}, t_R + 2\Delta_{FD}\right) \Bigg] \end{aligned} \tag{5.8}$$

where the nominal difference of the erroneous receiver clock time t_R and $\dot{\delta}_R = \frac{d\delta_R}{dT_R}$ steps in the finite difference calculation is denoted as Δ_{FD}.

5.3.3 Simplified Measurement Models for use in DOP Analysis

The models in the preceding two subsections are complicated and can be time-consuming to calculate. In this subsection, simplified versions of Eqs. (5.1) and (5.6) are presented. These simplified models are used to develop this paper's DOP analyses. The simplified form of the pseudorange model is:

$$\rho^j(\vec{r},\delta_R,t_R) = \sqrt{[\vec{r} - A(\omega_E\delta t_p^j)\vec{r}^j(t_R-\delta_R-\delta t_p^j)]^T[\vec{r} - A(\omega_E\delta t_p^j)\vec{r}^j(t_R-\delta_R-\delta t_p^j)]} + c\delta_R - c\delta^j \tag{5.9}$$

Note how the ionosphere and neutral atmosphere terms have been neglected. Experience shows that they do not contribute significantly to DOP-type linearized error covariance calculations.

In order to form a simplified carrier Doppler shift model for GDOP analysis a few approximations are made. Substitution into Eq. (5.6) of the approximations

$$\begin{aligned} 1 &\approx 1 + \frac{d\delta^j}{dT^j} \\ 1 &\approx 1 + \frac{d\delta_R}{dT_R} \\ 1 &\approx 1 + \frac{1}{c}\left[a_{\delta tp}^j - (\hat{\rho}^j)^T\vec{v}^j\right] \end{aligned} \tag{5.10}$$

yields the simplified model [42]:

$$-\lambda D^j = (\hat{\rho}^j)^T(\vec{v}-\vec{v}^j) + c\frac{d\delta_R}{dT_R} - c\frac{d\delta^j}{dT^j} \tag{5.11}$$

which will be used in the DOP analysis. Equations (5.9) and (5.11) retain the dominant terms from Eqs. (5.1) and (5.6) for GDOP analysis, but they are simpler and lend themselves

more easily to quick analysis.

5.4 LEO Constellations

Three LEO constellations are considered in this paper. They have all been designed primarily for communication purposes. They are Starlink, OneWeb, and Kuiper. The Starlink and OneWeb constellations currently have a portion of their constellations in orbit. The Kuiper constellation is still in the pre-flight phase.

In Table 5.1, possible characteristics of these LEO constellations are shown. Data for each constellation has been found from the FCC documents [13, 12, 1]. Due to all of the constellations not being fully deployed, these numbers are subject to change. The numbers in Table 5.1 represent, at best, guesses of the characteristics of the final constellation's orbital configurations based on the cited FCC filings. As the constellation designs mature and as modifications to original FCC filings are submitted, these configurations are likely to change. This paper's principles for constellation analysis, however, will not change.

Table 5.1: LEO Constellation Orbital Parameters

Name	No. of Planes	Sats. per Plane	Total No. Sats.	Inclination (deg.)	Altitude(s) (km)
Starlink	51	50-75	2825	53.8-81.0	1110-1325
Kuiper	34	34	1156	51.9	630
OneWeb	18	40	720	87.9	1200

A necessary condition for point solution navigation using only carrier Doppler shift is that measurements must be available simultaneously from eight or more satellites [42]. For the Starlink and OneWeb constellations, this requirement may be met everywhere on Earth, depending on the Earth coverage pattern of the transmitted signals [42, 32]. On the other hand, the Kuiper constellation does not have a large number of visible satellites outside of the $\pm 60^o$ latitude range due to its limited inclination of 51.9^o.

One of the questions that will be considered in the present paper concerns whether the availability of pseudorange from fewer than four satellites can reduce the overall requirement below eight satellites when using a combination of pseudorange from some satellites and carrier Doppler shift from all satellites. These mixed data would be used in a batch filter point solution for the position, receiver clock offset, velocity, and receiver clock offset rate.

For global coverage, it might be practical to use a combination of multiple constellations. More visible satellites will help navigation. The DOP analysis developed in this work can be used to determine the predicted performance for a particular set of satellites with particular capabilities for enabling pseudorange measurements, and carrier Doppler shift measurements, or both.

Figure 5.1, which is borrowed from [44], shows the OneWeb constellation's satellite orbital tracks in red and the 7.5^o elevation mask footprints in magenta. A single satellite and its footprint are highlighted in yellow. This figure shows the global coverage of the OneWeb constellation and the large number of visible satellites at any given location.

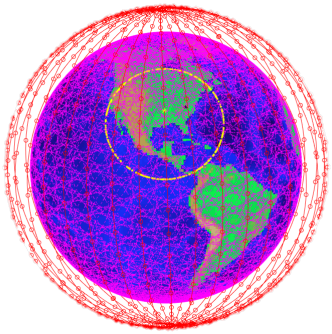

Figure 5.1: Satellite orbits (red curves) of OneWeb satellites (red circles). Each satellite has a circular footprint on the Earth (magenta) based on a 7.5^o elevation mask. A single satellite and footprint are emphasized in yellow [44].

5.5 Batch Filter

This paper's DOP analysis is concerned with the accuracy of a batch filter that calculates a point solution from a combination of pseudorange and carrier Doppler shift measurements for a single time epoch. It makes no use of a dynamics model or *a priori* information, unlike a sequential Kalman filter. Some of the satellite signals may provide only pseudorange measurements, others only carrier Doppler shift measurements, and some may provide both types of observables. The batch filter's signal model includes troposphere and ionosphere terms.

The available pseudorange and carrier Doppler shift measurements along with satellite ephemerides are used by the batch filter to calculate position, receiver clock offset, velocity, and receiver clock offset rate by using the Gauss-Newton method [16] to solve the corresponding nonlinear least-squares problem. The batch filter minimizes a weighted nonlinear least-squares cost function that equals the negative-log-likelihood of the pseudorange and carrier Doppler shift measurements. The solution quantities that it solves for by minimization of this cost function are the ECEF receiver position, $\vec{r}$, range-equivalent receiver clock offset, $c\delta_R$, the ECEF receiver velocity, $\vec{v}$, and the range-rate-equivalent receiver clock offset rate, $c\dot{\delta}_R$. The cost function to be minimized is:

$$\begin{aligned} J(x) &= 0.5 \sum_{i=1}^{M} \left[\frac{y_{PR}^{i} - h_{PR}^{i}(x)}{\sigma_{PR}} \right]^2 + 0.5 \sum_{j=M+1}^{M+N} \left[\frac{y_{Dopp}^{j} - h_{Dopp}^{j}(x)}{\sigma_{Dopp}} \right]^2 \\ &= \frac{1}{2} [y - h(x)]^T R^{-1} [y - h(x)] \end{aligned} \tag{5.12}$$

where

$$y = \begin{bmatrix} y_{PR}^{1} \\ \vdots \\ y_{PR}^{M} \\ y_{Dopp}^{M+1} \\ \vdots \\ y_{Dopp}^{M+N} \end{bmatrix} \tag{5.13}$$

is the $(M+N) \times 1$ vector of pseudorange and carrier Doppler shift measurements, M being the number of pseudorange measurements and N being the number of carrier Doppler shift measurements,

$$x = \begin{bmatrix} \vec{r} \\ c\delta_R \\ \vec{v} \\ c\dot{\delta}_R \end{bmatrix} \tag{5.14}$$

is the unknown 8×1 vector to be estimated, and

$$h(x) = \begin{bmatrix} h_{PR}^{1}(x) \\ \vdots \\ h_{PR}^{M}(x) \\ h_{Dopp}^{M+1}(x) \\ \vdots \\ h_{Dopp}^{M+N}(x) \end{bmatrix} \tag{5.15}$$

is the vector of functions of the two measurement models, with $h_{PR}(x)$ and $h_{Dopp}(x)$ be-

ing the modeled pseudorange and carrier Doppler shift, respectively, based on the current guessed x vector. They are computed using the models in Eqs. (5.1) and (5.8) after solving for the propagation delay using Eq. (5.2). Note that the Doppler shift measurement and model superscript values, $M+1$, ..., $M+N$, are distinct from those of the pseudorange superscript in order to avoid possible confusion of re-using superscript values in a way that might erroneously imply that, if the same superscript index is used for both a pseudorange and a carrier Doppler shift, then they correspond to the same satellite. This is not necessarily the case. Note, however, that it is possible that a common satellite produces both pseudorange and carrier Doppler shift measurements. In that case, the corresponding pseudorange and carrier Doppler shift superscripts will refer to one and the same satellite even though they have different values. The diagonal $(M+N)\times(M+N)$ measurement error covariance matrix is:

$$R = \begin{bmatrix} \sigma_{PR}^2 & 0 & 0 & 0 & \dots & 0 \\ \vdots & \ddots & \vdots & \vdots & \dots & \vdots \\ 0 & 0 & \sigma_{PR}^2 & 0 & \dots & 0 \\ 0 & 0 & 0 & \sigma_{Dopp}^2 & 0 & 0 \\ \vdots & \vdots & \vdots & \vdots & \ddots & \vdots \\ 0 & 0 & \dots & 0 & 0 & \sigma_{Dopp}^2 \end{bmatrix} \tag{5.16}$$

where σ_{PR} and σ_{Dopp} are the measurement error standard deviations of the pseudorange and carrier Doppler shift measurements, respectively.

In addition to the optimal estimate x_{opt}, which is the value of x that minimizes the cost function in Eq. (5.12) the batch filter produces the following approximation of its estimation

error covariance matrix:

$$P_{xx} = (H^T R^{-1} H)^{-1} \tag{5.17}$$

where

$$H = \left.\frac{\partial h}{\partial x}\right|_{x_{opt}} \tag{5.18}$$

The matrix P_{xx} is an approximation of the Cramer-Rao lower bound to the batch filter's true estimation error covariance matrix. In many cases, it gives a reasonable indication of the actual filter accuracy.

The point solution accuracy is denoted by the matrix in Eq. (5.17). The initial developments of this paper's DOP analysis approximates this matrix in a non-dimensional form. The P_{xx} matrix will also be used to assess the efficacy of the DOP analysis. Scalar DOP results will be considered good to the extent that they serve to predict the magnitudes of the corresponding diagonal elements of P_{xx}.

In a sense, the DOP analysis discussed in later sections is a simplified version of the covariance analysis from the point-solution batch filter. To determine a similar metric to GDOP, the trace of the batch filter's covariance matrix could be computed. The calculation of GDOP from the batch filter's covariance would have similar scaling issues to the DOP analysis discussed below. While the point-solution batch filter produces more accurate results due to the use of more accurate measurement models, its implementation is more complicated, and it does not produce a single dimensionless metric unlike, the DOP analysis.

The increased complexity of a combined pseudorange and Doppler shift DOP analysis can make the use of a robust covariance analysis seem more attractive even though the implemen-

tation of a covariance analysis also requires more work from the user than a DOP analysis. A robust covariance analysis would involve calculating the actual covariance matrix per Eq. (5.17) and using various square roots of partial traces as accuracy metrics rather than scalar, non-dimensional DOP values. In reality, a DOP analysis is a simplified covariance analysis that only uses the diagonal elements from the covariance analysis. The additional complications of unit issues in a combined DOP do not arise when performing a covariance analysis because a single dimensionless metric is not calculated in a covariance analysis. One benefit of the DOP analysis is that the single dimensionless value can be thought of as a gain on the error of a system. By thinking of the results in this way, the DOP analysis provides a more easily understood result than a typical covariance analysis to users not familiar with filtering and estimation.

5.6 Evaluation of Batch Filter using a Truth-Model Simulation

The batch filter has been tested using simulated truth-model data from three different sets of cases. The three sets of cases correspond to the three constellations listed on the lines of Table 5.1.

The simulation assumes that a measurement for a satellite can be produced if it is above a 7.5^o elevation mask as measured at the receiver. Measurements include carrier Doppler shift and pseudorange. The range-rate equivalent carrier Doppler shift measurement error standard deviation is set to $\lambda\sigma_{Dopp} = 0.01$ m/sec, and the pseudorange measurement error standard deviation is set to 120 m. This range-rate accuracy is similar to that of GPS signals in typical applications with typical carrier-to-noise density ratios and typical receiver PLL

or FLL tracking loop bandwidths. In practice, the available range-rate accuracy depends on a number of factors in the receiver and the carrier-to-noise density ratio and can vary from this assumed value. Due to the assumption of narrow-band signals, perhaps only 40 kHz wide, the simulated pseudorange measurement error standard deviation is about two orders of magnitude larger than for typical GNSS signals. While the pseudorange measurement error is too large for accurate navigation alone, it can still aid in determining a navigation solution, especially the receiver clock offset.

One set of truth-model simulations assumes that there are zero satellite ephemeris or clock errors. Another set of truth-model simulations includes satellite ephemeris and clock errors as follows: The satellite positions used in the filter have per-axis errors with zero-mean and two-meter standard deviation relative to their "truth" values. The filter's satellite velocities have errors with a mean of zero and standard deviations of 0.002 m/s relative to their truth values. The filter's satellite clock offset is modeled as being zero-mean with a standard deviation of 4×10^{-7} s relative to the "truth" values. The filter's satellite clock offset rate is modeled as being zero-mean with a standard deviation of 3.3×10^{-11} s/s relative to the "truth" values. These satellite ephemeris and transmitter clock error statistics are believed to be achievable for constellations with ground control segments that track the satellites and their clock and that fly high-quality ovenized crystal oscillators or chip-scale atomic clocks. All quantities from this paragraph are borrowed from [42]. The ionosphere and troposphere models used in truth-model simulation match the models used in the batch filter exactly.

The truth locations for each filter run have been randomly selected over the entire Earth with altitudes ranging from 0 to 9,144 m. Each set of cases consists of 1000 example runs of the batch filter with 1000 different sets of simulated data, one set each from 1000 different user locations on the Earth. For each location, two cases are run. One for perfect agreement between the filter and truth-model ephemerides and transmitter clock offsets and rates and

a second one with the stated statistics of disagreement.

For each of the three constellations and each user receiver location, three cases have been run. One case assumes that all visible satellites produce pseudorange and carrier Doppler shift measurements. A second case assumes that a randomly selected subset of only ten of the visible satellites produce carrier Doppler shift measurements, while another randomly selected subset of only two of the visible satellites produce pseudorange measurements. A third case uses only the ten carrier Doppler shift measurements of the second case while deleting the two pseudorange measurements. These latter two cases may be more indicative of what is actually possible due to the fact that these constellations might not enable every visible satellite to produce a usable signal at any given user location.

5.6.1 Performance Results

In Table 5.2, results from 1000 runs of the batch filter with random initial positions are shown. This table shows results for cases with the stated statistics of disagreement between the filter and truth-model ephemerides and transmitter clock offsets and offset rates. The Table-5.2 results assume that all visible satellites return both coarse pseudorange data and carrier Doppler shift data. For the Starlink constellation, there are more than 50 visible satellites for each run. For the OneWeb constellation, there are around 20 visible satellites for each run. The extremely large number of visible satellites results in accurate navigation point solutions from the batch filter because each of the satellites provides a pseudorange and a carrier Doppler shift observable.

The RMS of the norm of the position error is around 2-4 meters over all cases, and the maximum error magnitude is around 10 meters. The receiver clock offset error is much smaller than for any of the results of [42]. This improvement is caused by the inclusion of

Table 5.2: Batch filter Monte-Carlo truth-model simulation error statistics for Starlink, OneWeb, and Kuiper constellations with disagreement between the filter and truth-model ephemerides, transmitter clock offsets, and offset rates with all visible satellites returning pseudorange and carrier Doppler shift data.

Set of 1000 Cases	RMS of $\|\|\vec{r}_{opt} - \vec{r}_{truth}\|\|$ (m)	Max of $\|\|\vec{r}_{opt} - \vec{r}_{truth}\|\|$ (m)	RMS of $\|\|\vec{v}_{opt} - \vec{v}_{truth}\|\|$ (m/s)	Max of $\|\|\vec{v}_{opt} - \vec{v}_{truth}\|\|$ (m/s)	RMS of $\delta_{R_{opt}} - \delta_{R_{truth}}$ (ns)	Max of $\|\delta_{R_{opt}} - \delta_{R_{truth}}\|$ (ns)
Starlink	2.8121	9.1853	0.0112	0.0437	64.9826	197.003
OneWeb	4.2062	12.357	0.0159	0.0500	126.160	417.559
Kuiper*	3.4732	8.5746	0.0262	0.0860	100.685	394.389

*Latitude range limitation of $\pm$ 50^o

pseudorange measurements, even though those measurements are coarse in comparison to MEO-based GNSS signals. Some results from the batch filter will be used to help validate the DOP analysis discussed in the DOP analysis section.

In Table 5.3, results are shown from 1000 runs of the batch filter for the three different constellations with perfect agreement between the filter and truth-model ephemerides. Again, all visible satellites provide pseudorange and carrier Doppler shift observables. A comparison of the results in Tables 5.2 and 5.3 indicates that errors in the satellite ephemerides, clock offsets, and clock offset rates cause a modest degradation of accuracy: The estimation error summary statistics in Table 5.3 are somewhat smaller than their corresponding values on Table 5.2.

5.6.2 Results for Reduced Satellite Availability

Two special cases noted above reduce the number of visible signals significantly for the Starlink constellation. The reduction in the number of measurements results in significantly larger errors, as can be seen in Table 5.4 relative to the corresponding full-satellite-availability

Table 5.3: Combined full pseudorange and carrier Doppler shift availability batch filter results for Starlink, OneWeb, and Kuiper constellations with perfect agreement between the filter and truth-model ephemerides, transmitter clock offsets, and offset rates.

Set of 1000 Cases	RMS of $\|\|\vec{r}_{opt} - \vec{r}_{truth}\|\|$ (m)	Max of $\|\|\vec{r}_{opt} - \vec{r}_{truth}\|\|$ (m)	RMS of $\|\|\vec{v}_{opt} - \vec{v}_{truth}\|\|$ (m/s)	Max of $\|\|\vec{v}_{opt} - \vec{v}_{truth}\|\|$ (m/s)	RMS of $\delta_{R_{opt}} - \delta_{R_{truth}}$ (ns)	Max of $\|\delta_{R_{opt}} - \delta_{R_{truth}}\|$ (ns)
Starlink	1.7138	4.3121	0.0073	0.0217	46.271	156.593
OneWeb	2.7838	7.6404	0.0100	0.0352	90.389	350.800
Kuiper*	1.9469	5.2525	0.0141	0.0441	72.311	240.208

*Latitude range limitation of $\pm$ 50^o

case reported in Table 5.2.

Table 5.4: Combined pseudorange and carrier Doppler shift batch filter results for Starlink with limited numbers of available satellites and observables and with errors between the true and filter satellite ephemerides, transmitter clock offsets, and offset rates.

Reduced Signal Availability Case	RMS of $\|\|\vec{r}_{opt} - \vec{r}_{truth}\|\|$ (m)	Max of $\|\|\vec{r}_{opt} - \vec{r}_{truth}\|\|$ (m)	RMS of $\|\|\vec{v}_{opt} - \vec{v}_{truth}\|\|$ (m/s)	Max of $\|\|\vec{v}_{opt} - \vec{v}_{truth}\|\|$ (m/s)	RMS of $\delta_{R_{opt}} - \delta_{R_{truth}}$ (ns)	Max of $\|\delta_{R_{opt}} - \delta_{R_{truth}}\|$ (ns)
0 pseudorange 10 Doppler	30.9991	219.917	0.1412	1.2324	4181587	30126511
2 pseudorange 10 Doppler	17.3204	91.4872	0.0719	0.4610	394.7812	1377.4643

Part of the degradation in accuracy stems from the reduction in the raw number of satellites that produce data. Another driver in the accuracy degradation is the fact that the satellites producing measurements have been randomly selected from all visible satellites at each simulated receiver location. Random selection of measurement-producing satellites can result in cases with poor geometric diversity and poor diversity of the rate of change of the line-of-sight vectors between satellites and the receiver. Reference [42] has shown that the diversity of these two sets of problem quantities is important to achieving low GDOP for the Doppler-only navigation problem. Cases with poor diversity result in the maximum values over all the cases being significantly larger than the RMS values over all the cases.

The two reduced satellite availability cases also highlight how the addition of noisy pseudorange measurements significantly lowers the receiver clock offset error. Note how the second line of Table 5.4 has clock offset estimation error statistics in its last two columns that are many orders of magnitude smaller than the corresponding error statistics in the last two columns of the first line. The reduction occurs because the carrier-Doppler-shift-only solution has poor observability of the receiver clock offset [42]. The two instances of pseudorange data, even though they are coarse, compensate for this poor observability.

5.7 DOP Analysis

This section presents a new combined DOP analysis of pseudorange and carrier Doppler shift. It demonstrates how the new DOP analysis is formed as a combination and extension of a standard DOP analysis for pseudorange-based navigation and the DOP analysis of [42] for Doppler-shift-based navigation.

5.7.1 General DOP Analysis

Using Eqs. (5.9) and (5.11), a linearized relationship between the pseudorange and carrier Doppler shift estimation errors and the corresponding x-vector measurement errors is formed

by using a first-order Taylor series approximation:

$$\begin{bmatrix} \Delta\rho^1 \\ \vdots \\ \Delta\rho^M \\ -\lambda\Delta D^{M+1} \\ \vdots \\ -\lambda\Delta D^{M+N} \end{bmatrix} = \underbrace{\begin{bmatrix} (\hat{\rho}^1)^T & c & 0 & 0 \\ \vdots & \vdots & \vdots & \vdots \\ (\hat{\rho}^M)^T & c & 0 & 0 \\ (\dot{\hat{\rho}}^{M+1})^T & [(\hat{\rho}^{M+1})^T \dot{\vec{v}}^{M+1} + (\dot{\hat{\rho}}^{M+1})^T \vec{v}^{M+1}] & (\hat{\rho}^{M+1})^T & c \\ \vdots & \vdots & \vdots & \vdots \\ (\dot{\hat{\rho}}^{M+N})^T & [(\hat{\rho}^{M+N})^T \dot{\vec{v}}^{M+N} + (\dot{\hat{\rho}}^{M+N})^T \vec{v}^{M+N}] & (\hat{\rho}^{M+N})^T & c \end{bmatrix}}_{A_{DOP}} \begin{bmatrix} \Delta\vec{r} \\ \Delta\delta_R \\ \Delta\vec{v} \\ \Delta\dot{\delta}_R \end{bmatrix} \tag{5.19}$$

where the terms $\Delta\rho^1, \ldots, \Delta\rho^M$ and $\Delta D^{M+1}, \ldots, \Delta D^{M+N}$ are, respectively, the pseudorange and carrier Doppler shift measurement error terms and $\Delta\vec{r}, \Delta\delta_R, \Delta\vec{v}$, and $\Delta\dot{\delta}_R$ are the estimation error terms, and where

$$\dot{\vec{v}}^j = A(\omega_E \delta t_P^j) \frac{d^2\vec{r}^j}{dt^2}\bigg|_{t_r - \delta_R - \delta t_p^j} \tag{5.20}$$

is the j^{th} satellite's ECEF acceleration vector. Note in Eq. (5.19) how the A_{DOP} matrix is defined to be the large $(M+N)\times 8$ matrix on the equation's right-hand side. It is tempting to use the A_{DOP} matrix from Eq. (5.19) to find the DOP metrics of the system:

$$Q = (A_{DOP}^T A_{DOP})^{-1} = \begin{bmatrix} q_{rr} & q_{r\delta_R} & q_{rv} & q_{rdot\delta_R} \\ q_{\delta_R r} & q_{\delta_R\delta_R} & q_{\delta_R v} & q_{\delta_R\dot{\delta}_R} \\ q_{vr} & q_{v\delta_R} & q_{vv} & q_{v\dot{\delta}_R} \\ q_{\dot{\delta}_R r} & q_{\dot{\delta}_R\delta_R} & q_{\dot{\delta}_R v} & q_{\dot{\delta}_R\dot{\delta}_R} \end{bmatrix} \tag{5.21}$$

$$\text{GDOP} = \sqrt{Trace\,[Q]} = \sqrt{Trace[q_{rr}] + q_{\delta_R\delta_R} + Trace[q_{vv}] + q_{\dot{\delta}_R\dot{\delta}_R}} \tag{5.22}$$

In addition to the GDOP metric defined above, additional scalar DOP metrics can be calculated using the A_{DOP} matrix as per [36]. The metrics are found by omitting elements of the Q matrix, defined in Eq. (5.21), (sometimes after performing a transformation to local-level coordinates) before performing the $Trace$ operation. The calculations result in metrics that only predict the accuracy of certain components of the unknown estimated x vector. Typical additional metrics characterize position accuracy, horizontal position accuracy, vertical position accuracy, and receiver clock offset accuracy. Respectively, these are called PDOP, HDOP, VDOP, and TDOP, with TDOP defined as:

$$\text{TDOP} = \sqrt{q_{\delta_R \delta_R}} \tag{5.23}$$

Equation (5.23) only uses the diagonal element of Q that corresponds with the receiver clock offset, which for Eq. (5.19) is the element in the fourth row and the fourth column. The TDOP metric only characterizes the receiver clock's potential accuracy. Since the DOP analysis in Eq. (5.19) includes velocity and receiver clock offset states, another metric similar to PDOP exists that omits information about the accuracy of the receiver clock offset. Let this new metric be called δGDOP. Its formula takes the form:

$$\delta\text{GDOP} = \sqrt{Trace[q_{rr}] + Trace[q_{vv}] + q_{\dot{\delta}_R \dot{\delta}_R}} \tag{5.24}$$

Eq. (5.24) only sums the diagonal elements of the Q matrix of Eq. (5.21) that correspond to position, velocity, and receiver clock offset rate when performing the $Trace$ operation. This metric is not impacted by the receiver clock offset accuracy. The full GDOP metric of Eq. (5.22) is related to TDOP and this new metric as follows:

$$\text{GDOP}^2 = \delta\text{GDOP}^2 + \text{TDOP}^2 \tag{5.25}$$

Later in this analysis, the utility of the new δGDOP metric will be demonstrated.

Although the coefficient matrix on the right-hand side of Eq. (5.19) is close to a typical DOP matrix, it has a number of issues. The issues involve the units in the equation. In a normal DOP analysis, the A_{DOP} matrix is unitless. As a corollary, the vectors on the extreme left-hand and right-hand sides of the equation have the same units. Issues with unit agreement are not a problem for typical DOP analyses that include only pseudorange measurements and position and receiver clock offset states. In order to solve the unit issues in Eq. (5.19), a number of re-scaling parameters are needed. Some are based on constellation geometry. Others are based on constellation motion. Yet others are based on relative measurement error standard deviations.

5.7.2 Re-Scaling Parameters

Three different dimensioned normalizing constants are used. They are related to the observables' measurement error standard deviations and to constellation geometry and motion. The first constant, developed in [42], is the maximum line-of-sight sweep rate of all the satellites in a constellation relative to a receiver on a non-rotating Earth:

$$\begin{aligned} \gamma = ||\dot{\hat{\rho}}||_{max} &= \left[\frac{1}{1-(R_E/a_{orb})}\right]\sqrt{\frac{\mu}{a_{orb}^3}} \\ &\approx 0.006(rad/s) \end{aligned} \tag{5.26}$$

where R_E is the radius of the Earth, a_{orb} is the average semi-major axis of the constellation (whose orbits are all assumed to be circular), and μ is the standard central gravitational parameter for the Earth. The representative value shown in Eq. (5.26) is for a typical LEO constellation. The next useful scaling constant is the maximum range acceleration of the

constellation satellites relative to a receiver on a non-rotating Earth, which is also developed in [42]:

$$\eta = |\ddot{\rho}|_{max} = \left[\frac{R_E/a_{orb}}{1-(R_E/a_{orb})}\right]\left[\frac{\mu}{a_{orb}^2}\right]$$
$$\approx 37(m/s^2) \tag{5.27}$$

under the assumption of circular orbits. The final constant used in the DOP analysis is a ratio of the accumulated delta range rate measurement error standard deviation to the pseudorange measurement error standard deviation:

$$\xi = \frac{\sigma_{\dot{A}DR}}{\sigma_{PR}} = \sqrt{\left[\frac{2\times 3.0440}{\delta\tau_{eml}(\pi T_{accum})^2}\right]\left[\frac{f_{chip}}{f_{carr}}\right]^2}$$
$$\approx \frac{0.01}{120}(1/s) \tag{5.28}$$

where $\delta\tau_{eml}$ is the early-minus-late spacing in PRN code chips of the DLL discriminator, and T_{accum} is the accumulation interval used for the carrier Doppler shift and the DLL discriminator. The carrier Doppler shift discriminator is assumed to use three frequencies, one at the nominal frequency estimate, one $0.5/T_{accum}$ Hz below it, and one $0.5/T_{accum}$ Hz above it. The term f_{carr} is the carrier frequency, and f_{chip} is the spreading code chipping rate. The 3.0440 factor in the numerator comes from the optimal frequency estimate discriminator for such accumulations. The ratio 0.01/120 corresponds to $T_{accum} = 0.325$ s, $\delta\tau_{eml} = 0.5$ chips, $f_{chip} = 41667$ Hz, $f_{carr} = 1626\times 10^6$ Hz, and an appropriate carrier-to-noise density ratio, which divides out of the ξ ratio. Equation (5.28) would include an additional factor of $\sqrt{B_{FLL}/B_{DLL}}$ if there were continuously available signals and corresponding tracking loops with a Frequency-Lock Loop (FLL) bandwidth of B_{FLL} Hz and a Delay-Lock Loop (DLL) bandwidth of B_{DLL} Hz. The ξ value indicated in the second line of Eq. (5.28) could be

representative of some new narrow band LEO signals with a much lower f_{chip} than a typical MEO GNSS signal. This simplistic analysis assumes that all signals are alike, which is consistent with the usual DOP assumption that each satellite has the same σ_{PR}.

The first two re-scaling parameters, γ and η, are based on constellation design, specifically the semi-major axis (or altitude) of the orbits. The final factor is based on the relative accuracies of the two types of measurements used. That is, ξ, relates the pseudorange and carrier Doppler shift measurement accuracies.

In the next two subsections, different combinations of these scaling parameters are used to create non-dimensional DOP matrices. There are two major categories of the resulting matrices. The first is a pseudorange-based system that uses these three parameters in order to convert the carrier Doppler shift measurements and velocity and receiver clock offset rate states to units of meters. The second is a carrier-Doppler-shift-based system where the pseudorange measurements along with the position and receiver clock offset unknowns are converted to units of meters per second using the three parameters. The details of these analyses and their impacts on the DOP analysis are discussed in subsequent sections.

The terms pseudorange-based and carrier-Doppler-shift-based are defined here to differentiate between cases that convert the vector of estimated quantities to units of meters and meters per second, respectively. The pseudorange-based cases assume that pseudorange is the dominant measurement. This would be the case in systems with four or more accurate pseudorange measurements such as traditional GPS. Such a case is of reduced interest in the present work because a simple pseudorange-only DOP analysis could be used in this situation. Thus, the pseudorange-based cases are shown for completeness.

When converting from the dimensionless DOP metric to the predicted accuracy of an estimated quantity, the measurement error standard deviation of the dominant measurement

type must be used. In a carrier-Doppler-shift-based system, the DOP metrics are multiplied by $\lambda\sigma_{Dopp}$. It may seem odd to use the carrier Doppler shift measurement error uncertainty to predict the receiver clock offset accuracy when it is only weakly observable using carrier Doppler shift measurements. This is a valid concern, but in some carrier-Doppler-shift-based cases, $\lambda\sigma_{Dopp}$ is divided by ξ when predicting the accuracy of a given estimated quantity. This type of calculation results in multiplying the DOP metric by σ_{PR}, the pseudorange measurement error uncertainty. This makes sense because pseudorange should be the dominant measurement for the receiver clock offset unknown.

5.7.3 Pseudorange-Based Combined DOP

Pseudorange-based analyses are characterized by the conversion of the units of the carrier Doppler shift measurements, the velocity states, and the receiver clock offset rate state to units of meters. The pseudorange measurement error standard deviation is the controlling measurement accuracy parameter that is used to convert the resulting DOP value to the approximate accuracy of the different states. One combination of scaling parameters yields the following re-scaled version of Eq. (5.19) into a pseudorange-based DOP analysis:

$$\begin{bmatrix} \Delta\rho^1 \\ \vdots \\ \Delta\rho^M \\ -\lambda\Delta D^{M+1}(\frac{1}{\xi}) \\ \vdots \\ -\lambda\Delta D^{M+N}(\frac{1}{\xi}) \end{bmatrix} = \underbrace{\begin{bmatrix} (\hat{\rho}^1)^T & 1 & 0 & 0 \\ \vdots & \vdots & \vdots & \vdots \\ (\hat{\rho}^M)^T & 1 & 0 & 0 \\ (\frac{1}{\xi})(\dot{\hat{\rho}}^{M+1})^T & [(\hat{\rho}^{M+1})^T\dot{\vec{v}}^{M+1} + (\dot{\hat{\rho}}^{M+1})^T\vec{v}^{M+1}]/(\xi c) & (\hat{\rho}^{M+1})^T & 1 \\ \vdots & \vdots & \vdots & \vdots \\ (\frac{1}{\xi})(\dot{\hat{\rho}}^{M+N})^T & [(\hat{\rho}^{M+N})^T\dot{\vec{v}}^{M+N} + (\dot{\hat{\rho}}^{M+N})^T\vec{v}^{M+N}]/(\xi c) & (\hat{\rho}^{M+N})^T & 1 \end{bmatrix}}_{A_{DOP}} \begin{bmatrix} \Delta\vec{r} \\ c\Delta\delta_R \\ (\frac{1}{\xi})\Delta\vec{v} \\ (\frac{c}{\xi})\Delta\dot{\delta}_R \end{bmatrix} \quad (5.29)$$

In Eq. (5.29), ξ is the only re-scaling parameter that has been used. It has been used on the carrier Doppler shift measurement errors to convert their units to meters like the

pseudorange measurement errors. As in standard pseudorange navigation DOP analysis, the receiver clock offset error has been multiplied by c in order to convert it into range-equivalent units. The velocity errors have been multiplied by the reciprocal of ξ in order to convert them into equivalent units of meters. The receiver clock offset rate error has been multiplied by c in order to convert it into range-rate-equivalent units and then divided by ξ in order to convert the result into length units. The resulting non-dimensional A_{DOP} coefficient matrix on the right-hand side of Eq. (5.29) is one option for a pseudorange-based DOP analysis. The A_{DOP} matrix can be used in its Eq. (5.29) form with the calculation of Eqs. (5.22), (5.23), and (5.24) in order to compute the associated non-dimensional DOP metrics for this version of the analysis. The associated dimensional precision metrics are shown in Table 5.5.

Table 5.5: Navigation Precision from Pseudorange-Based DOP Option 1

Estimated Quantity	Dimensional Precision Metric
$\vec{r}$	GDOP(σ_{PR})
δ_R	GDOP(σ_{PR}/c)
$\vec{v}$	GDOP($\xi\sigma_{PR}$)
$\dot{\delta}_R$	GDOP($\xi\sigma_{PR}/c$)

The scaling parameters other than σ_{PR} found within the parentheses in the second column of Table 5.5 are the reciprocals of the scaling parameters that appear in the vector on the right-hand side of Eq. (5.29). Table 5.5 shows how one would determine the estimated dimensional PNT accuracy from the corresponding non-dimensional GDOP analysis. When using the table with a mix of DOP metrics, the GDOP value should be replaced by the appropriate DOP metric. For instance, in the second row, the TDOP value should be used in place of the GDOP value when breaking up the system into two different metrics, and the other three rows should use the δGDOP value.

There are a large number of possible pseudorange-based DOP analyses that can be developed

with the described normalizing constants. Only one is shown here. More examples can be found in [30]. For systems with four or more accurate pseudorange measurements, a combined solution with Doppler shift may be unnecessary. For systems with fewer than four pseudorange measurements or with inaccurate pseudorange measurements, example calculations have shown that a Doppler-shift-based DOP analysis produces results that agree better with the batch filter results than pseudorange-based analyses. Thus, the pseudorange-based DOP analyses are shown here only for completeness.

5.7.4 Carrier-Doppler-Shift-Based Combined DOP

All of the carrier-Doppler-shift-based DOP analyses convert the units of the pseudorange measurement to meters per second and the units of the position error and the range-equivalent receiver clock offset error to meters per second. One potential normalized DOP model based on carrier Doppler shift measurements is:

$$\begin{bmatrix} \xi\Delta\rho^1 \\ \vdots \\ \xi\Delta\rho^M \\ -\lambda\Delta D^{M+1} \\ \vdots \\ -\lambda\Delta D^{M+N} \end{bmatrix} = \underbrace{\begin{bmatrix} \frac{\xi}{\gamma}(\hat{\rho}^1)^T & \frac{\xi c}{\eta} & 0 & 0 \\ \vdots & \vdots & \vdots & \vdots \\ \frac{\xi}{\gamma}(\hat{\rho}^M)^T & \frac{\xi c}{\eta} & 0 & 0 \\ (\frac{1}{\gamma})(\dot{\hat{\rho}}^{M+1})^T & [(\hat{\rho}^{M+1})^T\dot{\vec{v}}^{M+1} + (\dot{\hat{\rho}}^{M+1})^T\vec{v}^{M+1}]/\eta & (\hat{\rho}^{M+1})^T & 1 \\ \vdots & \vdots & \vdots & \vdots \\ (\frac{1}{\gamma})(\dot{\hat{\rho}}^{M+N})^T & [(\hat{\rho}^{M+N})^T\dot{\vec{v}}^{M+N} + (\dot{\hat{\rho}}^{M+N})^T\vec{v}^{M+N}]/\eta & (\hat{\rho}^{M+N})^T & 1 \end{bmatrix}}_{A_{DOP}} \begin{bmatrix} \gamma\Delta\vec{r} \\ \eta\Delta\delta_R \\ \Delta\vec{v} \\ c\Delta\dot{\delta}_R \end{bmatrix} \quad (5.30)$$

In [42], the carrier-Doppler-shift-only system is shown to produce accurate position and velocity solutions, but it has only weak observability of the receiver clock offset. The addition of pseudorange measurements, even inaccurate ones, can significantly improve the clock accuracy of the carrier-Doppler-shift-only solution. This idea has guided the selection of the

scaling parameters in Eq. (5.30). The last N equations and the corresponding last N rows of the A_{DOP} coefficient matrix are identical to the equations and coefficient matrix that are analyzed in [42]. Given the success of the work in [42] for a carrier-Doppler-only navigation system, an analysis like that in Eq. (5.30) seems reasonable for a navigation system that relies primarily on carrier Doppler shift data while including a few pseudorange measurements in hopes of improving the receiver clock offset accuracy. Given the choice to make the last N rows like those of the analysis in [42] and given the need to change the dimensions of the pseudorange measurement errors into meters/sec units, the re-normalization of Eq. (5.30) follows. Even if only one pseudorange measurement is available, the DOP model in Eq. (5.30) implies that the batch filter will use it to determine the receiver clock offset. This DOP analysis also has good agreement with the covariance matrix from the batch filter, with matrix elements within 10^{-4} of the largest entry. The associated dimensional precision metrics for Eq. (5.30) using the δGDOP and TDOP metrics are shown in Table 5.6.

Table 5.6: Navigation Precision from Carrier-Doppler-Shift-Based DOP

Estimated Quantity	Dimensional Precision Metric
$\vec{r}$	$\delta\text{GDOP}(\lambda\sigma_{Dopp}/\gamma)$
δ_R	$\text{TDOP}(\lambda\sigma_{Dopp}/\eta)$
$\vec{v}$	$\delta\text{GDOP}(\lambda\sigma_{Dopp})$
$\dot{\delta}_R$	$\delta\text{GDOP}(\lambda\sigma_{Dopp}/c)$

A second option for a carrier-Doppler-shift-based DOP analysis model is:

$$\begin{bmatrix} \xi\Delta\rho^1 \\ \vdots \\ \xi\Delta\rho^M \\ -\lambda\Delta D^{M+1} \\ \vdots \\ -\lambda\Delta D^{M+N} \end{bmatrix} = \underbrace{\begin{bmatrix} \frac{\xi}{\gamma}(\hat{\rho}^1)^T & 1 & 0 & 0 \\ \vdots & \vdots & \vdots & \vdots \\ \frac{\xi}{\gamma}(\hat{\rho}^M)^T & 1 & 0 & 0 \\ (\frac{1}{\gamma})(\dot{\hat{\rho}}^{M+1})^T & [(\hat{\rho}^{M+1})^T\dot{\vec{v}}^{M+1} + (\dot{\hat{\rho}}^{M+1})^T\vec{v}^{M+1}]/(\xi c) & (\hat{\rho}^{M+1})^T & 1 \\ \vdots & \vdots & \vdots & \vdots \\ (\frac{1}{\gamma})(\dot{\hat{\rho}}^{M+N})^T & [(\hat{\rho}^{M+N})^T\dot{\vec{v}}^{M+N} + (\dot{\hat{\rho}}^{M+N})^T\vec{v}^{M+N}]/(\xi c) & (\hat{\rho}^{M+N})^T & 1 \end{bmatrix}}_{A_{DOP}} \begin{bmatrix} \gamma\Delta\vec{r} \\ (\xi c)\Delta\delta_R \\ \Delta\vec{v} \\ c\Delta\dot{\delta}_R \end{bmatrix} \quad (5.31)$$

where the speed of light has been factored out of the second column in the A_{DOP} matrix and moved to the receiver clock offset error element in the vector on the right-hand side. The associated dimensional precision metrics for Eq. (5.31) using the δGDOP and TDOP metrics are given in Table 5.7.

Table 5.7: Navigation Precision from Carrier-Doppler-Shift-Based GDOP

Estimated Quantity	Dimensional Precision Metric
$\vec{r}$	$\delta\text{GDOP}(\lambda\sigma_{Dopp}/\gamma)$
δ_R	$\text{TDOP}(\lambda\sigma_{Dopp}/(\xi c)$
$\vec{v}$	$\delta\text{GDOP}(\lambda\sigma_{Dopp})$
$\dot{\delta}_R$	$\delta\text{GDOP}(\lambda\sigma_{Dopp}/c)$

The different options for calculating the A_{DOP} matrix listed here are only a few examples of how to use the normalizing factors to calculate the A_{DOP} matrix. More examples are derived in [30]. The DOP analysis in Eq. (5.30) is shown due to its success in [42]. The DOP analysis in Eq. (5.31) is shown because it is found to be the best analysis. Further discussion of the results is shown in future sections.

5.7.5 Validation of DOP Analysis Using Batch Filter Covariance

In order to verify the correctness of each of the DOP analysis options, a comparison to the covariance of the batch filter has been made. This validation ensures that the scaling of each of the columns of the A_{DOP} matrix in the DOP analysis are consistent with the batch filter. Through the use of a scaling matrix, S, the batch filter covariance matrix can be non-dimensionalized based on the scaling parameters used in the corresponding DOP analysis. The comparison between the batch filter and DOP results is:

$$Q = (A_{DOP}^T A_{DOP})^{-1} \stackrel{?}{=} \frac{1}{\sigma_{DOM}^2} S P_{xx} S \tag{5.32}$$

where P_{xx} is the measurement error covariance matrix found using Eq. (5.17) from the filter where σ_{DOM} is the error standard deviation associated with the dominant measurement of the particular DOP analysis – either σ_{PR} or $\lambda\sigma_{Dopp}$, and where the S matrix is the re-scaling matrix that, when multiplied by the vector error of the batch filter estimate x of Eq. (5.14), yields the re-scaled estimation error vector on the right-hand side of the corresponding DOP analysis equation. As an example, the S matrix associated with the pseudorange-dominant DOP error model in Eq. (5.29) is

$$S = \begin{bmatrix} I_3 & 0 & 0 & 0 \\ 0 & 1 & 0 & 0 \\ 0 & 0 & \frac{1}{\xi} I_3 & 0 \\ 0 & 0 & 0 & \frac{1}{\xi} \end{bmatrix} \tag{5.33}$$

where I_3 is a 3×3 identity matrix. The S matrices and the $1/\sigma^2_{DOM}$ factor non-dimensionalize the P_{xx} matrix so that the units match the Q matrix in the equation.

For all types of DOP analysis considered in this work, good agreement has been obtained between the non-dimensional Q matrix of the DOP analysis on the left-hand side of Eq. (5.32) and the corresponding non-dimensionalized version of the batch covariance matrix on the right-hand side to within 4 significant digits or better. This fact indicates that the DOP analyses are all founded on reasonable assumptions about accuracy models of the basic pseudorange/Doppler-shift point solution navigation system that constitutes this paper's subject of investigation.

5.7.6 Accuracy Prediction Capabilities of Scalar DOP Metrics

After verifying the mathematical correctness of each DOP analysis possibility, another important question must be asked: Which one or ones produce scalar metrics that characterize the accuracy of all or most of the batch filter's unknowns? When comparing the results from different DOP options with the batch filter Monte Carlo simulation study errors listed in Tables 5.2 - 5.4, some GDOP analyses produce results that do not agree with the batch filter error results. The difference in results is due to scaling issues in different elements. The relative scaling varies depending on the number of pseudorange and carrier Doppler shift measurements. Therefore, a single GDOP analysis option that produces filter accuracy predictions that agree with the batch filter results was not found in [30].

In the present work, a number of methods have been tried in order to find a DOP analysis that works for all cases. One method has been to test different combinations of scaling factors over many different scenarios that involved varying numbers and accuracies of pseudorange and carrier Doppler shift measurements. Various combinations of scale factors were tried in attempts to force the magnitudes of the columns of the resulting non-dimensional A_{DOP} matrix to be near one. Another method of seeking good re-scaling parameters involved using QR factorization of a portion of the A_{DOP} matrix in order to separate the carrier Doppler shift effects on velocity and clock offset rate observability from their effects on position and clock offset observability. The QR factorization allowed for a more traditional GDOP analysis of the position and clock offset terms using the pseudorange measurements and using the information about position and clock offset that is provided by the carrier Doppler shift measurements. Neither of the two methods yielded a single DOP metric that could predict the accuracy of all of the unknowns of the batch filter in all cases.

A method that works for all cases is to give up on the question for a single useful GDOP

metric. Instead, one must split the GDOP metric into the two separate metrics of TDOP and δGDOP. The first metric characterizes the predicted accuracy of the receiver clock offset, and the second metric characterizes the predicted accuracy of the position, the velocity, and the receiver clock offset rate. When comparing the results of different DOP analyses with the batch filter using the two separate metrics, all of the tested Doppler-based DOP analyses produce accuracy predictions that agree with the batch filter simulation-based results. Although all Doppler-shift-based DOP analyses yield predictions that agree with the batch filter after scaling, the magnitude of the resulting TDOP and δGDOP values vary. The two different metrics are needed for the following reason: When inaccurate pseudorange measurements are included with carrier Doppler shift, two separate subsets of the estimated unknowns are created because the pseudorange measurements only significantly aid the clock offset terms, and the clock offset is only weakly observable in a Doppler-only system. One subset consists of the position, velocity, and clock rate estimates, and the other subset consists of the clock offset. Attempting to combine the errors of these two different subsets in a single GDOP metric leads to disagreements in the predicted accuracy of the estimated quantities between the GDOP analysis and the batch filter. Thus, splitting the DOP analysis into two separate metrics resulted in an agreement between the DOP analysis and the batch filter's errors and covariance matrix.

5.7.7 Combined DOP Representative Results

This section presents the δGDOP and TDOP plots for a number of different constellations. The $1-\sigma$ measurement error standard deviation for the pseudorange measurements is assumed to be $\sigma_{PR} = 120$ m, and $\lambda\sigma_{Dopp} = 0.01$ m/s is assumed to be the range-rate-equivalent carrier Doppler shift measurement error standard deviation. For this analysis, it is assumed that every visible satellite above a 7.5^o elevation mask yields a pseudorange and a carrier

Doppler shift measurement unless otherwise noted. For more plots using other DOP analyses see [30].

Figure 5.2 shows the δGDOP and TDOP maps for the Kuiper constellation. The particular DOP analysis is based on Eqs. (5.21), (5.23), (5.24), and (5.31). Thus, it is a Doppler-dominated DOP analysis. Note that the latitude bounds of the considered region are -50^o to 50^o. Outside of these bounds, the visibility of satellites is low due to the maximum inclination of the Kuiper constellation. The values for the two DOP metrics are both no greater than four over the entire region of consideration, which indicates low potential navigation error. The inclination of the Kuiper constellation creates a good diversity of the rates of change of the line-of-sight vectors between the satellites and the receiver, which results in an accurate navigation solution similar to the OneWeb constellation with alternating ascending and descending nodes, as analyzed in [42] and [30].

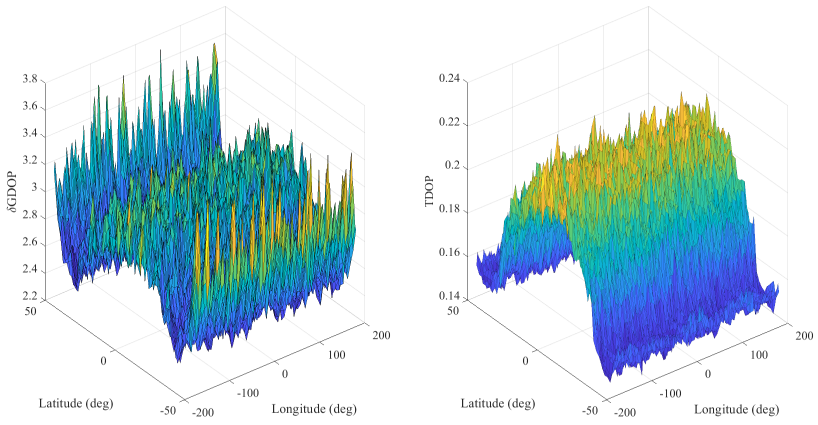

Figure 5.2: Carrier-Doppler-Shift-based Option 2 DOP results for the Kuiper constellation with every visible satellite producing pseudorange and carrier Doppler shift measurements.

Figure 5.3 shows the δGDOP and TDOP maps for the Kuiper constellation found using Eqs. (5.21), (5.23), (5.24), and (5.30). This is the alternate Doppler-dominated DOP analysis scaling that has been discussed above. Note that the δGDOP plot is the same as in Fig. 5.2.

The similarity is due to the columns associated with position, velocity, and clock rate being the same between Eqs. (5.31) and (5.30). On the other hand, the TDOP map values are different because of the changes in the column associated with the clock offset in Eqs. (5.31) and (5.30). Although the magnitudes are different, the shape of each of the two TDOP plots has the same shape. The same shape results in the predicted accuracies of each system being nearly identical after proper scaling. The analysis associated with Eq. (5.31) is used in the remainder of this paper because its TDOP values are near one when pseudorange measurements are available and it is consistent with the classical pseudorange-based GDOP analysis for a DOP value near one to indicate an accurate navigation solution.

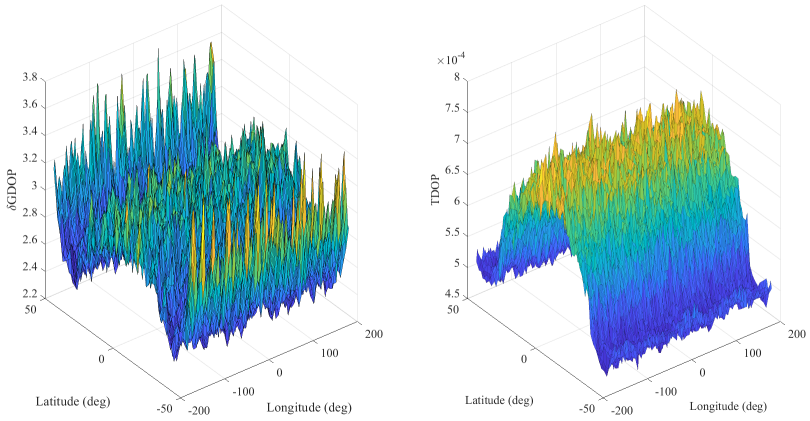

Figure 5.3: Carrier-Doppler-Shift-based Option 1 DOP results for the Kuiper constellation with every visible satellite producing pseudorange and carrier Doppler shift measurements.

Figure 5.4 shows the two DOP maps for a Starlink constellation with none of the satellites producing pseudorange measurements even though the assumption of the possibility of pseudorange measurements is implied in the use of the ξ rescaling parameter because its definition requires a pseudorange measurement error standard deviation. Notice how the scale of the TDOP plot is orders of magnitude larger than the TDOP plot of Figure 5.2. The results imply that even noisy pseudorange measurements might significantly reduce the receiver clock error compared to a carrier-Doppler-shift-only solution. In the left-hand panel

of Fig. 5.4, the δGDOP values are low, which indicates that position, velocity, and clock offset rate are accurate due to the large number of carrier Doppler shift measurements. A large difference in magnitude between the diagonal elements of the Q matrix is one of the scenarios in which a single GDOP metric may produce results that do not agree with a batch filter, in this case because the TDOP magnitudes would dominate the magnitudes from the other states when performing the $Trace$ operation to make GDOP large even though δGDOP is not large.

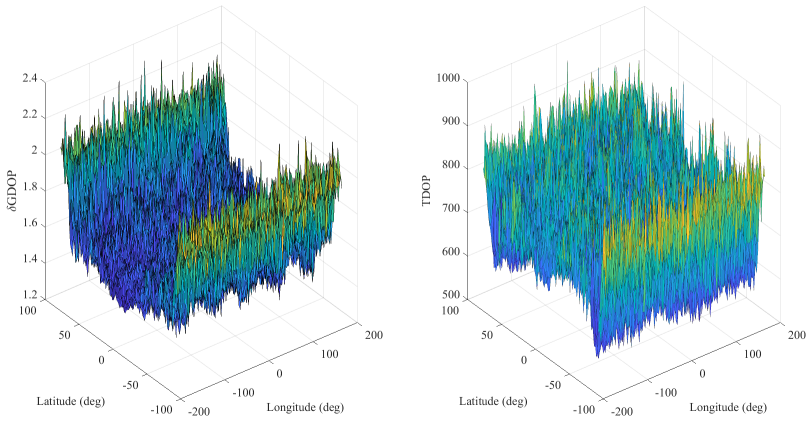

Figure 5.4: Carrier-Doppler-Shift-based Option 2 DOP results for the Starlink constellation with no satellites producing pseudorange measurements and all visible satellites producing carrier Doppler shift measurements.

For the sake of brevity, this paper does not show results for every possible form of DOP analysis. That said, extensive studies have demonstrated that it is possible to produce DOP maps for every constellation with any number of pseudorange and carrier Doppler shift measurements. By using two separate DOP metrics and a carrier-Doppler-shift-based analysis, the results all agree well with the errors from a batch filter analysis. This is not the case when using only the single metric GDOP. As discussed in [30], some DOP analyses' single GDOP metric results agree with the batch filter in certain cases but not others.

5.8 Example Constellation Design

The DOP analysis can be used for basic constellation design. The simplicity of the DOP analysis allows for the rapid generation of results. Thus, the impacts of changes in constellation design can be quickly calculated without the need for costly simulations and batch filter solutions. The DOP maps versus latitude and longitude in the previous section are useful as snapshots in time. In order to perform constellation design, however, the impacts of time variations of the constellation's relative geometry need to be considered. This section uses plots of the maximum and minimum values of the two DOP metrics over latitude or longitude and an entire orbital period of an individual constellation element as a means of evaluating potential system accuracy. These plots are more indicative of overall constellation navigation performance than a single snapshot in time.

The design analysis and plots in this section use the OneWeb constellation as an example. One of the key features analyzed is the benefit of alternating ascending and descending nodes. The increase in the diversity of the rate of change of the line-of-sight vectors between the receiver and satellite caused by alternating ascending and descending nodes of this polar-orbiting constellation's orbit planes has been shown to improve Doppler-only navigation performance significantly [42]. Another major constellation design aspect that is considered is the number of satellites that produce pseudorange measurements per orbital plane. The analysis assumes that all visible satellites broadcast signals that can be used to measure carrier Doppler shift.

The constellation designs that have been considered allow a subset of the satellites in each plane to broadcast pseudorange-capable signals. These satellites are assumed to be distributed evenly throughout the plane. Additionally, adjacent planes are assumed to have pseudorange-capable satellites that are offset in their arguments of latitude relative to those

of a given plane. If five satellites per plane are chosen to produce pseudorange measurements, then in order to achieve an even spacing within the plane each pseudorange-capable satellite is separated by $40/5 = 8$ satellite slots within its orbital plane. With this setup, adjacent planes' pseudorange-capable satellites are offset by $8/2 = 4$ satellites, or half the in-plane spacing. Other formulas for the argument of latitude offset between planes have been tested, but the in-plane spacing and adjacent plane offset formulas above produced the best results even for the alternating ascending node case. Figure 5.5 helps to visualize the scenario with five pseudorange-capable satellites per plane. Black circles in the figure represent pseudorange-capable satellites. Red circles indicate satellites not capable of producing pseudorange measurements. The red and yellow lines indicate orbital planes with satellites traveling in opposite directions, indicated by the black arrows. Only three of the OneWeb orbital planes are shown for simplicity, but the pattern repeats for all orbital planes.

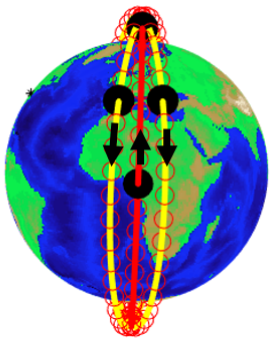

Figure 5.5: Three orbital planes of the OneWeb constellation. Black circles indicate pseudorange-capable satellites. The red and yellow lines indicate orbital planes with satellites traveling in different directions, indicated by the black arrows. Empty red circles indicate satellites in the constellation that are not capable of producing pseudorange measurements.

Figure 5.6 plots the maximum and minimum values of the two DOP metrics over latitude and over the entire orbital period versus longitude for the OneWeb constellation with grouped ascending nodes and two satellites per plane that can return pseudorange measurements. In both plots, the dips at two longitudes are due to the seams in the constellation between the

groups of ascending nodes and descending nodes. At these seams, a user receiver can see both north-going and south-going satellites, which greatly improves the observability of the batch filter solution. These dips agree with Figure 5 from [42] but are narrower due to the Earth's rotation over the orbital period. Similar improvements to navigation accuracy evident at seams of polar constellations are observed in Figure 9 of [22]. The addition of pseudorange measurements provides little benefit to the maximum possible values of the δGDOP metric in the figure's left-hand plot. The TDOP plot does not indicate a change in the maximum values either, but the minimum values are much better than for a Doppler-only solution. The maximum clock offset TDOP metric is not changed because there are times over the orbital period when no pseudorange measurements are available at every location due to the low number of pseudorange-capable satellites.

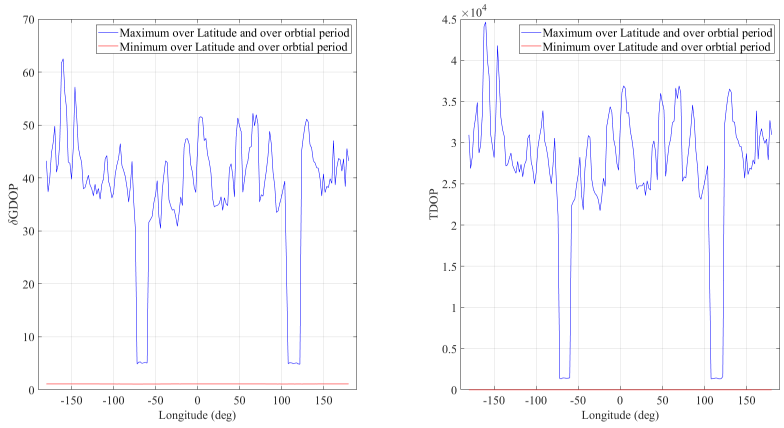

Figure 5.6: Carrier-Doppler-Shift-based Option 2 DOP results for the OneWeb constellation with grouped ascending nodes and with two satellites per plane producing pseudorange measurements and all visible satellites that produce carrier Doppler shift measurements. Maximum and minimum values are taken over latitude and over the entire orbital period.

Figure 5.7 shows the maximum and minimum numbers of visible satellites versus longitude and latitude for the constellation whose δGDOP and TDOP values have been plotted in Fig. 5.6. The maxima and minima are taken over latitude (left-hand panel) or longitude

(right-hand panel) and over orbital period. OneWeb constellation designs with different characteristics may change the plots in Fig. 5.7 slightly, but both plots are a good indication for the number of satellites visible for all cases. Note that the visible number of satellites corresponds to the number of carrier Doppler shift measurements, but not the number of pseudorange measurements. Furthermore, the number of visible satellites is significantly higher than can be expected for the OneWeb constellation when using solely main-lobe downlink signals from the phased array antennas on the OneWeb satellites. Recall that a 7.5^o elevation mask is used to determine whether a satellite is visible or not. The low elevation mask is more in line with using wide beam antennas for telemetry, tracking, and control purposes. As will be shown below, the DOP accuracy predictions for a well-designed OneWeb constellation tend to be better (i.e., produce lower DOP values) near the Earth's poles than near the Earth's equator. This fact and the latitude-dependent visible satellite counts in the right-hand panel of Fig. 5.7 imply that the number of carrier Doppler shift measurements still impacts the DOP and navigation accuracy in a combined pseudorange and carrier Doppler shift system when the number of the pseudorange measurements is low and the pseudorange measurements are inaccurate.

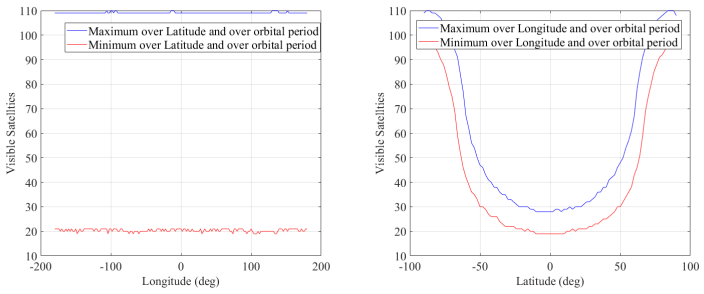

Figure 5.7: Number of visible satellites from the OneWeb constellation with grouped ascending nodes. Maximum and minimum values are taken over latitude and the entire orbital period for the left plot. For the right plot, the maximum and minimum values are taken over longitude and the entire orbital period.

Figure 5.8 depicts the maximum and minimum DOP metrics over latitude and the entire

orbital period versus longitude for a OneWeb constellation with alternating ascending and descending nodes and two satellites per plane producing pseudorange measurements. As opposed to Fig. 5.6, the dips in the maxima of the DOP metrics are not seen. Instead, the maximum values in Fig. 5.8 are all roughly at the magnitudes of the dips in Fig. 5.6. This agrees with the results from [42], when using alternating ascending and descending nodes. In Fig. 5.8, the δGDOP values are low, which indicates that the position, velocity, and clock offset rate errors are low. On the other hand, the maximum TDOP values are large while the minima are low. This fact indicates that there are times when pseudorange measurements are not available. This result indicates that the maximum values of TDOP might be reduced significantly if more pseudorange-capable satellites per plane were added.

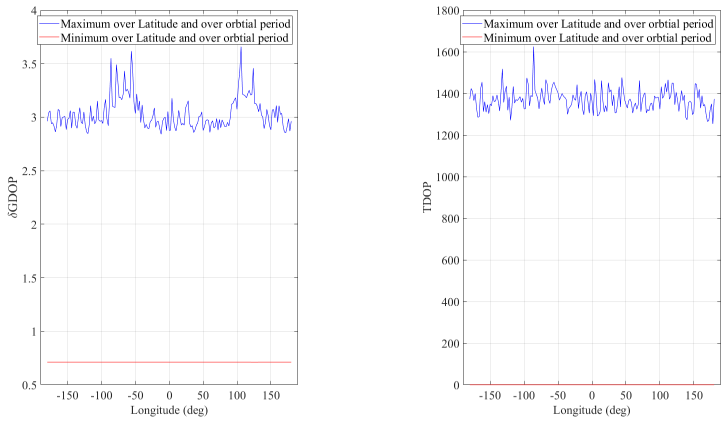

Figure 5.8: Carrier-Doppler-Shift-based Option 2 DOP results for the OneWeb constellation with alternating ascending and descending nodes and with two satellites per plane producing pseudorange measurements and all visible satellites producing carrier Doppler shift measurements. Maximum and minimum values are taken over latitude and the entire orbital period.

Figure 5.9 depicts the maximum and minimum DOP metrics over longitude and the entire orbital period versus latitude for a OneWeb constellation with alternating ascending and descending nodes and with five satellites per plane that broadcast pseudorange-capable signals. In both plots, the maximum and minimum values are much closer together in magnitude, and

the TDOP maximum values have been reduced by about three orders of magnitude relative to the results in Fig. 5.8. This good result is caused by the fact that pseudorange measurements are available everywhere for the entire orbital period. Five pseudorange-capable satellites per plane is the minimum number to show close agreement between the minimum and maximum TDOP metrics. With fewer than five pseudorange-capable satellites per plane, the maximum values in the TDOP plot spike to much higher values.

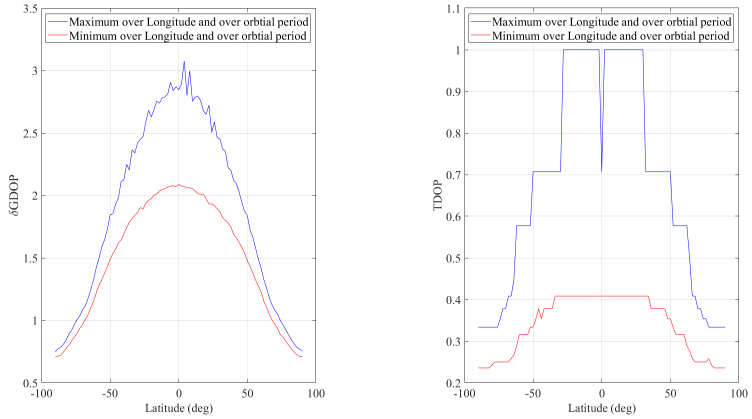

Figure 5.9: Carrier-Doppler-Shift-based Option 2 DOP results for the OneWeb constellation with alternating ascending and descending nodes and with five satellites per plane producing pseudorange measurements and all visible satellites producing carrier Doppler shift measurements. Maximum and minimum values are taken over longitude and the entire orbital period.

From this analysis, it is clear that, in order for the OneWeb constellation to have the best potential position, clock offset, velocity, and clock offset rate navigation potential, it is best to have alternating ascending and descending nodes and to have a minimum of five pseudorange capable satellites per plane. These results are only valid under the specific assumptions used in this analysis. Although the results may change under different assumptions, the OneWeb constellation design analysis above is an example of how the DOP metrics can be used for rapid constellation design for navigation systems. The DOP equations developed above can be used for any navigation system that has satellites that broadcast signals that enable a

mix of pseudorange and carrier Doppler shift measurements.

In this section, the constellation design process used a brute-force method. The simplicity of the implementation of the DOP analysis allows for the use of brute-force methods, but the formula for the A_{DOP} matrix can also be used to identify constellation characteristics that impact navigation accuracy. For example, the bottom half of the first column of the large A_{DOP} matrix on the right-hand side of Eq. (5.31) includes $\dot{\hat{\rho}}$ terms. These quantities are defined as the time rates of change of the unit direction vectors that point from the satellite and the receiver. Increasing the diversity of the time rates of change of the line of sight vectors between the satellites and the receiver increases the diversity of the $\dot{\hat{\rho}}$ terms which would result in an improvement in navigation accuracy. This is confirmed in the results when using alternating ascending and descending nodes for the OneWeb constellation. Similar arguments can be made for each of the columns in the A_{DOP} matrix.

5.9 Summary and Conclusions

This paper has developed a DOP analysis that predicts the accuracy of the position, clock offset, velocity, and clock offset rate of a combined pseudorange and carrier Doppler shift navigation system that uses data from LEO satellites in a point-solution batch filter. The DOP analysis uses problem scaling parameters in order to non-dimensionalize the coefficient matrix in a linearized relationship between measurement errors and filter estimation errors. An important new scaling parameter has been introduced to facilitate the required non-dimensionalization: the ratio of the error standard deviation of the range-rate-equivalent carrier Doppler shifts to the standard deviation of the pseudoranges. It is given in 1/sec units. With the addition of pseudorange measurements to the carrier Doppler shift measurements of a previous study, two separate subsets of filter unknowns are created in practice. Thus,

instead of a single GDOP metric, two separate DOP metrics are needed. One characterizes the accuracy of the position, velocity, and clock offset rate estimates. The other characterizes the accuracy of only the clock offset. The DOP metrics have been checked by comparing their accuracy predictions with the accuracy that has been achieved by a combined pseudorange and carrier Doppler shift point-solution batch filter operating on simulated data. Using the DOP metrics, a number of LEO constellations' potential navigation accuracies have analyzed. Additionally, an example of how to use the DOP analysis for constellation design is shown using the OneWeb constellation.

Representative results are shown in the form of DOP maps versus latitude and longitude for both metrics and a few LEO constellations. The addition of a few pseudorange measurements to a Doppler-based navigation system, even inaccurate ones, can significantly increase the accuracy of the receiver clock offset estimate even when there are not enough highly accurate pseudoranges to have a significant impact on the position, velocity, and clock offset rate accuracy. This is caused by the fact that the clock accuracy is only weakly observable in a carrier-Doppler-shift-only navigation solution.

The constellation design portion of this work considers plots of the two DOP metrics' maximum and minimum values over latitude or longitude and time. These plots characterize DOP metric maxima and minima over an entire orbital period. The DOP-based constellation design analysis indicates that, for the OneWeb constellation, alternating ascending and descending nodes and five pseudorange-producing satellites per plane produces the best results with the fewest number of pseudorange-capable satellites possible. This result illustrates how the DOP analyses developed here enable the rapid determination of the navigation potential of a system.

Chapter 6

Conclusions

This dissertation demonstrated the feasibility of GNSS-like navigation using an INS and carrier Doppler shift measurements from LEO communication constellations to provide an alternative or backup to GNSS. The large number of LEO satellites and their high overhead velocities allow for a position solution using only carrier Doppler shift measurements. It is assumed that the simulated LEO constellations do not have omnidirectional beacons. Therefore, only one or two signals are available at any given location and time. The low number of visible signals makes a point-solution batch filter, similar to the typical GNSS position solution, impossible. Instead, an SRIF-form of an EKF is used to determine the navigation accuracy using data generated from a truth-model simulation of an aircraft flying over Blacksburg, Virginia. The EKF combines carrier Doppler shift measurements and accelerations and angular rate measurements from an INS to provide a navigation solution with fewer than eight simultaneous visible signals.

The feasibility of such a system and the effects of constellation design parameters on navigation accuracy are analyzed in the first manuscript. One method to lower navigation error is to increase the diversity of the rate of change of the line-of-sight vectors between the satellites and the receiver. To increase this diversity for polar constellations, the ascending and descending nodes can be alternated. Other methods to improve navigation accuracy include increasing INS quality, increasing signal availability, and steering satellite spot beams so that a diverse set of satellites provide measurements to a single point on the Earth. The

first manuscript uses constellations with parameters ranging from 66 satellites in six orbital planes (Iridium) to 1600 satellites in 32 orbital planes (Starlink). The OneWeb and Iridium constellation have polar orbits while the Starlink and Kuiper constellations are inclined. The altitudes of the investigated constellations range from 590 km to 1200 km. Under this work's assumptions each polar constellation provides one or two signals at any given time while the inclined constellations provide only one. Using two constellations, the results show that a steady-state navigation filter position accuracy around one meter is possible except when using exclusively polar constellations, where the steady-state position accuracy is around seven meters. The steady-state timing accuracy for the same system is around 0.5 ms.

The second manuscript discusses the methods for implementing a tightly-coupled INS/radio-navigation Kalman filter. Specifically, it analyzes the different methods of including INS data into the filter from the first manuscript. The most popular method for incorporating INS data, model replacement, is found to produce the same accuracy as other methods using Gauss-Markov models. It is unclear why model replacement is the most popular. In model replacement, the INS measurements are directly integrated, similar to dead-reckoning. It is conjectured that model replacement is the most popular option to incorporate INS measurements because some of the researchers who developed INS/radio-navigation filters initially worked on dead-reckoning navigation systems with only an INS. Methods other than model replacement produce navigation results with comparable accuracy. Some methods other than model replacement use Gauss-Markov models which require extra filter states and model parameter tuning to produce the best results. These methods require more initial tuning, but are implemented in a more traditional manner than model replacement from a Kalman filtering standpoint: the inclusion of the INS data via filter measurement updates. The Gauss-Markov model methods allow for alternate methods of incorporating multiple independent INS measurements. The results show little difference in navigation performance

between the different filter implementation architectures. The second manuscript shows that the method for the inclusion of INS measurements in a KF can be chosen based on the preferences of the user and system specifications.

The third manuscript describes a DOP analysis of a system using noisy pseudorange measurements and carrier Doppler shift measurements in a batch filter point solution that is a generalization of the Doppler-only batch filter of [42]. In the first two manuscripts and other previous works, using only carrier Doppler shift to navigate results in poor receiver clock accuracy. This manuscript demonstrates that the addition of noisy pseudorange measurements increases the estimated receiver clock accuracy by multiple orders of magnitude when operating in a batch-filter mode with a sufficient number of available satellite signals. The clock accuracy with noisy pseudorange measurements is around 0.001 ms. The DOP analysis provides a method to quickly determine the approximate accuracies of the solution components by using simplified models of pseudorange and carrier Doppler shift to investigate the driving error factors of a combined navigation system. This work allows constellation designers to quickly and easily determine the impact of adding noisy pseudorange measurements to a carrier-Doppler-shift-based navigation system. Solutions to challenges created by using pseudorange and carrier Doppler shift measurements in a DOP analysis are provided in the third manuscript. One of the solutions involves developing an alternative DOP metric, $\delta GDOP$ – a metric of the combined position, velocity, and clock offset rate accuracy, and using it in conjunction with $TDOP$ – the clock offset accuracy – to develop good approximations of the solution components' RMS estimation errors. Finally, the third manuscript provides an example of how to use the DOP metrics for constellation design.

Results from the DOP analysis agree with results from previous work and the analysis from the first manuscript. The agreement indicates that the DOP analysis is correct, but also confirms that the driving error factors in the first manuscript are correct. The geometric

diversity of the line-of-sight unit direction vectors between the satellites and the receiver is shown to be a driving error factor in both the first manuscript's analysis and the DOP analysis, even with the addition of noisy pseudorange measurements. Also important to both analyses is diversity of the rates of change of these unit direction vectors. As a part of the DOP analysis, the values of the elements in the A_{DOP} coefficient matrix in a linearized measurement model are used to form an idea of how much diversity of the line-of-sight vectors between the satellites and the receivers and between their rates of change exists. Even though this analysis applies only to point-solution batch filters when many satellites are simultaneously available, the contributions of Ch. 3 demonstrate that, in the case of carrier Doppler shift measurements only, good GDOP for the batch filter – as in [42] – goes hand-in-hand with good performance of a tightly-coupled INS/radio-navigation Kalman filter if such a filter is needed due to reduced satellite availability at any given location.

This dissertation makes several contributions to the development of a navigation system independent of GNSS that uses carrier Doppler shift from the broadcast signals of LEO communication constellations. The dissertation first demonstrates the feasibility of using LEO communication satellites to navigate with GNSS-like accuracy. Then a number of methods to improve navigation accuracy are shown. It then discusses the different methods that can be used to implement a KF to determine a receiver's position and velocity from INS and carrier Doppler shift measurements. An analysis is conducted of the different implementation methods to determine if any architecture reduces navigation error. Finally, it provides a simple DOP analysis that produces rough estimates of a receiver's position, clock, velocity, and clock rate accuracy using noisy pseudorange measurements in addition to carrier Doppler shift measurements without the need for a complex Kalman filter if enough carrier Doppler shift measurements and pseudorange measurements are available for a batch filter point solution.

Bibliography

[1] FCC Report. *ONEWEB NON-GEOSTATIONARY SATELLITE SYSTEM (LEO) – Attachment A*. FCC Space Station Applications. Jan. 2018. URL: https://fcc.report/IBFS/SAT-MPL-20200526-00062/2379565.pdf (visited on 11/21/2022).

[2] A. Lehtinen. "Doppler Positioing with GPS". MA thesis. Tampere Univeristy of Technology Department of Electrical Engineering, 2001. URL: https://www.yumpu.com/en/document/read/18205420/antti-lehtinen-doppler-positioning-with-gps-matematiikan-laitos (visited on 11/21/2022).

[3] A. Rawnsley. "Iran's Alleged Drone Hack: Tough, but Possible". In: *Wired* (Dec. 2011). URL: https://www.wired.com/2011/12/iran-drone-hack-gps/ (visited on 11/21/2022).

[4] J. Amos. "UK Government Takes £400m Stake in Satellite Firm OneWeb". In: *BBC News* (July 2020). URL: http://bbc.in/2KwVUQM (visited on 11/21/2022).

[5] B. M. Aumayer and M. G. Petovello. "Effect of Sampling Rate Error on GNSS Velocity and Clock Drift Estimation". In: *Navigation: Journal of The Institute of Navigation* 62.3 (2015), pp. 229–238. DOI: https://doi.org/10.1002/navi.114.

[6] Y. Bar-Shalom, X. Li, and T. Kirubarajan. *Estimation with Applications to Tracking and Navigation: Theory, Algorithms and Software*. Wiley-Interscience; 1st edition, 2001, pp. 371–420. DOI: https://doi.org/10.1002/0471221279.ch10.

[7] B. Barshan and H. Durrant-Whyte. "Inertial Navigation Systems for Mobile Robots". In: *Robotics and Automation, IEEE Transactions on* 11.3 (July 1995), pp. 328–342. DOI: https://doi.org/10.1109/70.388775.

[8] H. Benzerrouk et al. "Alternative PNT based on Iridium Next LEO Satellites Doppler/INS Integrated Navigation System". In: *2019 26th Saint Petersburg International Conference on Integrated Navigation Systems (ICINS)*. 2019, pp. 1–10. DOI: https://doi.org/10.23919/ICINS.2019.8769440.

[9] G. J. Bierman. "Factorization Methods for Discrete Sequential Estimation". In: New York, NY: Academic, 1977. Chap. 5, pp. 68–81. URL: https://books.google.com/books?id=5AZjEmUKXGcC (visited on 11/21/2022).

[10] R. G. Brown and P. Y. Hwang. *Introduction to Random Signals and Applied Kalman Filtering*. 3rd Edition. New York: Wiley, Nov. 1977, pp. 428–432. ISBN: 0470609699. URL: https://tinyurl.com/492sarvd (visited on 11/21/2022).

[11] *FCC Fines Operator of GPS Jammer That Affected Newark Airport GBAS*. July 2013. URL: https://insidegnss.com/fcc-fines-operator-of-gps-jammer-that-affected-newark-airport-gbas/ (visited on 11/21/2022).

[12] FCC Report. *Application of Kuiper Systems LLC for Authority to Launch and Operate a Non-Geostationary Satellite Orbit System in Ka-band Frequencies – Technical Appendix*. FCC Space Station Applications. Mar. 2019. URL: https://fcc.report/IBFS/SAT-LOA-20190704-00057/1773885 (visited on 11/21/2022).

[13] FCC Report. *SPACEX NON-GEOSTATIONARY SATELLITE SYSTEM – Attachment A*. FCC Space Station Applications. Mar. 2017. URL: https://fcc.report/IBFS/SAT-MOD-20181108-00083/1569860.pdf (visited on 11/21/2022).

[14] C. E. Fossa et al. "An overview of the IRIDIUM (R) low Earth orbit(LEO) satellite system". In: *Proceedings of the IEEE 1998 National Aerospace and Electronics Conference*. Dayton, Ohio: NAECON, 1998, pp. 152–159. DOI: https://doi.org/10.1109/NAECON.1998.710110.

[15] M. George and S. Sukkarieh. "Tightly Coupled INS/GPS with Bias Estimation for UAV Applications". In: *Proceedings of the Australiasian Conference on Robotics and Automation (ACRA)*. Sydney, Australia, 2005, pp. 1–8. URL: https://www.researchgate.net/publication/228996997_Tightly_coupled_INSGPS_with_bias_estimation_for_UAV_applications (visited on 11/21/2022).

[16] P. E. Gill, W. Murray, and M. H. Wright. *Practical optimization*. Philadelphia, PA: Society for Industrial and Applied Mathematics, 1981, pp. 133–140. DOI: https://doi.org/10.1137/1.9781611975604.

[17] M. Givens. "Multiple IMU Sensor Fusion for sUAS Navigation and Photogrammetry". Copyright - Database copyright ProQuest LLC; ProQuest does not claim copyright in the individual underlying works; Last updated - 2021-05-26. PhD thesis. Utah State University, 2019, pp. 20–25. URL: https://www.proquest.com/dissertations-theses/multiple-imu-sensor-fusion-suas-navigation/docview/2316006248/se-2?accountid=14826 (visited on 11/21/2022).

[18] R. L. Greenspan. "Inertial Navigation Technology from 1970–1995". In: *NAVIGATION* 42.1 (1995), pp. 165–185. DOI: https://doi.org/10.1002/j.2161-4296.1995.tb02334.x. eprint: https://onlinelibrary.wiley.com/doi/pdf/10.1002/j.2161-4296.1995.tb02334.x. URL: https://onlinelibrary.wiley.com/doi/abs/10.1002/j.2161-4296.1995.tb02334.x.

[19] HoneyWell Aerospace. *HG4930 MEMS Inertial Measurement Unit*. HoneyWell Aerospace, 2019. URL: https://aerospace.honeywell.com/us/en/products-and-services/product/hardware-and-systems/sensors/hg4930-mems-inertial-measurement-unit (visited on 11/21/2022).

[20] P. Iannucci and T. Humphreys. "Economical Fused LEO GNSS". In: *Proceedings of 2020 IEEE/ION Position, Location and Navigation Symposium (PLANS)*. Apr. 2020, pp. 426–443. DOI: https://doi.org/10.1109/PLANS46316.2020.9110140.

[21] S. Jain, A. Humne, and K. Chandrasekaran. *Evaluation of Attitude and Heading Reference System*. Nov. 2014. URL: https://www.researchgate.net/publication/281290727_Evaluation_of_Attitude_and_Heading_Reference_System (visited on 11/21/2022).

[22] M. Joerger et al. "Analysis of Iridium-Augmented GPS for Floating Carrier Phase Positioning". In: *NAVIGATION* 57.2 (2010), pp. 137–160. DOI: https://doi.org/10.1002/j.2161-4296.2010.tb01773.x. eprint: https://onlinelibrary.wiley.com/doi/pdf/10.1002/j.2161-4296.2010.tb01773.x. URL: https://onlinelibrary.wiley.com/doi/abs/10.1002/j.2161-4296.2010.tb01773.x.

[23] R. E. Kalman. "A New Approach to Linear Filtering and Prediction Problems". In: *Journal of Basic Engineering* 82.1 (Mar. 1960), pp. 35–45. ISSN: 0021-9223. DOI: https://doi.org/10.1115/1.3662552. eprint: https://asmedigitalcollection.asme.org/fluidsengineering/article-pdf/82/1/35/5518977/35_1.pdf.

[24] S.E. Langel et al. "Tightly Coupled GPS/INS Integration for Differential Carrier Phase Navigation Systems Using Decentralized Estimation". In: *IEEE/ION Position, Location and Navigation Symposium*. Indian Wells, CA, 2010, pp. 397–409. DOI: https://doi.org/10.1109/PLANS.2010.5507177.

[25] E. J. Lefferts, F. L. Markley, and M. D. Shuster. "Kalman Filtering for Spacecraft Attitude Estimation". In: *Journal of Guidance, Control, and Dynamics* 5.5 (1982), pp. 417–429. DOI: https://doi.org/10.2514/6.1982-70.

[26] F. Lemoine et al. "The development of the joint NASA GSFC and the National Imagery and Mapping Agency (NIMA) geopotential model EGM96". In: *NASA Goddard Space Flight Center, Greenbelt, Maryland, 20771 USA* (July 1998). URL: https://science.gsfc.nasa.gov/sed/content/uploadFiles/publication_files/EGM96_NASA-TP-1998-206861.pdf (visited on 11/21/2022).

[27] J. B. Lundberg and B. E. Schutz. "Recursion formulas of Legendre functions for use with nonsingular geopotential models". In: *Journal of Guidance, Control, and Dynamics* 11.1 (1988), pp. 31–38. DOI: https://doi.org/10.2514/3.20266.

[28] M. Jones. "Spoofing in the Black Sea: What really happened?" In: *GPS World* (Oct. 2017). URL: https://www.gpsworld.com/spoofing-in-the-black-sea-what-really-happened/ (visited on 11/21/2022).

[29] F. L. Markley and J. L. Crassidis. "Filtering for Attitude Estimation and Calibration". In: *Fundamentals of Spacecraft Attitude Determination and Control*. New York, NY: Springer New York, 2014, pp. 235–285. ISBN: 978-1-4939-0802-8. DOI: https://doi.org/10.1007/978-1-4939-0802-8_6.

[30] B. McLemore and M. L. Psiaki. "GDOP of Navigation using Pseudorange and Doppler Shift from a LEO Constellation". In: *Proceedings of the 34th International Technical Meeting of the Satellite Division of The Institute of Navigation (ION GNSS+ 2021)*. Sept. 2021, pp. 2783–2803. DOI: https://doi.org/10.33012/2021.18008.

[31] B. McLemore and M. L. Psiaki. "Navigation Using Doppler Shift from LEO Constellations and INS Data". In: *Proceedings of the ION GNSS+ 2020*. Virtual. Sept. 2020, pp. 3071–3086. DOI: https://doi.org/10.33012/2020.17670.

[32] B. McLemore and M. L. Psiaki. "Navigation Using Doppler Shift from LEO Constellations and INS Data". In: *IEEE Transactions on Aerospace and Electronic Systems* 58.5 (Oct. 2022), pp. 4295–4314. DOI: https://doi.org/10.1109/TAES.2022.3162772.

[33] V. B. Mendes. *Modeling the Neutral-Atmosphere Propagation Delay in Radiometric Space Techniques*. Ph.D. Dissertation, Dept. of Geodesy and Geomatics Engineering, Engineering Technical Report No. 199, Univ. of New Brunswick, Fredericton, New Brunswick, Canada, Apr. 1999. URL: https://gge.ext.unb.ca/Pubs/TR199.pdf (visited on 11/21/2022).

[34] M. Meza. *Manual For ICAO AERONAUTICAL MOBILE SATELLITE (ROUTE) SERVICE Part 2-IRIDIUM*. Mar. 2007. URL: https://bit.ly/37oX3D1 (visited on 11/21/2022).

[35] P. Miller et al. "Autonomous Underwater Vehicle Navigation". In: *Journal of Oceanic Engineering, IEEE* 35.3 (Aug. 2010), pp. 663–678. DOI: https://doi.org/10.1109/JOE.2010.2052691.

[36] P. Misra and P. Enge. *Global Positioning System: Signals, Measurements, and Performance*. Ganga-Jamuna Press, 2011, pp. 199–224. ISBN: 9780970954428. URL: https://books.google.com/books?id=5WJOywAACAAJ (visited on 11/21/2022).

[37] J. Morales, J. Khalife, and Z. Kassas. "Simultaneous Tracking of Orbcomm LEO Satellites and Inertial Navigation System Aiding Using Doppler Measurements". In: *2019 IEEE 89th Vehicular Technology Conference (VTC2019-Spring)*. 2019, pp. 1–6. DOI: https://doi.org/10.1109/VTCSpring.2019.8746485.

[38] J. Morales et al. "Inertial Navigation System Aiding with Orbcomm LEO Satellite Doppler Measurements". In: *Proceedings of the 31st International Technical Meeting of the Satellite Division of The Institute of Navigation (ION GNSS+ 2018)*. Miami, Florida, 2018, pp. 2718–2725. DOI: https://doi.org/10.33012/2018.16059.

[39] R. Morales-Ferre et al. "GDOP-based analysis of suitability of LEO constellations for future satellite-based positioning". In: *Proceedings of 2020 IEEE International Conference on Wireless for Space and Extreme Environments*. 2020, pp. 147–152. DOI: https://doi.org/10.1109/WiSEE44079.2020.9262624.

[40] R. Munguía. "A GPS-aided Inertial Navigation System in Direct Configuration". In: *Journal of Applied Research and Technology* 12.4 (Aug. 2014), pp. 803–814. DOI: https://doi.org/10.1016/S1665-6423(14)70096-3.

[41] United States Executive Office of the President (Donald Trump). *Executive order 13905: Strengthening National Resilience Through Responsible Use of Positioning, Navigation, and Timing Services*. 2020. URL: http://bit.ly/3oErJXk (visited on 11/21/2022).

[42] M. L. Psiaki. "Navigation using Carrier Doppler Shift from a LEO Constelllation: TRANSIT on Steroids". In: *NAVIGATION* 68.3 (2021), pp. 621–641. DOI: https://doi.org/10.1002/navi.438. eprint: https://onlinelibrary.wiley.com/doi/pdf/10.1002/navi.438. URL: https://onlinelibrary.wiley.com/doi/abs/10.1002/navi.438 (visited on 11/21/2022).

[43] M. L. Psiaki, T. E. Humphreys, and B. Stauffer. "Attackers can spoof navigation signals without our knowledge. Here's how to fight back GPS lies". In: *IEEE Spectrum* 53.8 (2016), pp. 26–53. DOI: https://doi.org/10.1109/MSPEC.2016.7524168.

[44] M. L. Psiaki and B. McLemore. "TRANSIT on Steroids: Doppler-Based GNSS Meets Large LEO Constellations". In: *Inside GNSS* 15.6 (Dec. 2020), pp. 48–53. URL: https://insidegnss.com/transit-on-steroids-doppler-based-gnss-meets-large-leo-constellations/ (visited on 11/21/2022).

[45] P. Racelis, P. Pervan, and M. Joerger. "Fault-Free Integrity Analysis of Mega-Constellation-Augmented GNSS". In: *Proceedings of the 32nd International Technical Meeting of the Satellite Division of The Institute of Navigation (ION GNSS+ 2019)*. Miami, Florida, Sept. 2019, pp. 465–484. DOI: https://doi.org/10.33012/2019.16862.

[46] T. Reid et al. "Broadband LEO Constellations for Navigation". In: *NAVIGATION* 65.2 (2018), pp. 205–220. DOI: https://doi.org/10.1002/navi.234.

[47] Z. Tan et al. "Positioning Using IRIDIUM Satellite Signals of Opportunity in Weak Signal Environment". In: *Electronics* 9.1 (Dec. 2019), pp. 37–55. DOI: https://doi.org/10.3390/electronics9010037.

[48] S. Vajda and A. Zorn. "Survey of existing and emerging technologies for strategic submarine navigation". In: *IEEE 1998 Position Location and Navigation Symposium (Cat. No.98CH36153)*. 1998, pp. 309–315. DOI: https://doi.org/10.1109/PLANS.1998.670102.

[49] J. Wendel, C Schlaile, and G. Trommer. "Direct Kalman Filtering of GPS/INS for Aerospace Applications". In: *Proceedings of the International Symposium on Kinematic Systems in Geodesy, Geomatics and Navigation : June 5 - 8, 2001, Banff, Alberta, Canada*. International Symposium on Kinematic Systems in Geodesy, Geomatics and Navigation. 2001 (Banff, Kanada, June 5–8, 2001). Univ., 2001, pp. 144–149. URL: https://tinyurl.com/mppr4v4n (visited on 11/21/2022).

[50] J. R. Wertz. "Attitude Dynamics". In: *Spacecraft Attitude Determination and Control*. Dordrecht: Springer Netherlands, 1978, pp. 510–557. ISBN: 978-94-009-9907-7. DOI: https://doi.org/10.1007/978-94-009-9907-7_16.

[51] M. Zhu, F. Yu, and X. Wenjiao. "An Unconventional Multiple Low-Cost IMU and GPS-Integrated Kinematic Positioning and Navigation Method Based on Singer Model". In: *Sensors* 19.19 (Oct. 2019), pp. 4274–4297. DOI: https://doi.org/10.3390/s19194274.